APPENDICES: PREPARATION AND CHARACTERISATION OF POLY(ETHYLENE TEREPHTHALATE) NANOCOMPOSITES

LIST OF CONTENTS 2-17

List of Contents

APPENDIX 7: THERMAL DEGRADATION KINETICS

APPENDIX 8: THERMO-OXIDATIVE DEGRADATION (TGA/DSC)

APPENDIX 9: THERMO-OXIDATIVE DEGRADATION KINETICS

Calculation 1: Estimation of the molar mass for a montmorillonite platelet with dimensions 100 nm x 100 nm

Molecular formula: $[M_x[Al_{4-x}Mg_x](Si_8)O_{20}(OH)_4]$

The platelet will be considered with no isomorphous substitution, and therefore no counter ions should be present within the molecular formula.

Revised molecular formula: $[Al_4(Si_8)O_{20}(OH)_4]$

Repeat distance for a silica unit: ~ 2.25 Å (0.225 nm)

If platelet is 100 nm in length/breadth then approximately 444.44 silica units will be present.

Mass of a basic layer unit consisting of 2 Si and 1 Al: 180.16 g

Mass of a single layer 1 silica unit thick: 80,069.51 g

Molar mass for platelet 100 x 100 nm: 6,411,126,609.57 g mol^{-1}

Calculation 2: Estimation of interplatelet distance on exfoliation for a variety of tactoids sizes, and the resulting platelet mass and percentage weight of clay within a 1 cm^3 PET model. The model was created under the guidance of Duncan MacKerron at DuPont Teijin Films Ltd, Wilton.

The exfoliation of model tactoids of various platelet contents have been considered, within a 1 cm^3 PET matrix. For simplicity, platelet contents were multiples of 8 due to the cubic special area considered.

Intertactoid distances were considered from the centre of the tactoids, with the starting distance 1 x 10^8 nm. Only final interplatelet distances were reported for simplicity. Calculations are purely theoretical, as a starting tactoid of 2.815 x 10^{14} could obviously not exist in reality.

The total platelet mass was calculated as follows: mass = no. platelets x (platelet molar mass/ avagadro's number). The total mass was then used to determine the percentage weight within 1 cm^3 of PET.

The mass of 1cm^3 of PET was calculated through the following equation: mass = density x volume. The density of PET is 1.335 g cm^{-3}, therefore the calculated mass of a 1 cm^3 volume is 1.335g.

Table 1 Data relating the number of starting platelets in a tactoids to the interplatelet distance on complete exfoliation, in addition to the total platelet mass and resulting % weight within 1 cm^3 of PET

No. platelets in starting tactoid	Interplatelet distance at complete exfoliation (nm)	Total platelet mass (g)	% weight within 1 cm^3 of PET
8	5 x 10^6	1.329 x 10^{-23}	9.954 x 10^{-22}
64	2.5 x 10^6	1.063 x 10^{-22}	7.963 x 10^{-21}
512	1.25 x 10^6	8.505 x 10^{-22}	6.371 x 10^{-20}
4,096	6.25 x 10^5	6.804 x 10^{-21}	5.097 x 10^{-19}
32,768	3.125 x 10^5	5.443 x 10^{-20}	4.077 x 10^{-18}
262,144	1.563 x 10^5	4.355 x 10^{-19}	3.262 x 10^{-17}
2,097,152	7.813 x 10^4	3.484 x 10^{-18}	2.609 x 10^{-16}
16,777,216	3.906 x 10^4	2.787 x 10^{-17}	2.088 x 10^{-15}
134,217,728	1.953 x 10^4	2.230 x 10^{-16}	1.670 x 10^{-14}
1,073,741,824	9.766 x 10^3	1.784 x 10^{-15}	1.336 x 10^{-13}
8,589,934,592	4.883 x 10^3	1.427 x 10^{-14}	1.069 x 10^{-12}
6.872 x 10^{10}	2.441 x 10^3	1.142 x 10^{-13}	8.551 x 10^{-12}
5.498 x 10^{11}	1,221	9.132 x 10^{-13}	6.841 x 10^{-11}
4.398 x 10^{12}	610	7.306 x 10^{-12}	5.472 x 10^{-10}
3.518 x 10^{13}	305	5.845 x 10^{-11}	4.378 x 10^{-9}
2.815 x 10^{14}	152	4.676 x 10^{-10}	3.502 x 10^{-8}

Table 1 provides an approximate interplatelet distance if complete and homogeneous exfoliation is presumed. It is observed that complete exfoliation may theoretically only be present at extremely low weight percentages of montmorillonite to a maximum of 3.502×10^{-8} % w/w. This loading is significantly lower than any of the loadings studied within this thesis. It is unrealistic to therefore assume the formation of a house of cards structure as a significant degree of platelet exfoliation is unlikely, with a partial structure of book-house structure appearing more realistic.

Calculation 3: Estimation of surface modifier content on platelet surface

Percentage mass loss of Cloisites® 6A, 15A and 20A was determined though thermogravimetric analysis. The mass loss was then correlated to the reported modifier concentration in meq/100g reported by Southern Clay Products, Inc. A linear relationship was observed following the relationship: $y = 0.1703x + 5.2701$.

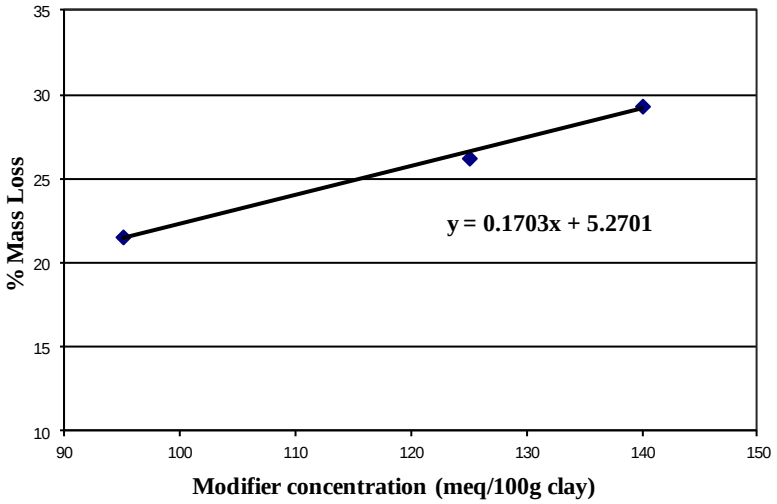

Figure 1 % Mass loss versus organic modifier concentration of Cloisites® 20A, 15A and 6A.

The molar mass of the ammonium dimethyl dehydrogenated tallow modifier was calculated as 527.974 g mol^{-1}. The molar mass was then be used to calculate the number of moles of modifier present, using the determined mass loss within the clay due to degradation of the organic modifiers; a loss of 29.33 %, 26.24 % and 21.56 % for Cloisites® 6A, 15A and 20A, respectively.

The moles of modifier present within the clay were calculated using a theoretical mass loss within 100g of clay. For example, within 100g of Cloisite® 20A, 21.56% of the clay lost during TGA will be attributed to the degradation of the organic modifiers. The estimated number of moles of modifier present can then be used to calculate an estimate number of modifier molecules.

Table 2 Data relating to modifier content on Cloisites® 20A, 15A and 6A

Cloisite®	Modifier concentration (meq/100g clay)	Modifier molar mass (g mol^{-1})	% mass loss	Moles of modifier	No. of modifier molecules
20A	95	527.97	21.56	0.0408	2.457×10^{22}
15A	125		26.24	0.0497	2.993×10^{22}
6A	140		29.33	0.0556	3.348×10^{22}

In Calculation 2, the molar mass of a model platelet of 100 x 100 nm was calculated as 6,411,126,609.57 g mol^{-1}. The molar mass was employed to calculate an estimate number of platelets in 100g of organically modified nanoclay.

Table 3 Determination of the number of platelets in 100g or organically modified nanoclay

Cloisite®	% Mass MMT	Moles of MMT	No. of platelets
20A	78.44	1.223×10^{-8}	7.36×10^{15}
15A	73.76	1.150×10^{-8}	6.92×10^{15}
6A	70.67	1.102×10^{-8}	6.64×10^{15}

The resulting platelet to modifier ratio is illustrated in table 4.

Table 4 Platelet: modifier ratios

Cloisite®	Platelet : Modifier
20A	1 : 3,338,315
15A	1 : 4,325,145
6A	1 : 5,042,169

The modifier is therefore greatly in excess. If the 100 x 100 nm model platelet is considered a facial surface area of 20,000 nm^2 is available for modification. Nitrogen has an atomic width of 130 pm (0.13 nm) and therefore the majority of modifier present would not be able to electrostatically interact with the platelet surface due to steric hindrance.

APPENDIX 2: DISPERSION EFFECTS

The power output of the sonicator was determined through sonication of a liquid of known specific heat capacity, in this case deionised water. The temperature increase due to sonication was measured against time with a newly calibrated thermocouple, and the change in time and temperature was used to calculate the total power output.

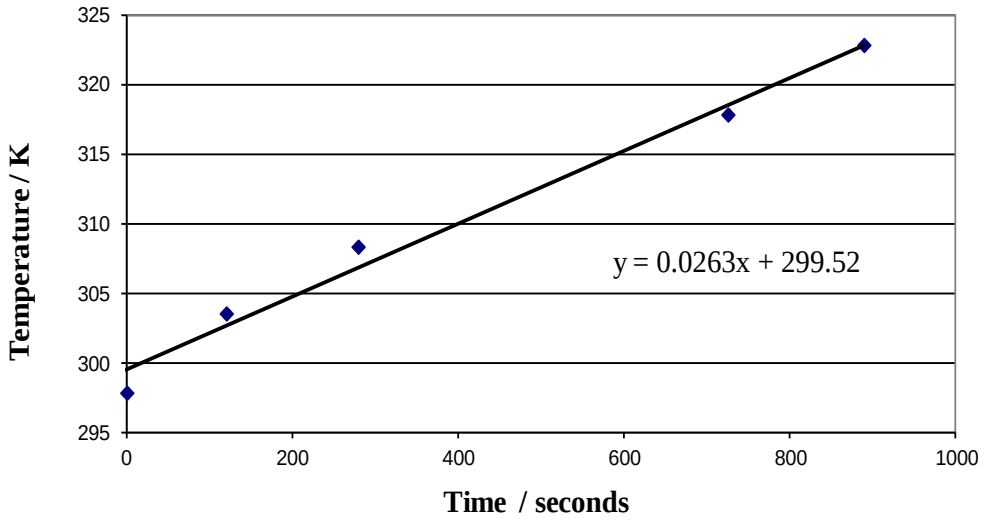

Figure 2 Plot of dT/dt during the sonication of deionised water.

The power output was calculated using equation 1, where C_p was the specific heat capacity (C_p water = 4182 J Kg^{-1} K^{-1}) and M the mass of the liquid (Kg). The power output was calculated at 8.33 J s^{-1}.

$$\text{Power Output} = (dT/dt)\, C_p\, M$$

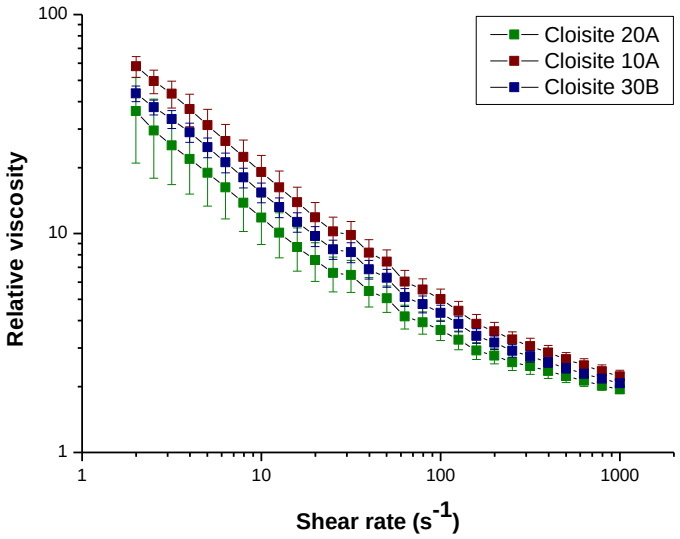

Figure 3 Relative viscosity versus shear rate for ethylene glycol suspensions of Cloisites® 10A, 20A and 30B at a 6% w/w loading.

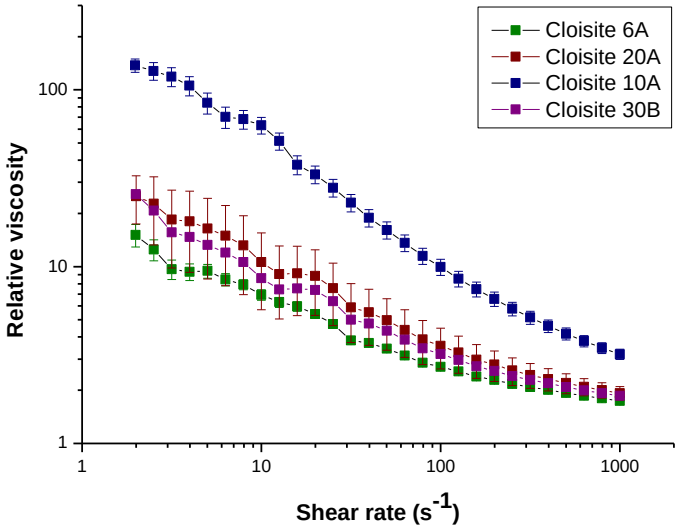

Figure 4 Relative viscosity versus shear rate for diethylene glycol suspensions of Cloisites® 6A, 20A, 10A and 30B at a 6% w/w loading.

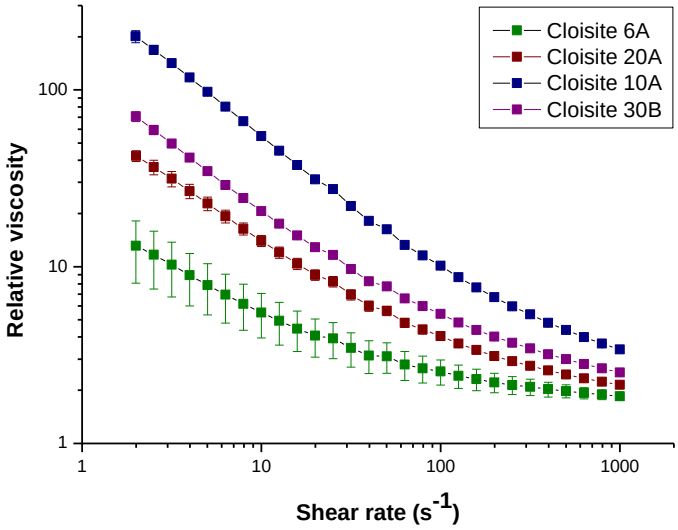

Figure 5 Relative viscosity versus shear rate for triethylene glycol suspensions of Cloisites® 6A, 20A, 10A and 30B at a 6% w/w loading.

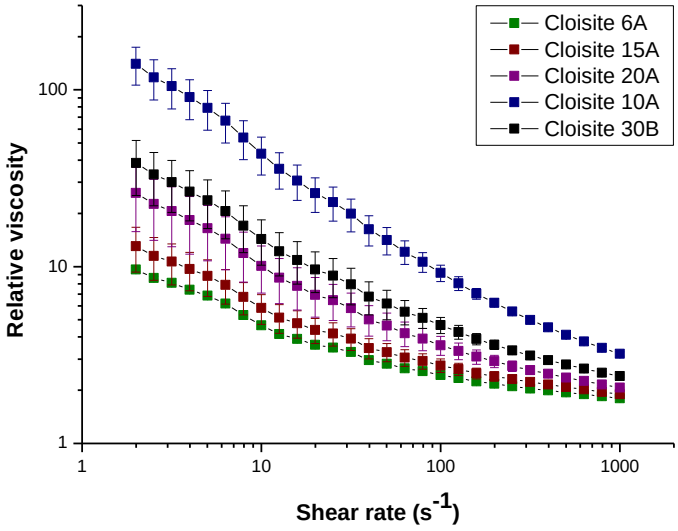

Figure 6 Relative viscosity versus shear rate for tetraethylene glycol suspensions of Cloisites® 6A, 15A, 20A, 10A and 30B at a 6% w/w loading.

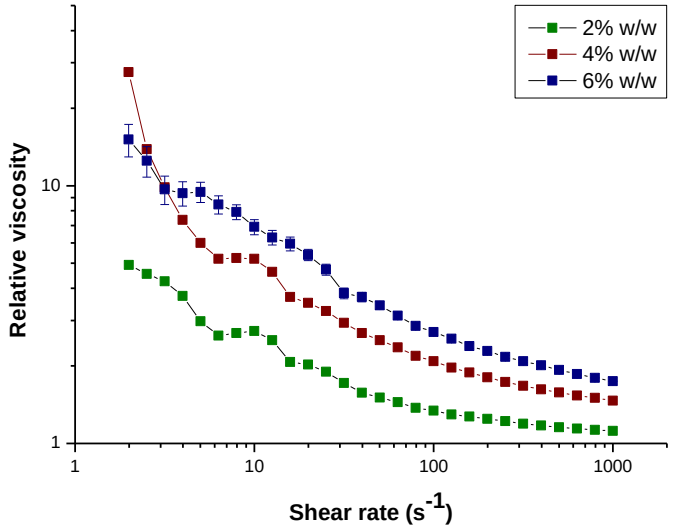

Figure 7 Relative viscosity versus shear rate for diethylene glycol suspensions of Cloisites® 6A at loadings between 2 - 6% w/w.

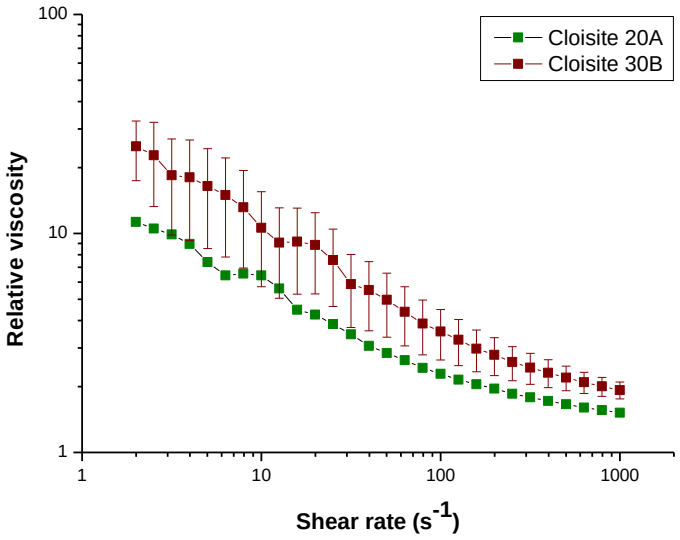

Figure 8 Relative viscosity versus shear rate for diethylene glycol suspensions of Cloisites® 20A at loadings 4 and 6% w/w.

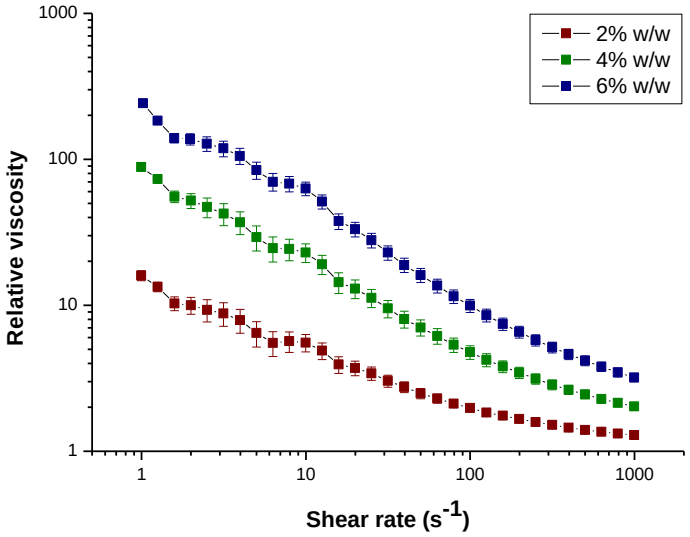

Figure 9 Relative viscosity versus shear rate for diethylene glycol suspensions of Cloisites® 10A at loadings between 2 - 6% w/w.

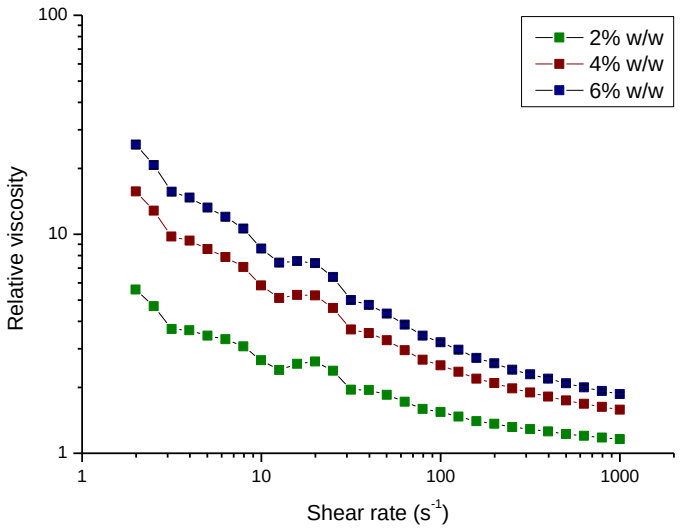

Figure 10 Relative viscosity versus shear rate for diethylene glycol suspensions of Cloisites® 30B at loadings between 2 - 6% w/w.

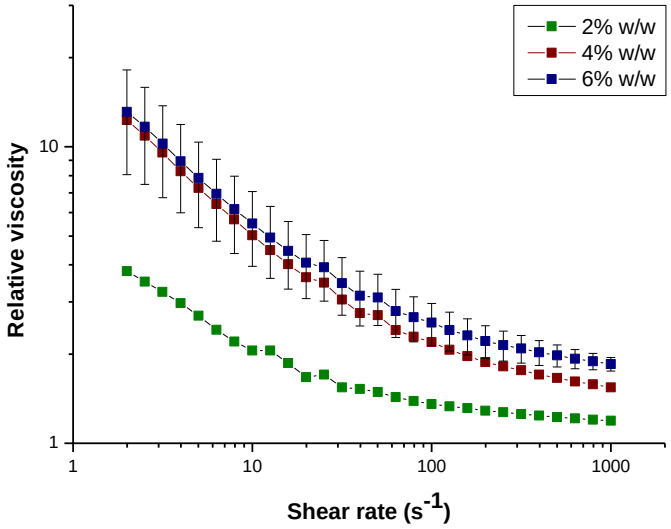

Figure 11 Relative viscosity versus shear rate for triethylene glycol suspensions of Cloisites® 6A at loadings between 2 - 6% w/w.

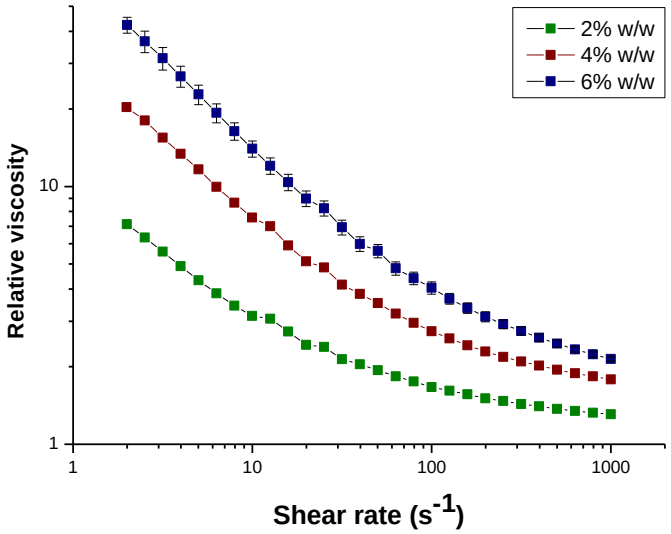

Figure 12 Relative viscosity versus shear rate for triethylene glycol suspensions of Cloisites® 20A at loadings between 2 - 6% w/w.

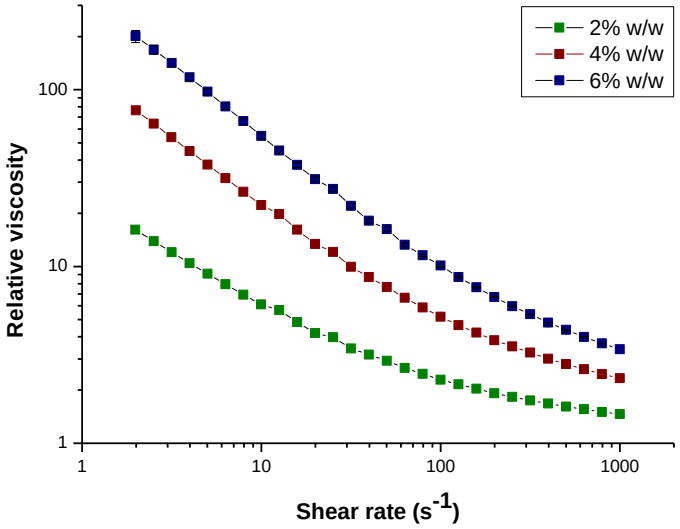

Figure 13 Relative viscosity versus shear rate for triethylene glycol suspensions of Cloisites® 10A at loadings between 2 - 6% w/w.

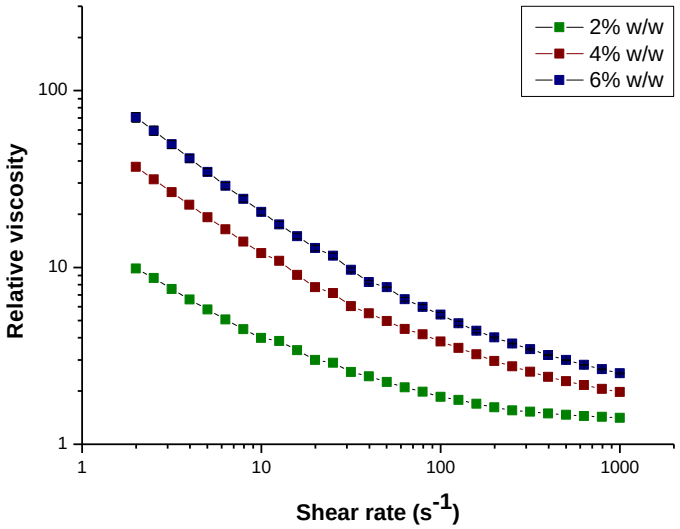

Figure 14 Relative viscosity versus shear rate for triethylene glycol suspensions of Cloisites® 30B at loadings between 2 - 6% w/w.

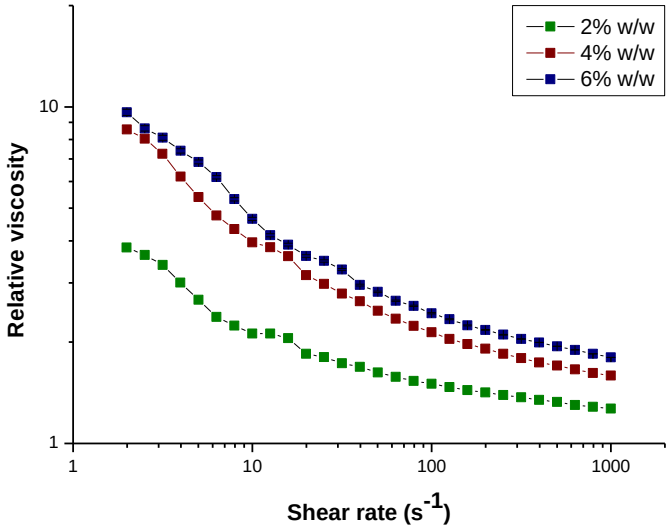

Figure 15 Relative viscosity versus shear rate for tetraethylene glycol suspensions of Cloisites® 6A at loadings between 2 - 6% w/w.

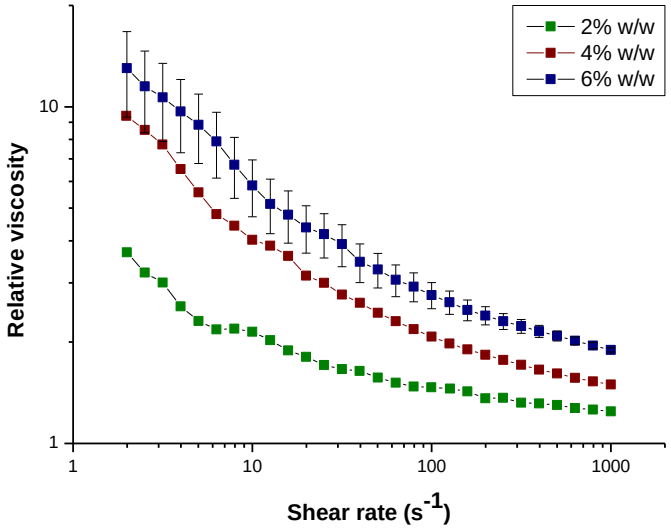

Figure 16 Relative viscosity versus shear rate for tetraethylene glycol suspensions of Cloisites® 15A at loadings between 2 - 6% w/w.

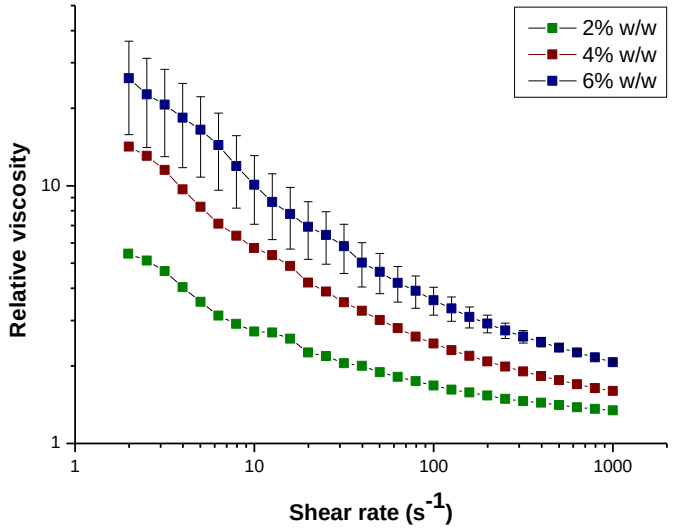

Figure 17 Relative viscosity versus shear rate for tetraethylene glycol suspensions of Cloisites® 20A at loadings between 2 - 6% w/w.

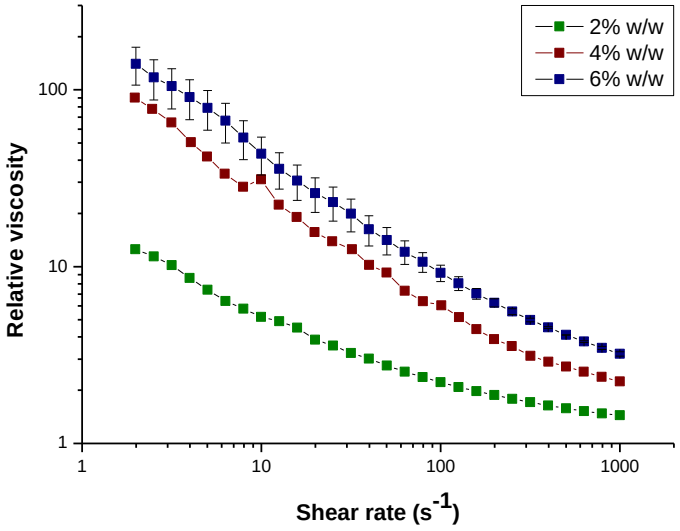

Figure 18 Relative viscosity versus shear rate for tetraethylene glycol suspensions of Cloisites® 10A at loadings between 2 - 6% w/w.

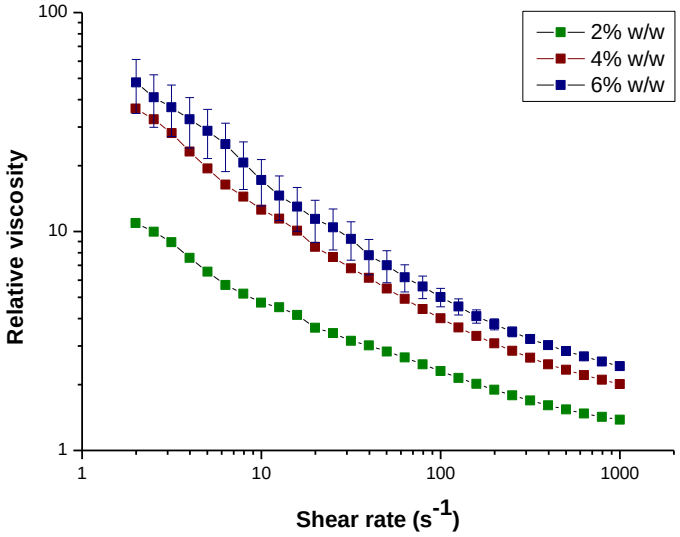

Figure 19 Relative viscosity versus shear rate for tetraethylene glycol suspensions of Cloisites® 30B at loadings between 2 - 6% w/w.

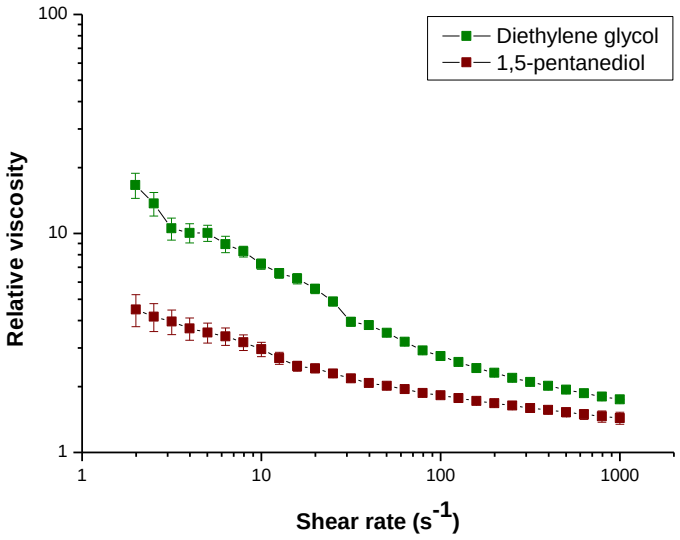

Figure 20 Relative viscosity versus shear rate for diethylene glycol and 1,5-pentanediol suspensions of Cloisites® 6A at a 6% w/w loading.

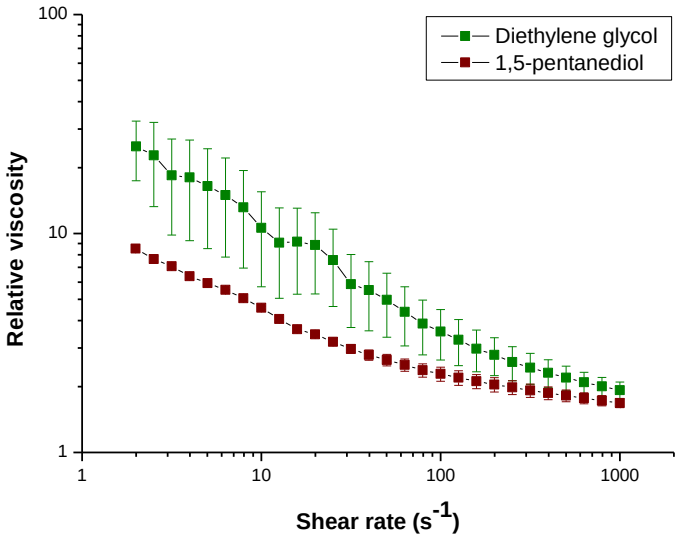

Figure 21 Relative viscosity versus shear rate for diethylene glycol and 1,5-pentanediol suspensions of Cloisites® 20A at a 6% w/w loading.

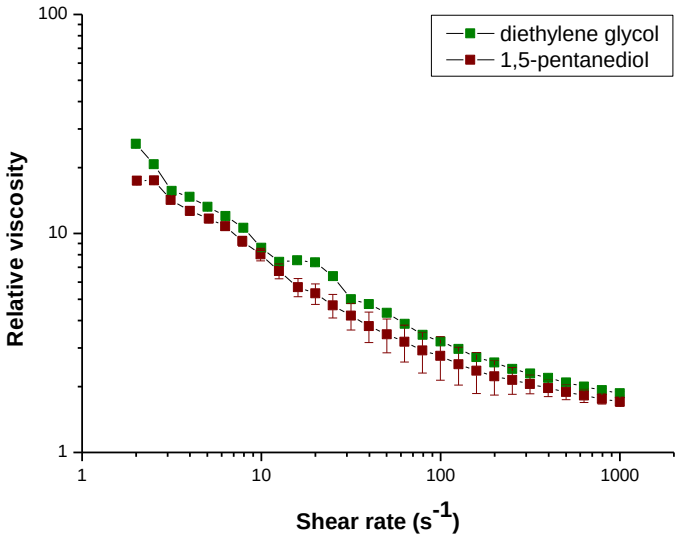

Figure 22 Relative viscosity versus shear rate for diethylene glycol and 1,5-pentanediol suspensions of Cloisites® 30B at a 6% w/w loading.

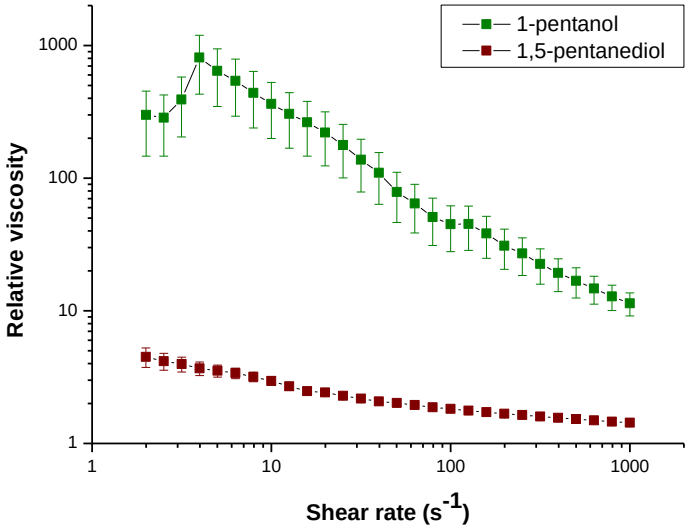

Figure 23 Relative viscosity versus shear rate for 1-pentanol and 1,5-pentanediol suspensions of Cloisites® 6A at a 6% w/w loading.

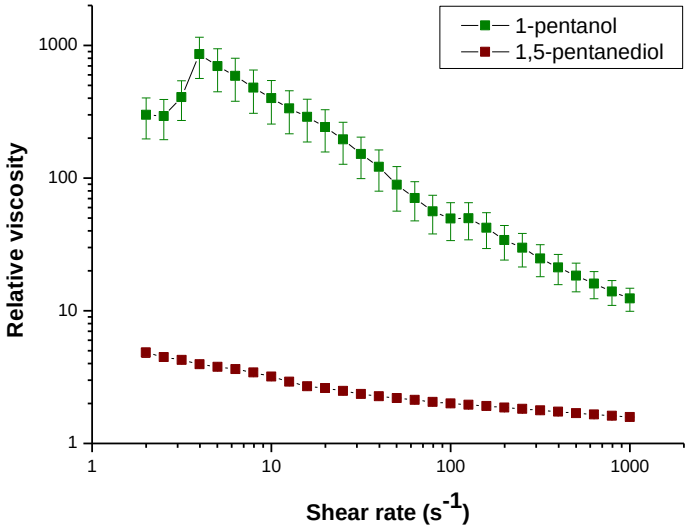

Figure 24 Relative viscosity versus shear rate for 1-pentanol and 1,5-pentanediol suspensions of Cloisites® 15A at a 6% w/w loading.

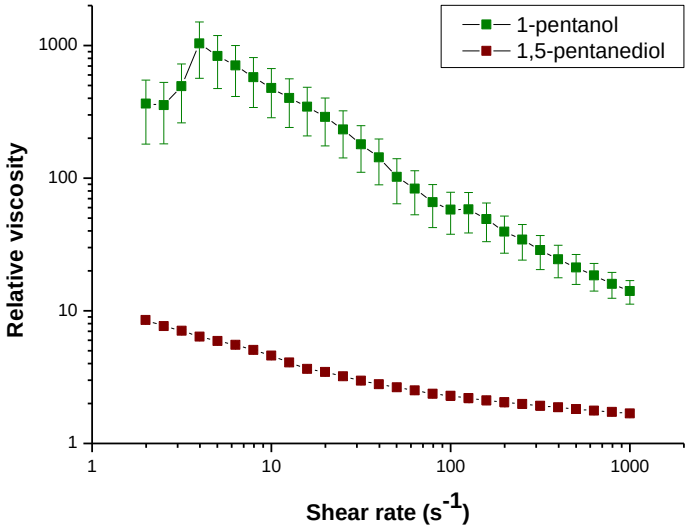

Figure 25 Relative viscosity versus shear rate for 1-pentanol and 1,5-pentanediol suspensions of Cloisites® 20A at a 6% w/w loading.

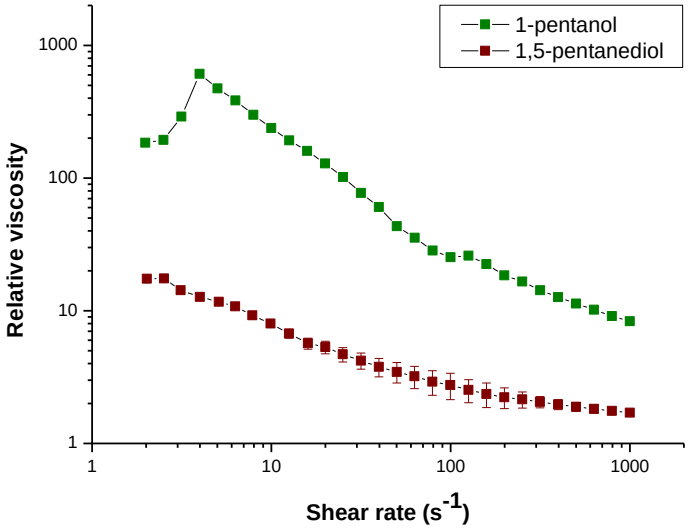

Figure 26 Relative viscosity versus shear rate for 1-pentanol and 1,5-pentanediol suspensions of Cloisites® 30B at a 6% w/w loading.

APPENDIX 3: CHARACTERISATION

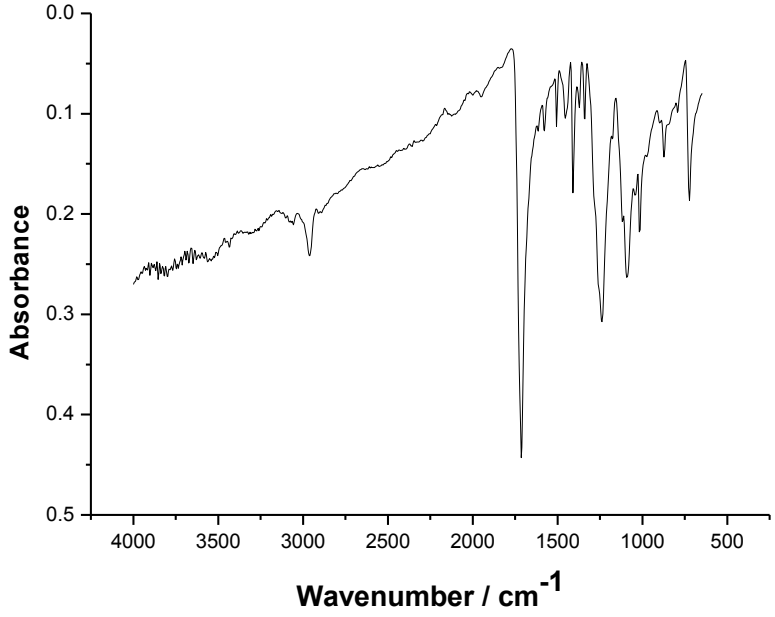

Figure 27 ATR-FTIR spectra of PET0.5G CHIP

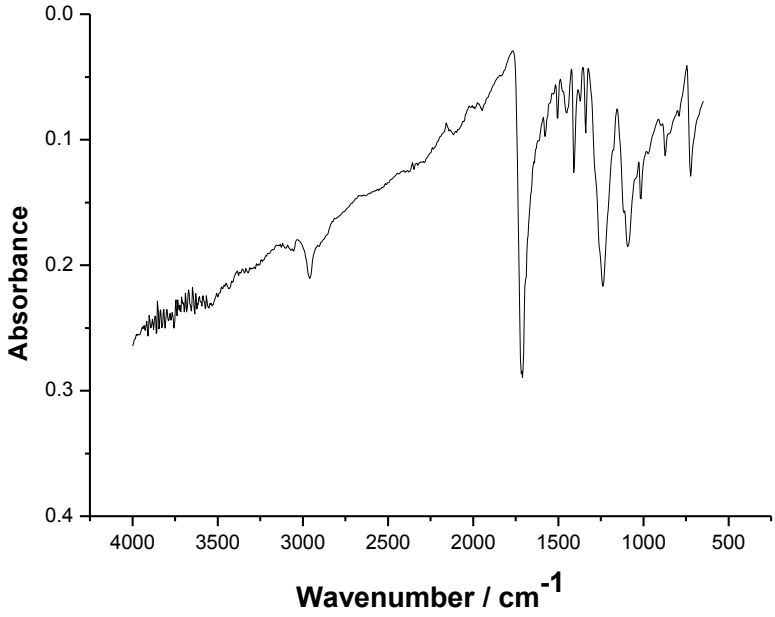

Figure 28 ATR-FTIR spectra of PET1.0G CHIP

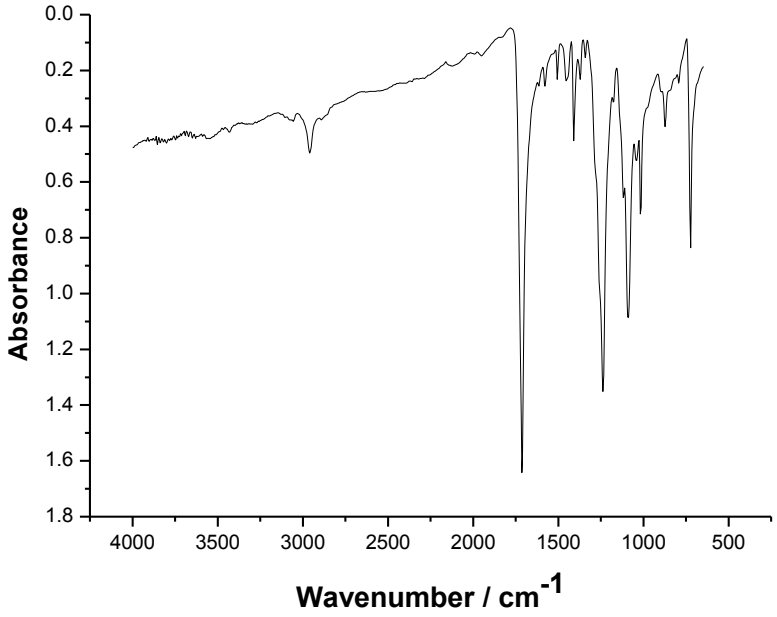

Figure 29 ATR-FTIR spectra of PET UNIAXIAL FILM

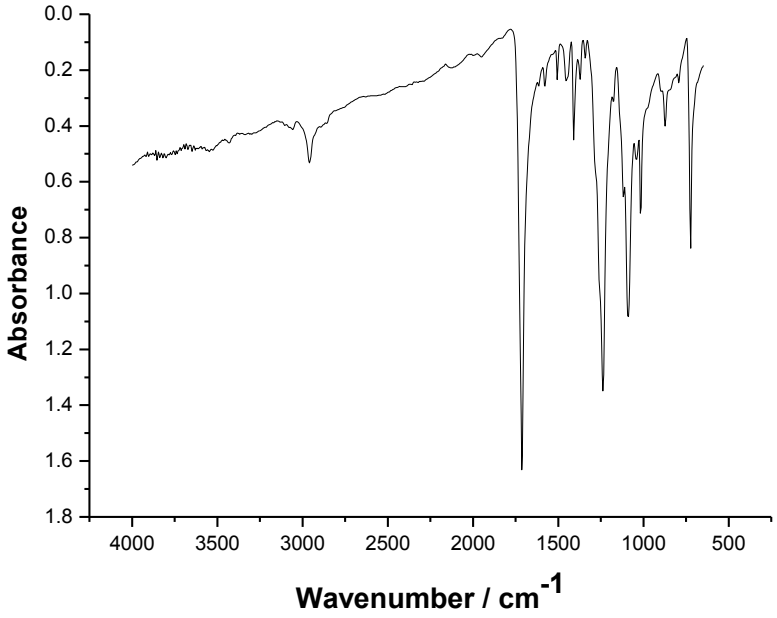

Figure 30 ATR-FTIR spectra of PET0.5G UNIAXIAL FILM

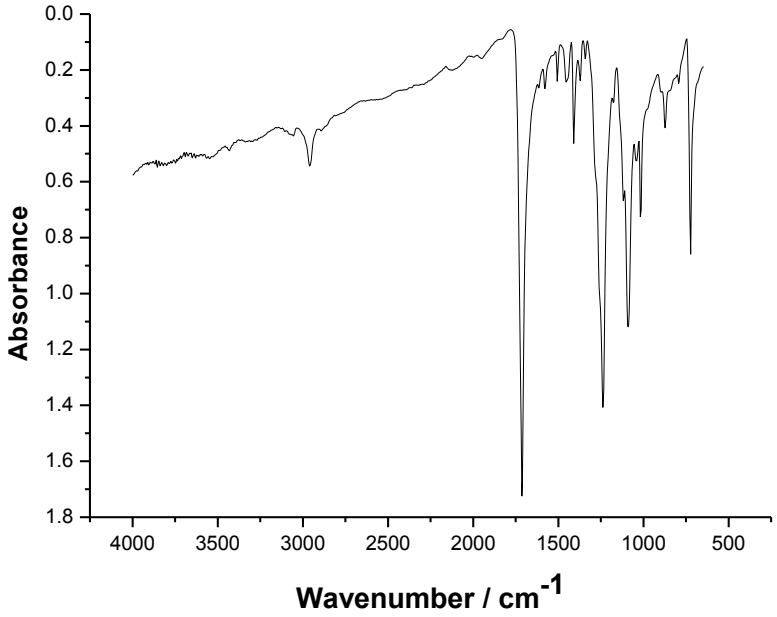

Figure 31 ATR-FTIR spectra of PET1.0G UNIAXIAL FILM

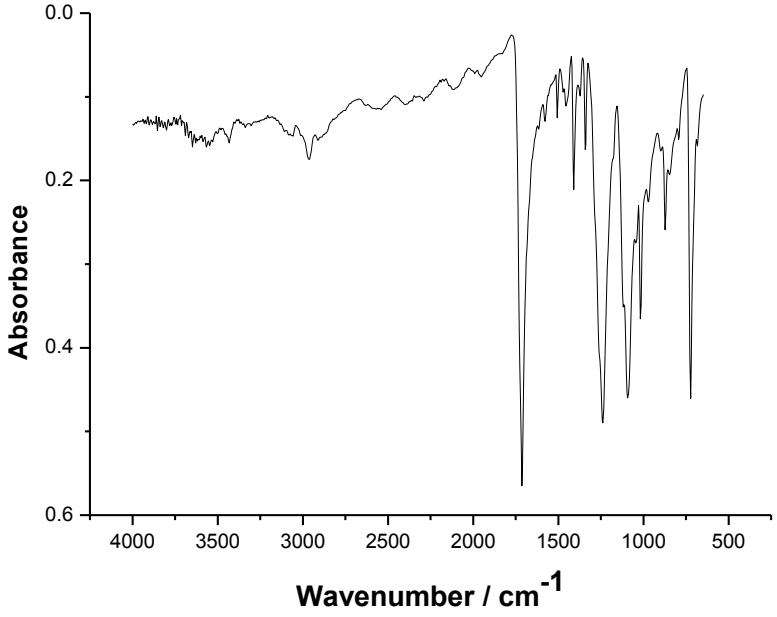

Figure 32 ATR-FTIR spectra of PET BIAXIAL FILM

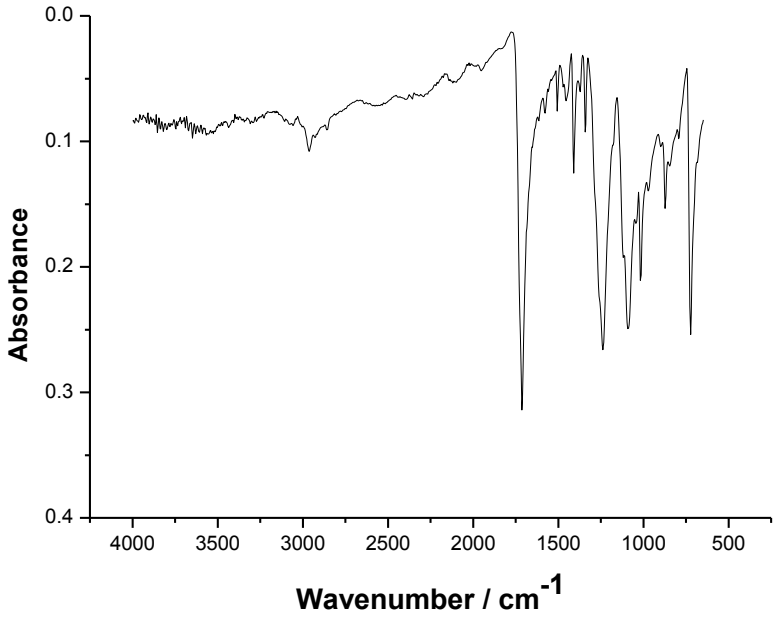

Figure 33 ATR-FTIR spectra of PET0.5G BIAXIAL FILM

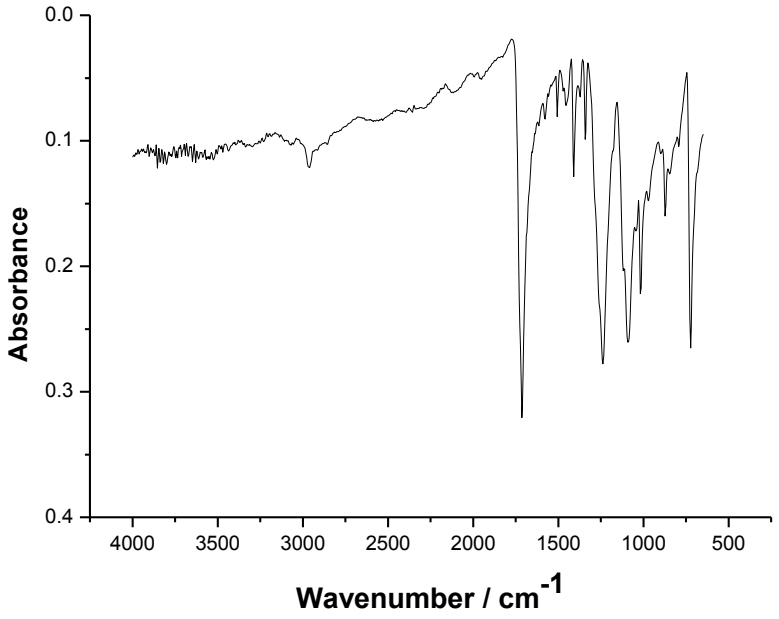

Figure 34 ATR-FTIR spectra of PET1.0G BIAXIAL FILM

Table 5 Intrinsic viscosity standards

PET standard	Sample
1	PET, PET0.5G and PET1.0G amorphous chip and uniaxial film
2	PET, PET0.5G and PET1.0G biaxial film

Table 6 Intrinsic viscosity measurements and calculated molecular weights for the PET standards used prior to determining the molecular weights of PET and PET composite chip and films.

Standard	Replicate	$[\eta]$ / dLg^{-1}	M_w / $g\ mol^{-1}$
1	1	0.619	38,396
	2	0.615	38,030
	Average	0.623 ± 0.003	38,213 ± 259
2	1	0.620	38,488
	2	0.624	38,870
	Average	0.622 ± 0.003	38,679 ± 270

Table 7 Full data sets of intrinsic viscosities and calculated molecular weight for PET and composite chip, illustrating within sample variance. K and α were determined as 4.25×10^{-4} and 0.69 respectively.

Material	Sample	Sample no.	Replicate	$[\eta]$ / dLg^{-1}	M_w / g mol^{-1}
AMORPHOUS CHIP	PET	1	1	0.671	43,162
			2	0.674	43,474
			Average	0.673 ± 0.002	43,318 ± 220
		2	1	0.673	43,384
			2	0.674	43,417
			Average	0.674 ± 0.000	43,400 ± 24
	PET0.5G	1	1	0.656	41,792
			2	0.659	42,049
			Average	0.658 ± 0.002	41,920 ± 182
		2	1	0.659	42,028
			2	0.657	41,865
			Average	0.658 ± 0.001	41,946 ± 115
	PET1.0G	1	1	0.640	40,337
			2	0.642	40,487
			Average	0.641 ± 0.001	40,412 ± 107
		2	1	0.643	40,560
			2	0.638	40,179
			Average	0.641 ± 0.003	40,369 ± 269
UNIAXIAL FILM	PET	1	1	0.611	37,693
			2	0.606	37,266
			Average	0.609 ± 0.003	37,480 ± 302
		2	1	0.616	38,133
			2	0.613	37,908
			Average	0.615 ± 0.002	38,021 ± 159
	PET0.5G	1	1	0.583	35,211
			2	0.581	35,085
			Average	0.582 ± 0.001	35,148 ± 89
		2	1	0.580	34,959
			2	0.578	34,814
			Average	0.579 ± 0.001	34,886 ± 102
	PET1.0G	1	1	0.551	32,480
			2	0.552	32,577
			Average	0.552 ± 0.001	32,529 ± 69
		2	1	0.554	32,706
			2	0.557	33,008
			Average	0.556 ± 0.002	32,857 ± 214
BIAXIAL FILM	PET	1	1	0.588	35,669
			2	0.608	37,393
			Average	0.598 ± 0.014	36,531 ± 1,218
	PET0.5G	1	1	0.562	33,373
			2	0.567	33,853
			Average	0.565 ± 0.004	33,613 ± 339
	PET1.0G	1	1	0.541	31,632
			2	0.524	30,168
			Average	0.533 ± 0.012	30,900 ± 1,036

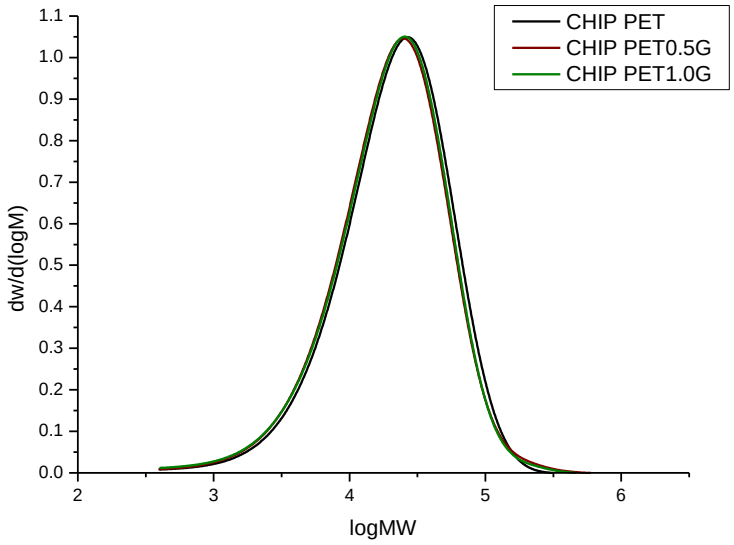

Figure 35 Molecular weight distribution plots of polymer and composite chip highlighting the effect of Garamite® loading on M_w values during synthesis.

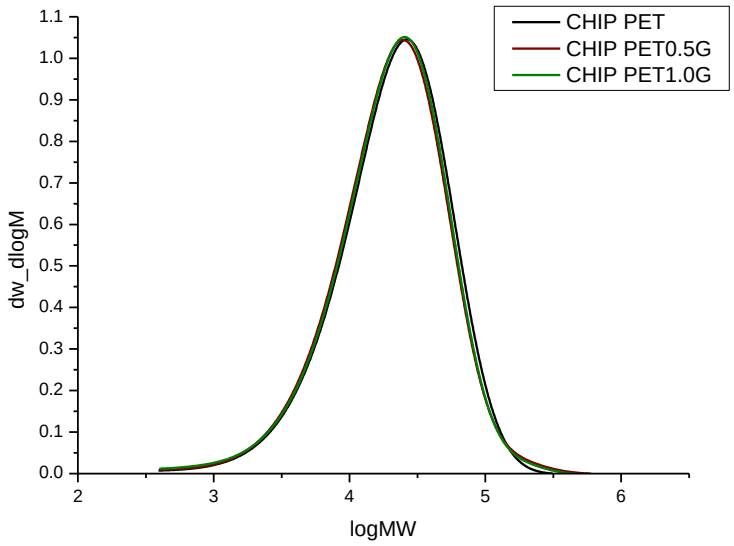

Figure 36 Replicate. Molecular weight distribution plots of polymer and composite chip highlighting the effect of Garamite® loading on M_w values during synthesis.

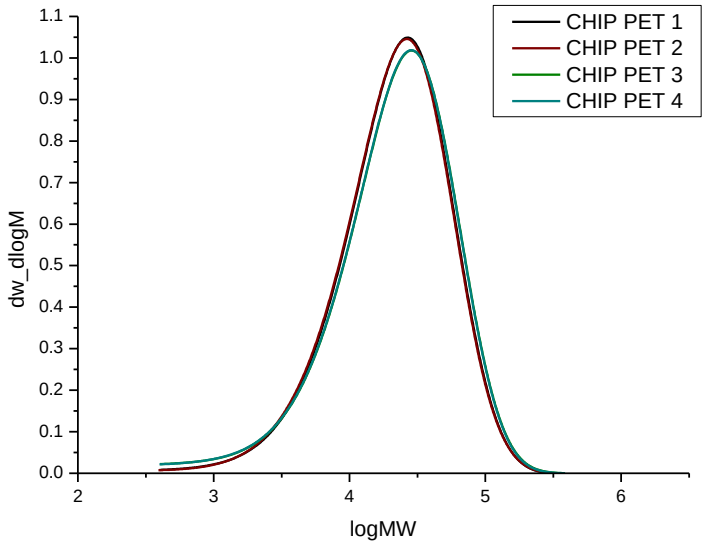

Figure 37 Overlay of PET chip samples illustrating repeatability.

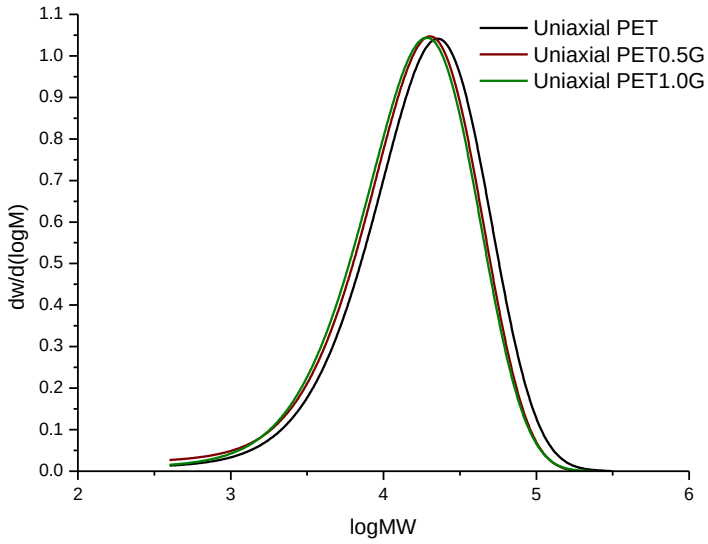

Figure 38 Molecular weight distribution plots of polymer and composite uniaxial film highlighting the effect of Garamite® loading on M_w values during synthesis.

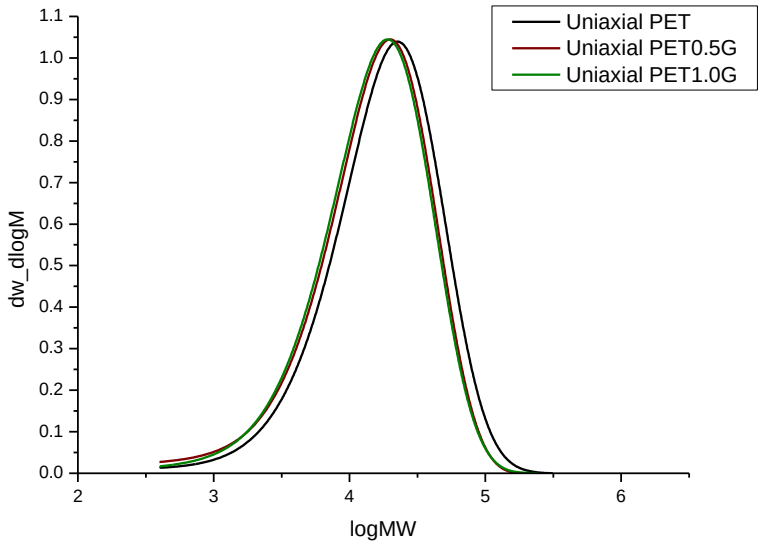

Figure 39 Replicate. Molecular weight distribution plots of polymer and composite uniaxial film highlighting the effect of Garamite® loading on M_w values during synthesis.

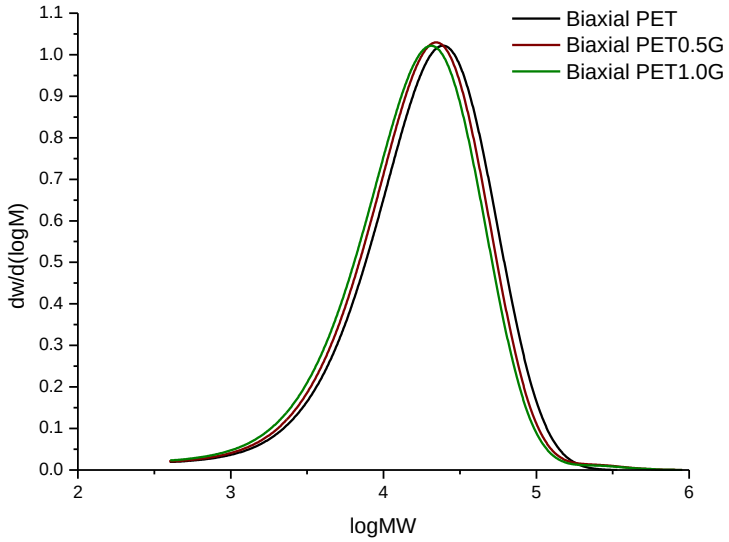

Figure 40 Molecular weight distribution plots of polymer and composite biaxial film highlighting the effect of Garamite® loading on M_w values during synthesis.

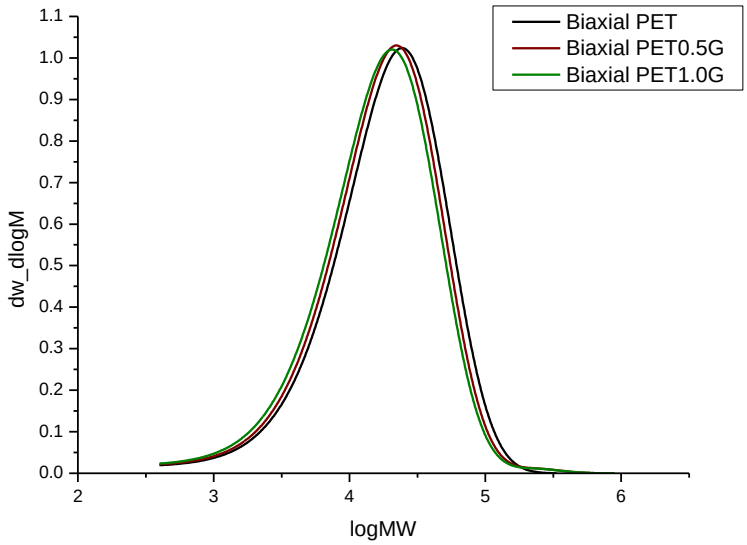

Figure 41 Replicate. Molecular weight distribution plots of polymer and composite biaxial film highlighting the effect of Garamite® loading on M_w values during synthesis.

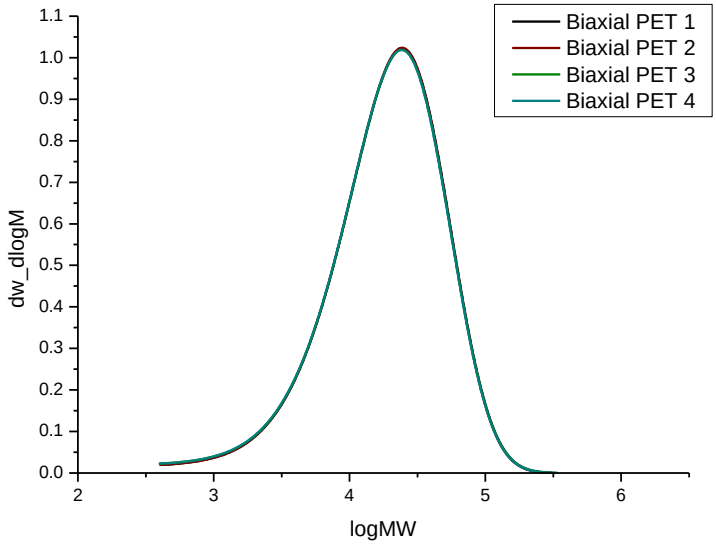

Figure 42 Overlay of PET biaxial film samples illustrating repeatability.

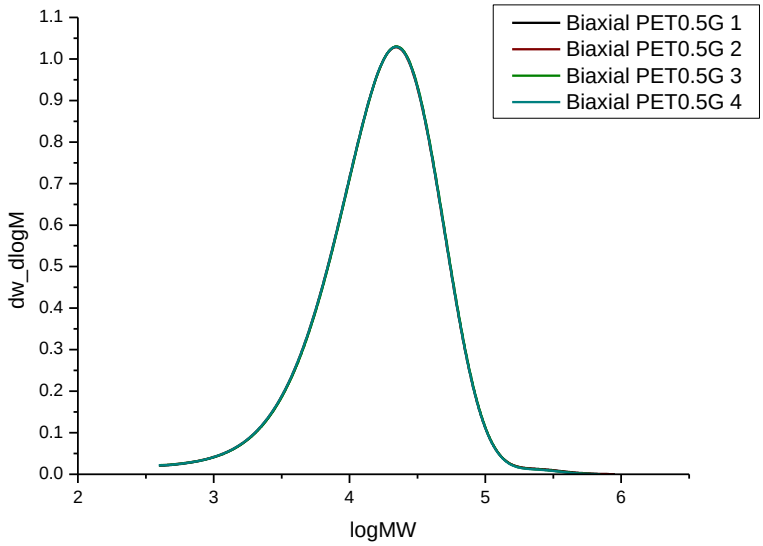

Figure 43 Overlay of PET0.5G biaxial film samples illustrating repeatability.

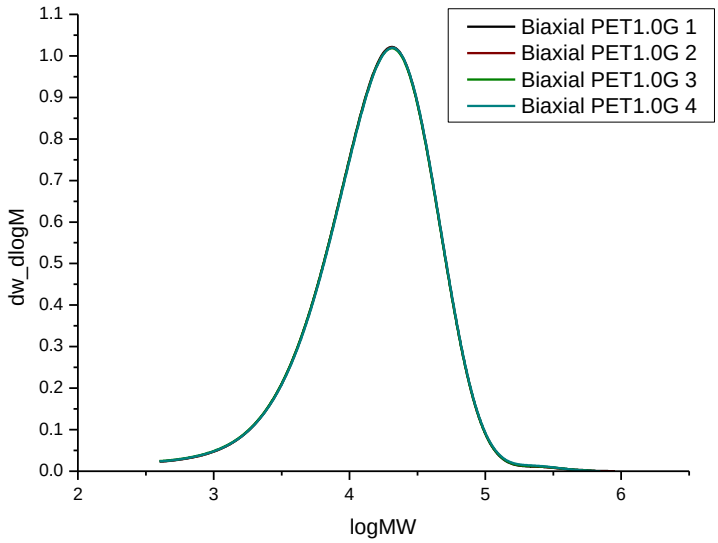

Figure 44 Overlay of PET1.0G biaxial film samples illustrating repeatability.

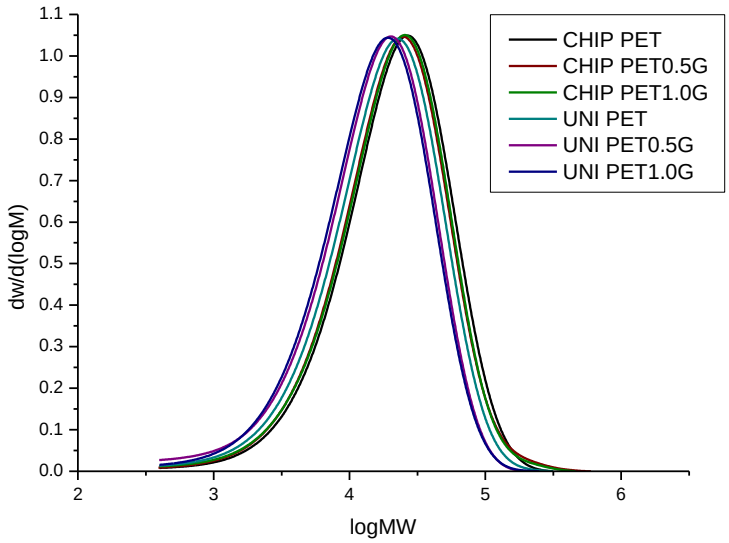

Figure 45 Molecular weight distribution plots of polymer and composite chip and uniaxial film highlighting the effect of unilateral stretching during melt processing on M_w values.

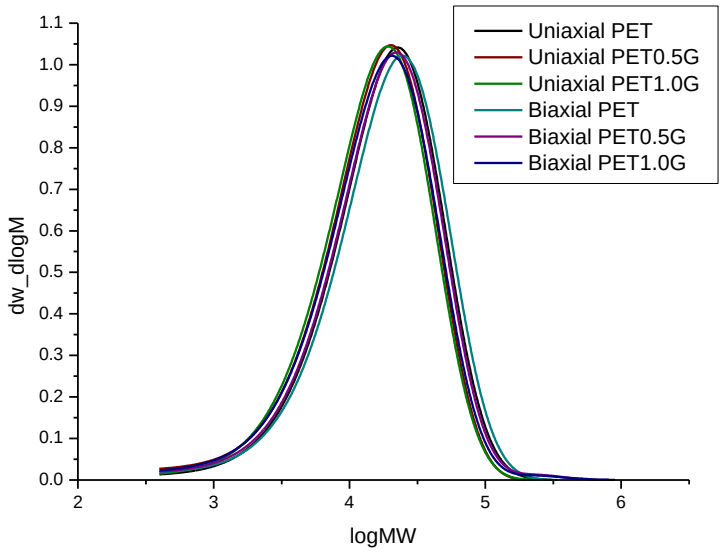

Figure 46 Molecular weight distribution plots of polymer and composite uniaxial and biaxial film highlighting the effect of bilateral stretching on M_w values.

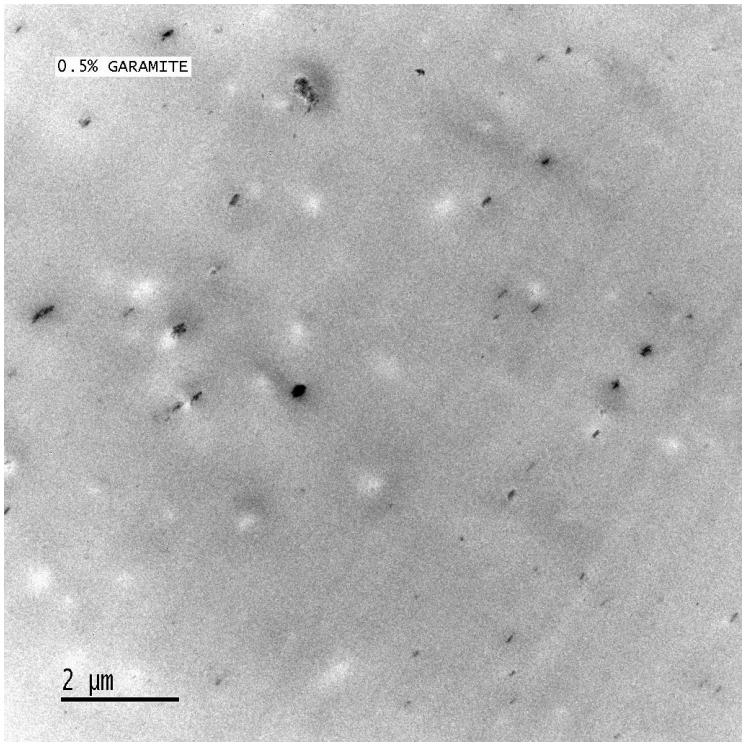

Figure 47 TEM image of PET0.5G uniaxial film at 2µm.

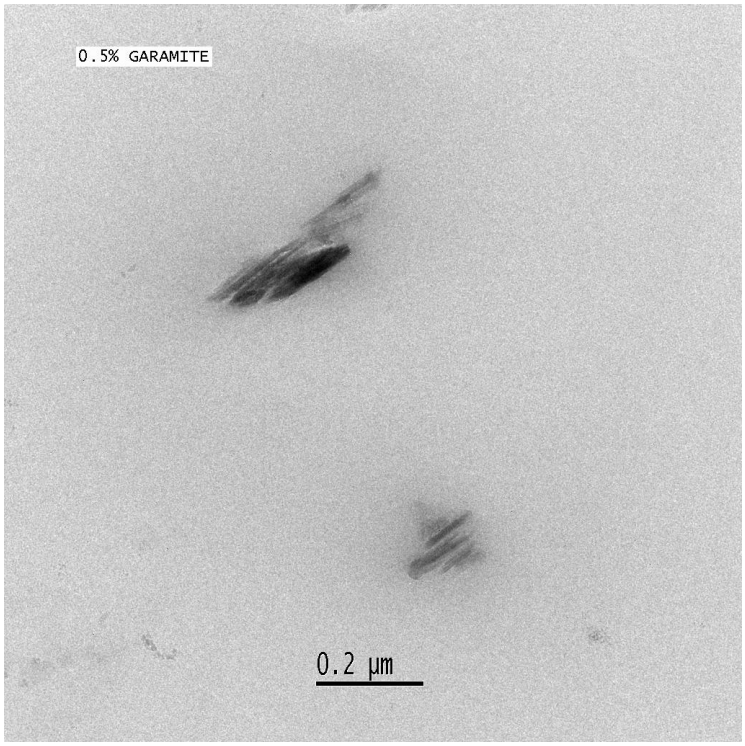

Figure 48 TEM image of PET0.5G uniaxial film at 0.2µm.

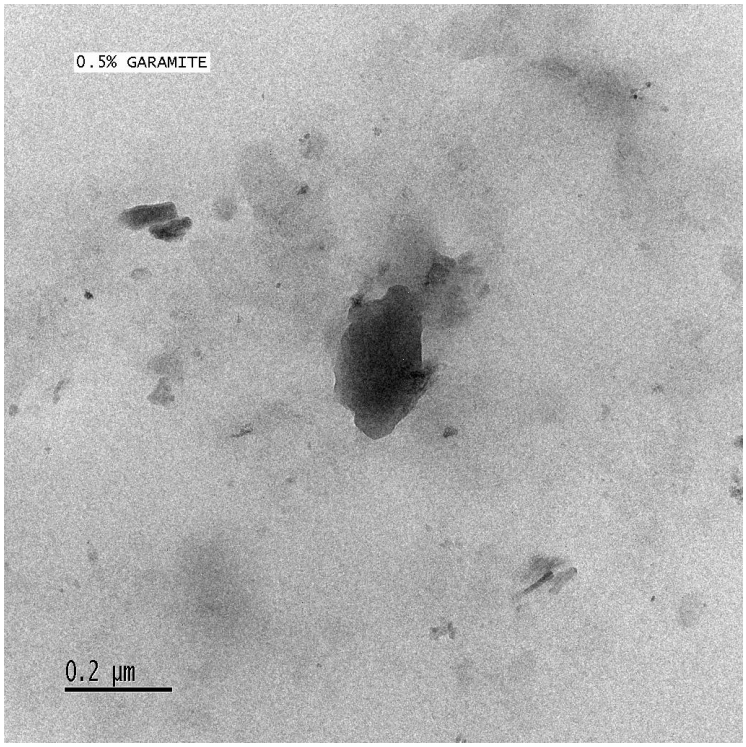

Figure 49 TEM image of PET0.5G uniaxial film at 0.2µm.

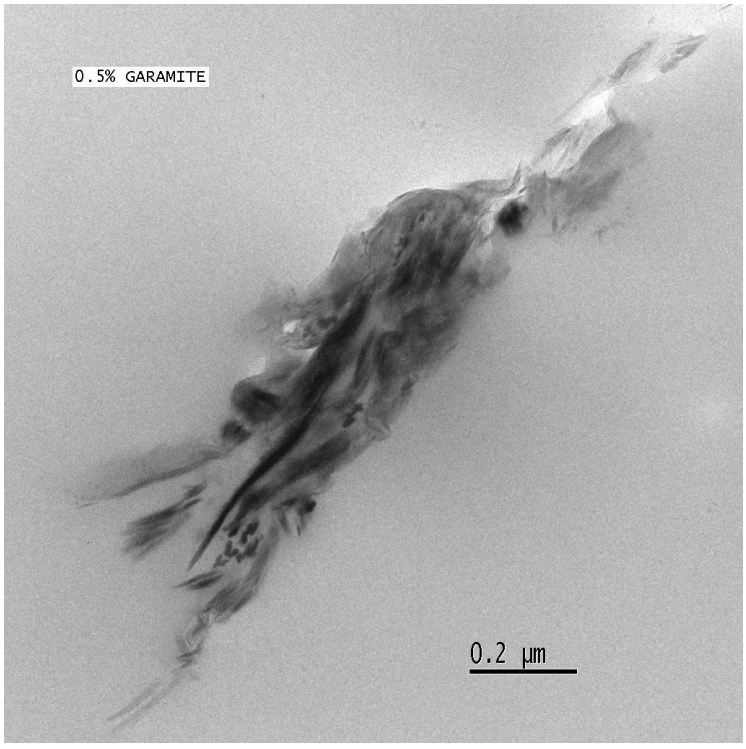

Figure 50 TEM image of PET0.5G uniaxial film at 0.2µm.

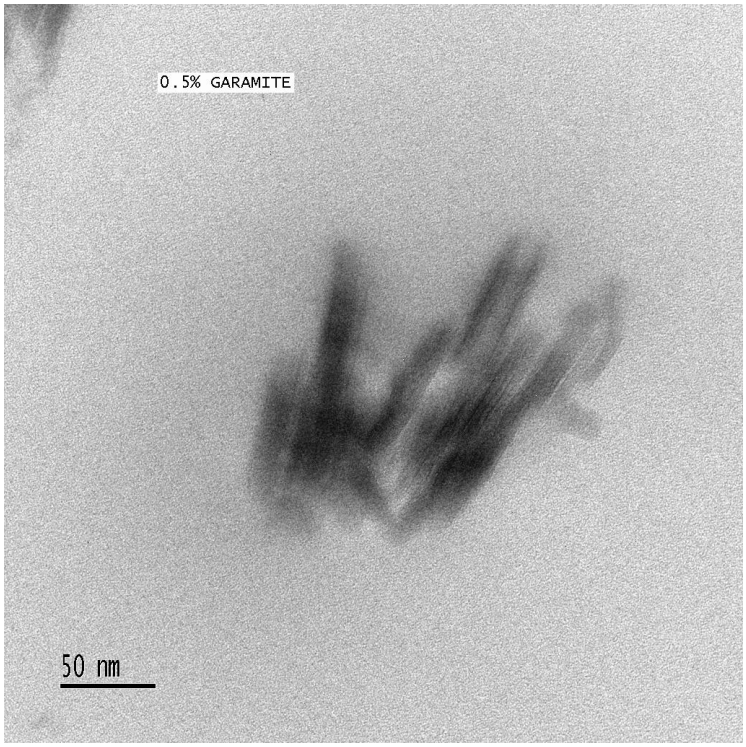

Figure 51 TEM image of PET0.5G uniaxial film at 50nm.

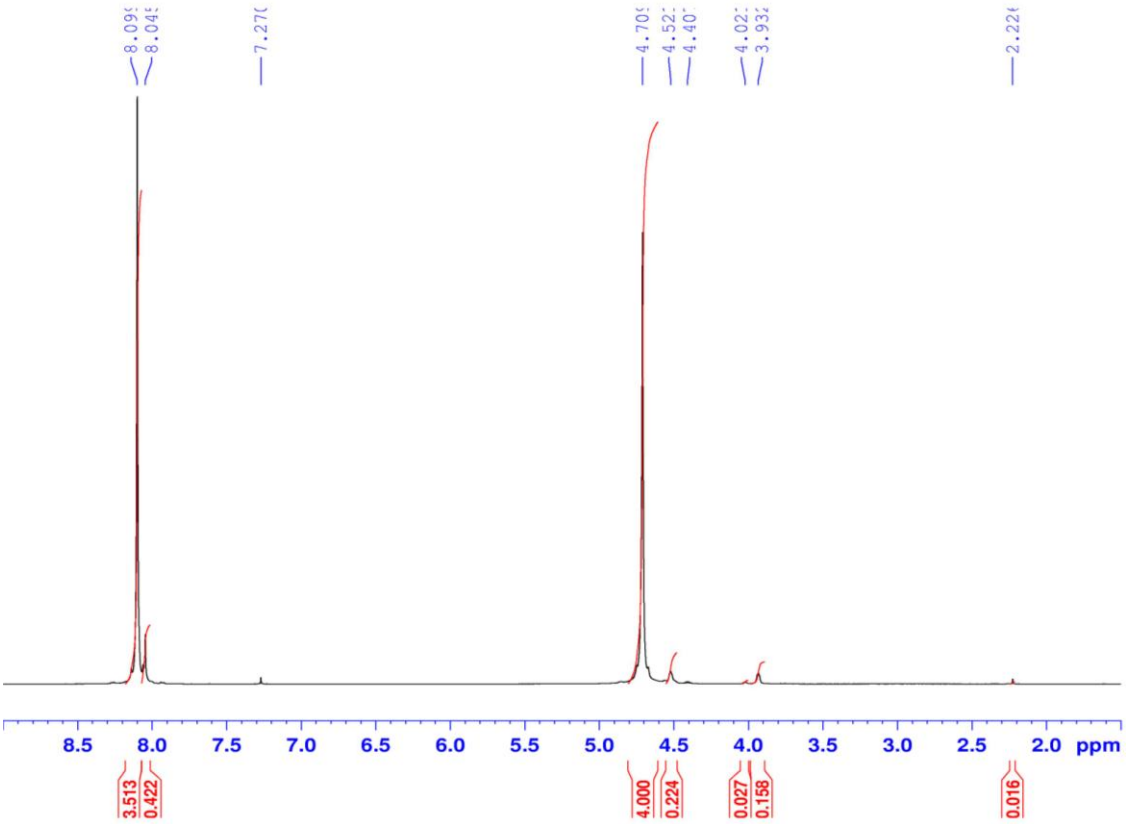

Figure 52 ^{1}H NMR spectra of PET0.5G CHIP in $CDCl_3$/HFIP

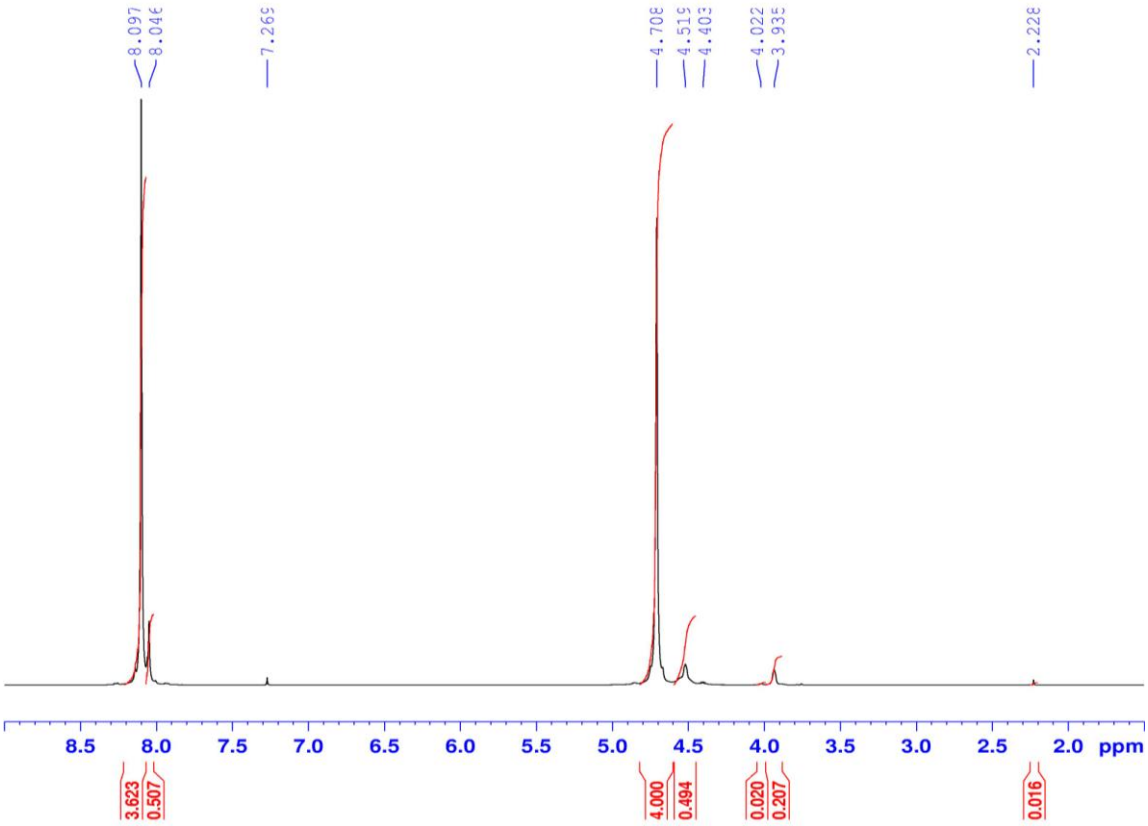

Figure 53 ^{1}H NMR spectra of PET1.0G CHIP in $CDCl_3$/HFIP

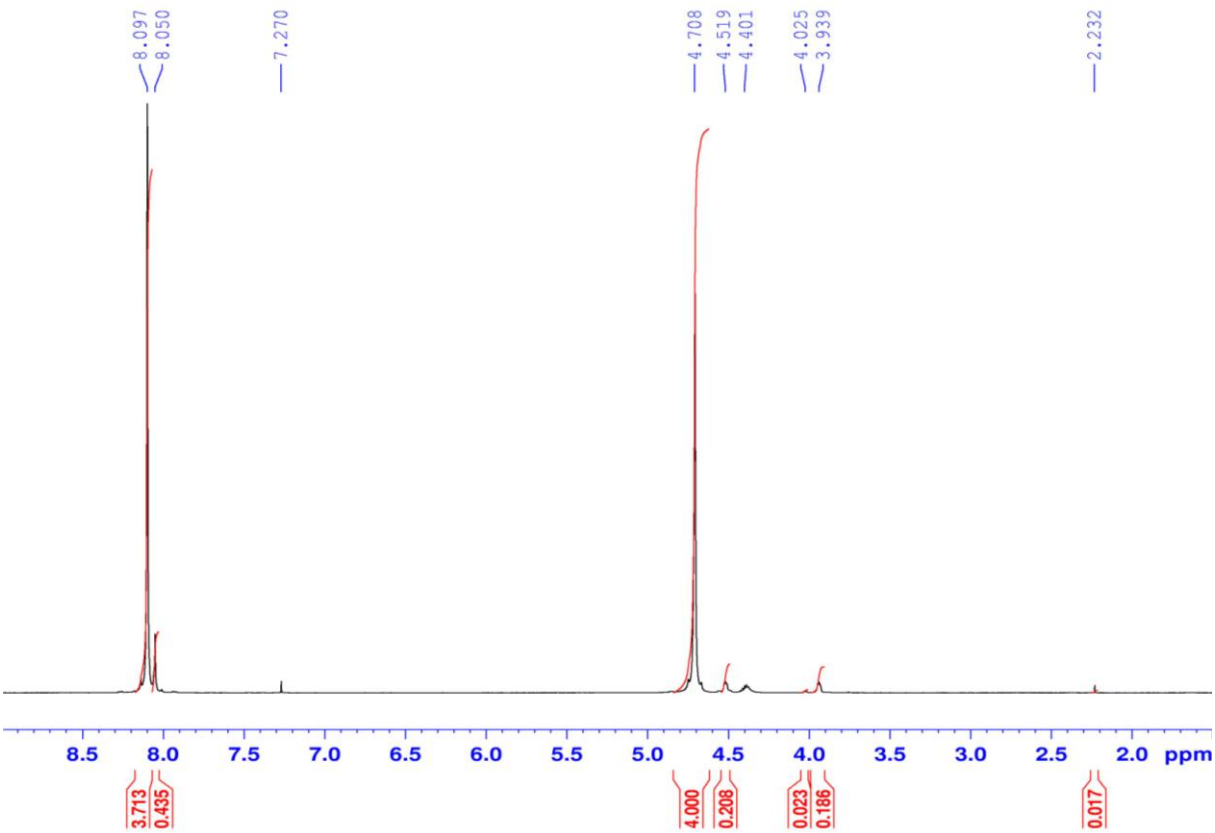

Figure 54 ^{1}H NMR spectra of PET UNIAXIAL FILM in $CDCl_3$/HFIP

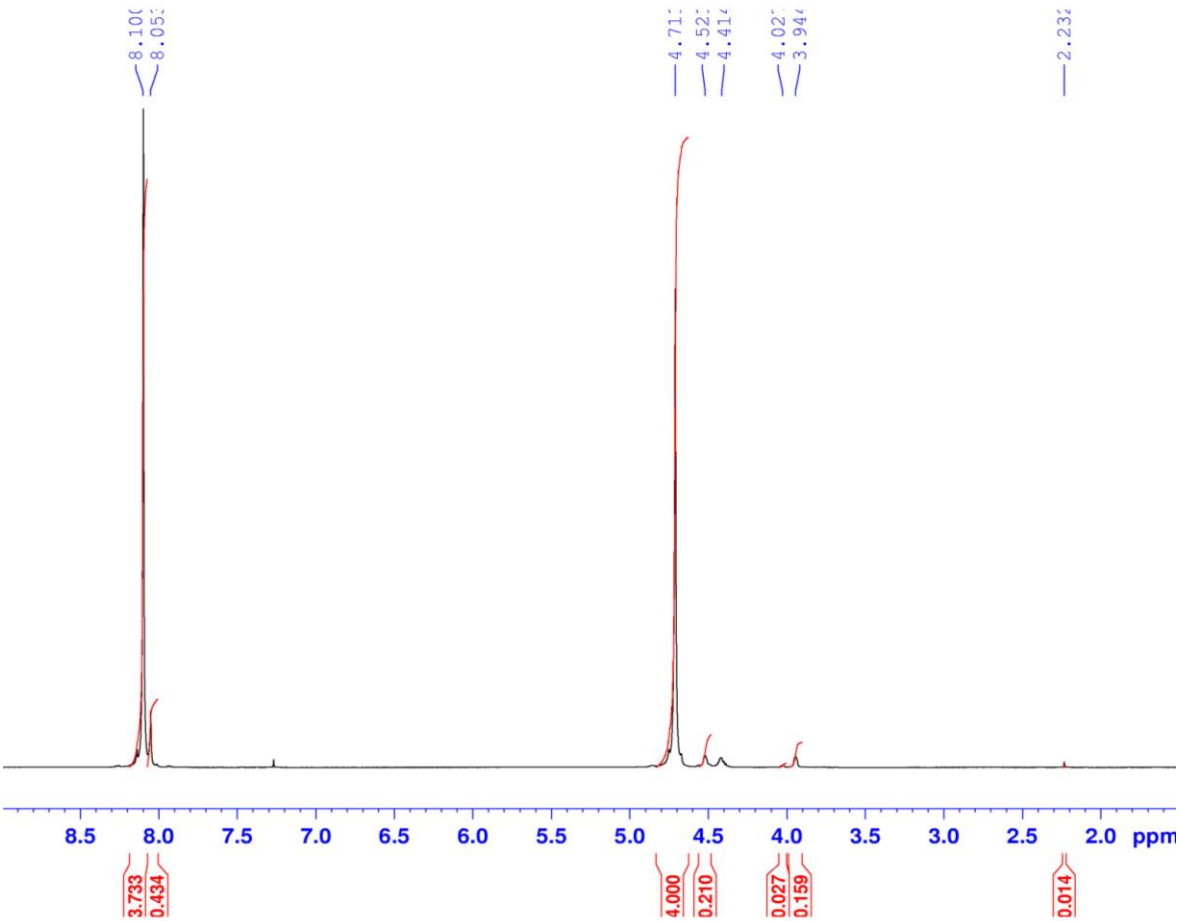

Figure 55 ^{1}H NMR spectra of PET0.5G UNIAXIAL FILM in $CDCl_3$/HFIP

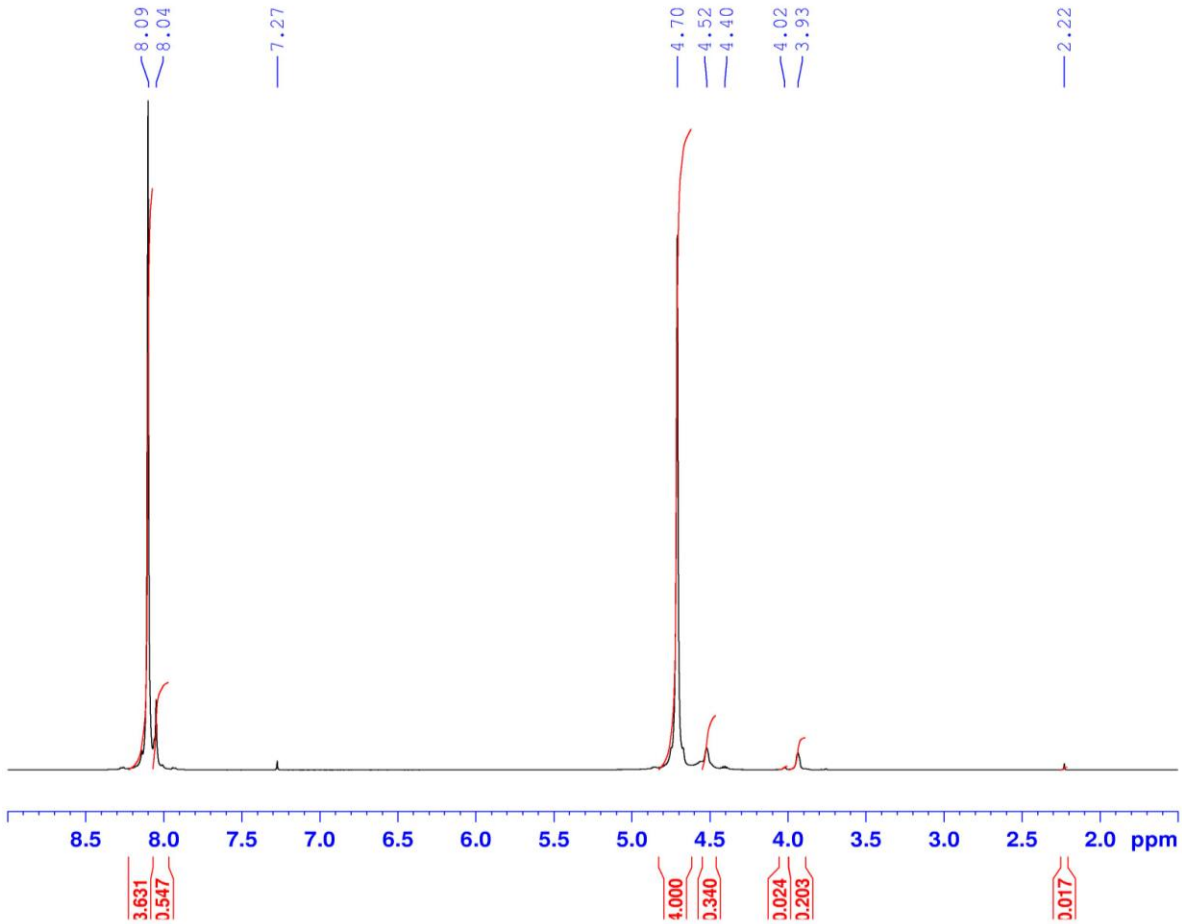

Figure 56 ^{1}H NMR spectra of PET1.0G UNIAXIAL FILM in $CDCl_3$/HFIP

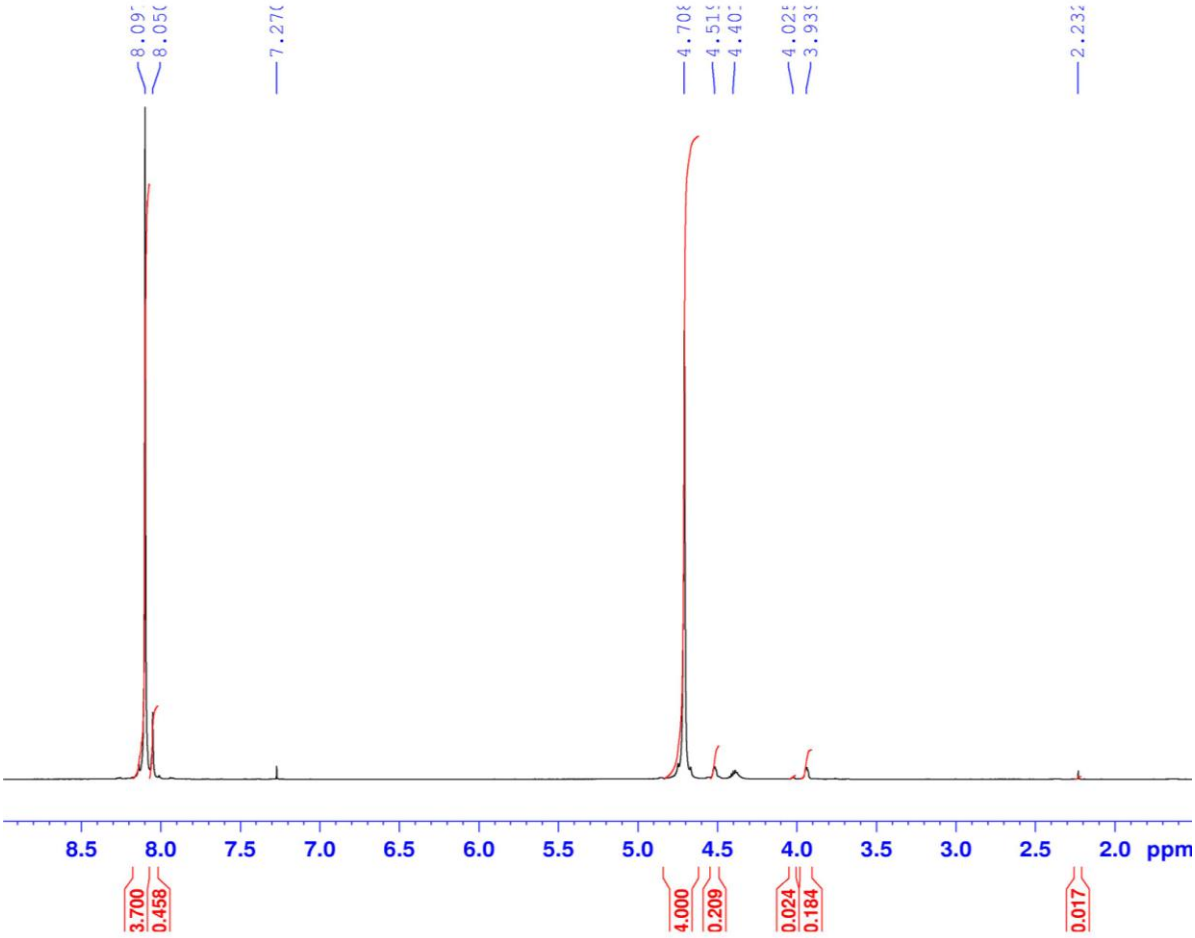

Figure 57 ^{1}H NMR spectra of PET BIAXIAL FILM in $CDCl_3$/HFIP

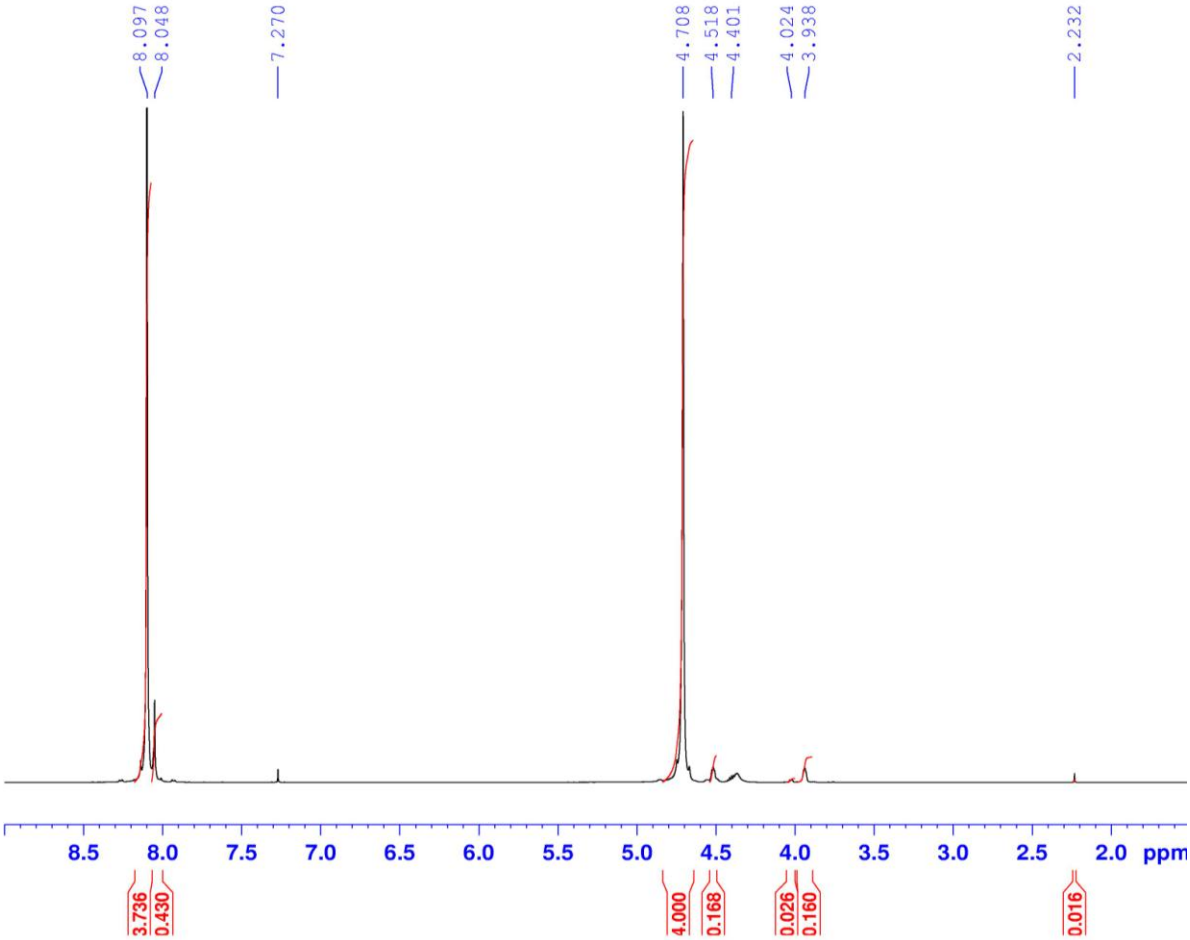

Figure 58 ^{1}H NMR spectra of PET0.5G BIAXIAL FILM in $CDCl_3$/HFIP

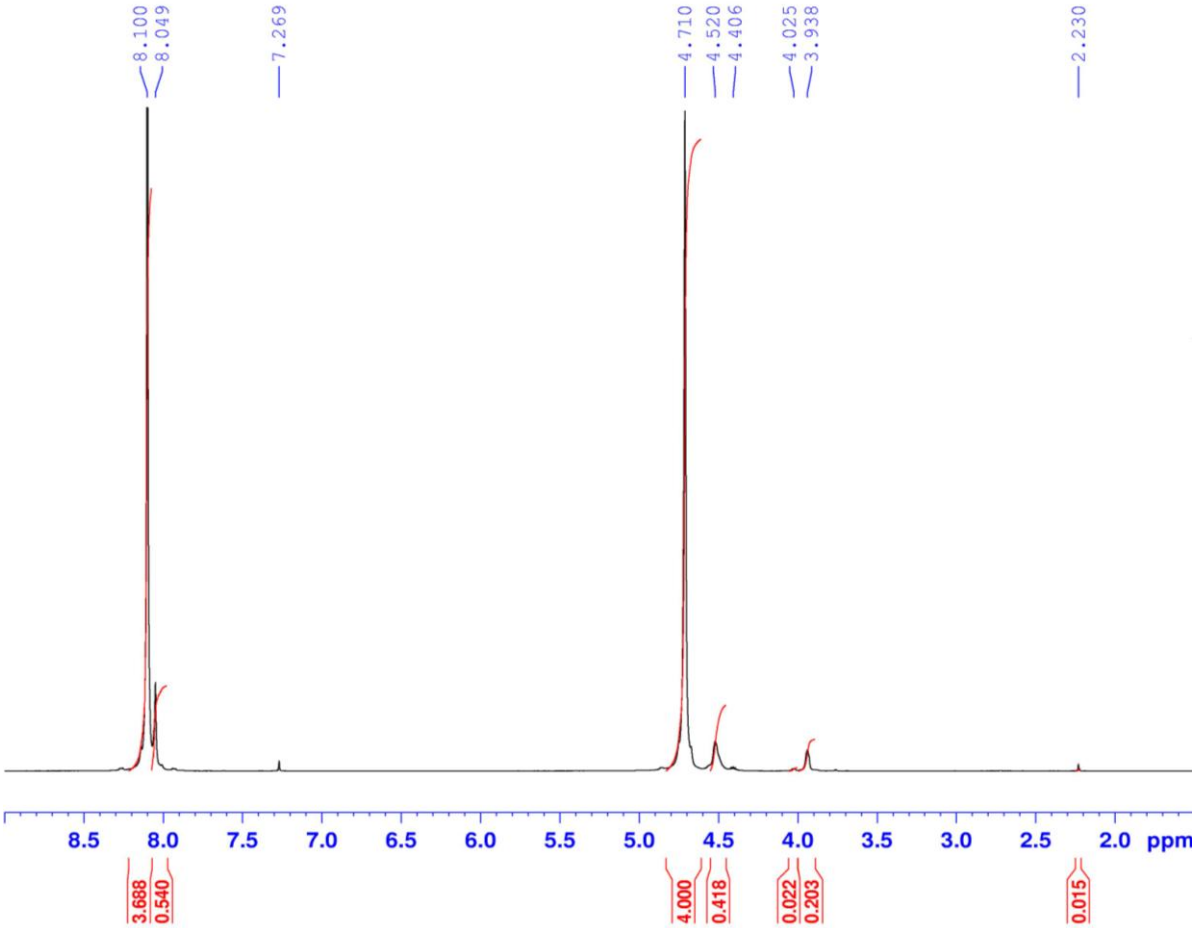

Figure 59 ^{1}H NMR spectra of PET1.0G BIAXIAL FILM in $CDCl_3$/HFIP

APPENDIX 4: CRYSTALLISATION

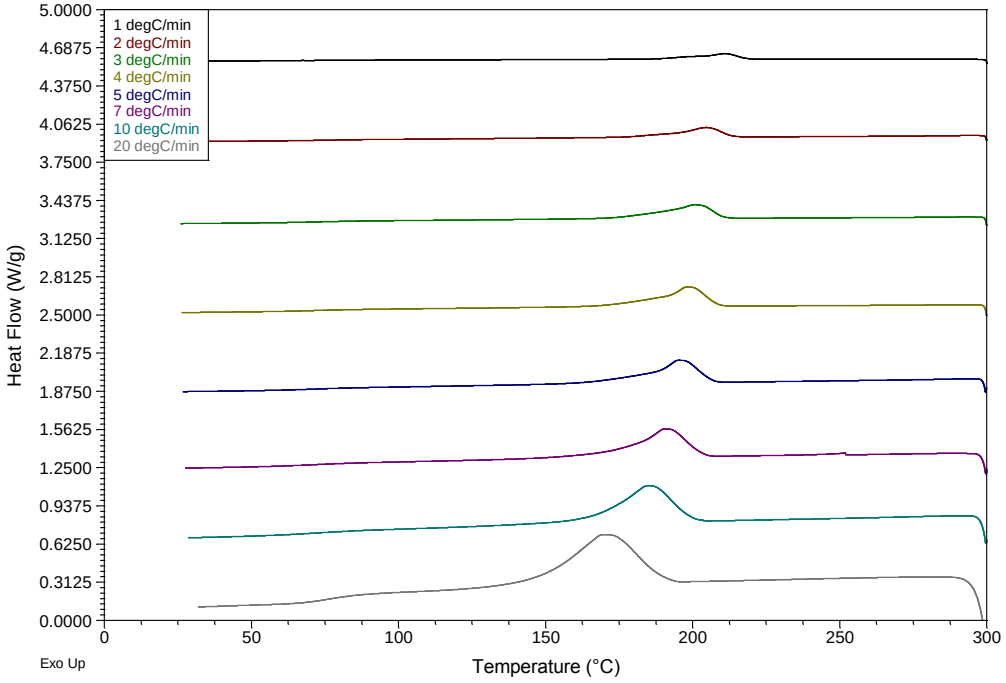

Figure 60 Replicate. DSC thermogram of dynamic crystallisation in PET chip. Cooling rates range between 1 ºC min^{-1} and 20 ºC min^{-1}.

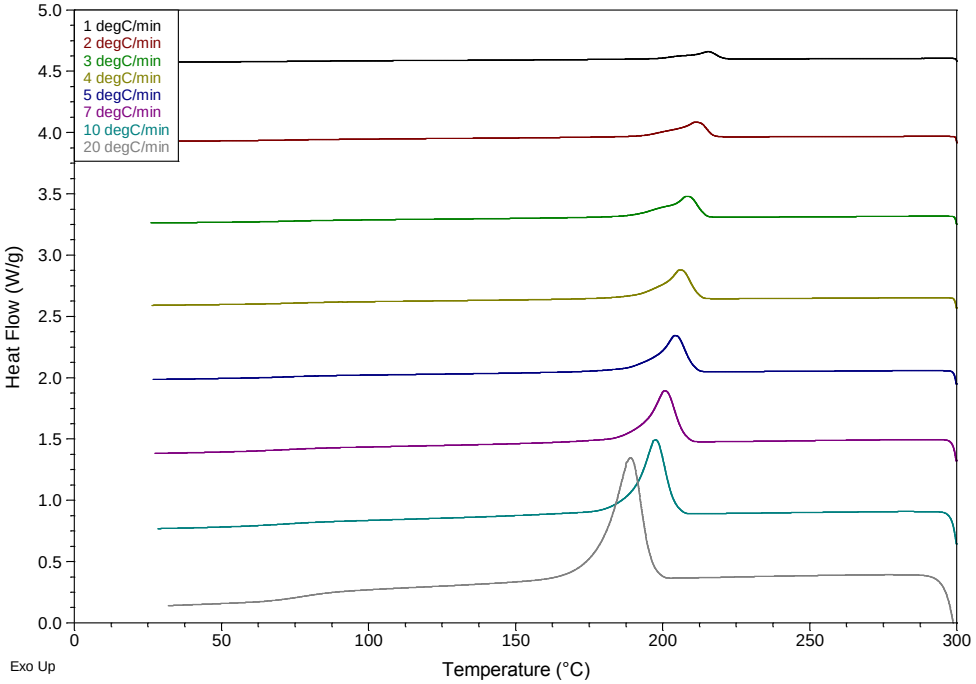

Figure 61 Replicate. DSC thermogram of dynamic crystallisation in PET0.5G chip. Cooling rates range between 1 ºC min^{-1} and 20 ºC min^{-1}.

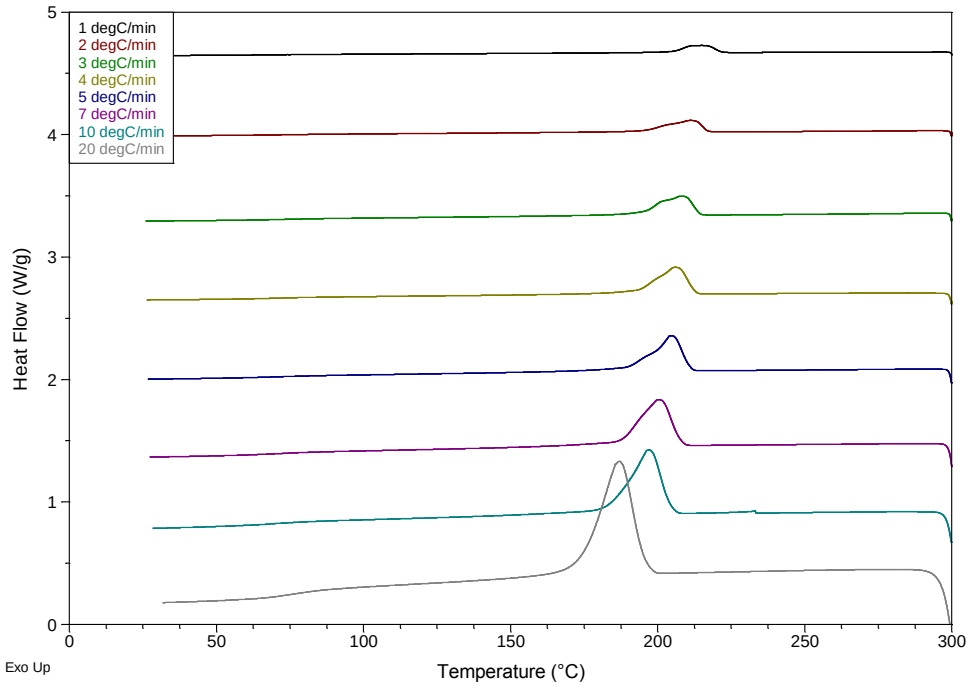

Figure 62 Replicate. DSC thermogram of dynamic crystallisation in PET1.0G chip. Cooling rates range between 1 ºC min^{-1} and 20 ºC min^{-1}.

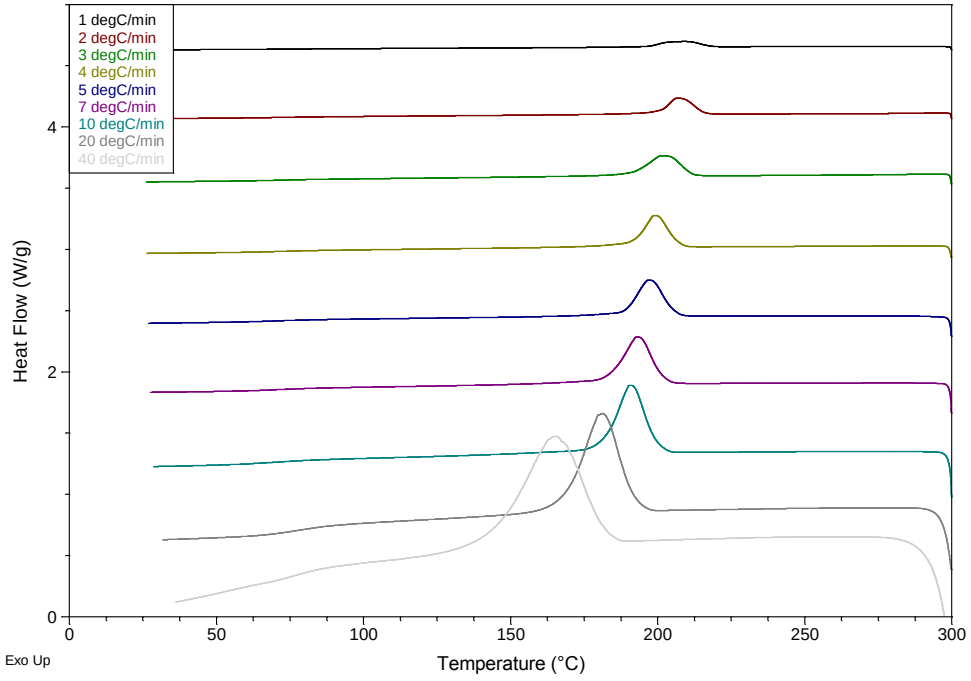

Figure 63 DSC thermogram of dynamic crystallisation in PET uniaxial. Cooling rates range between 1 ºC min^{-1} and 20 ºC min^{-1}.

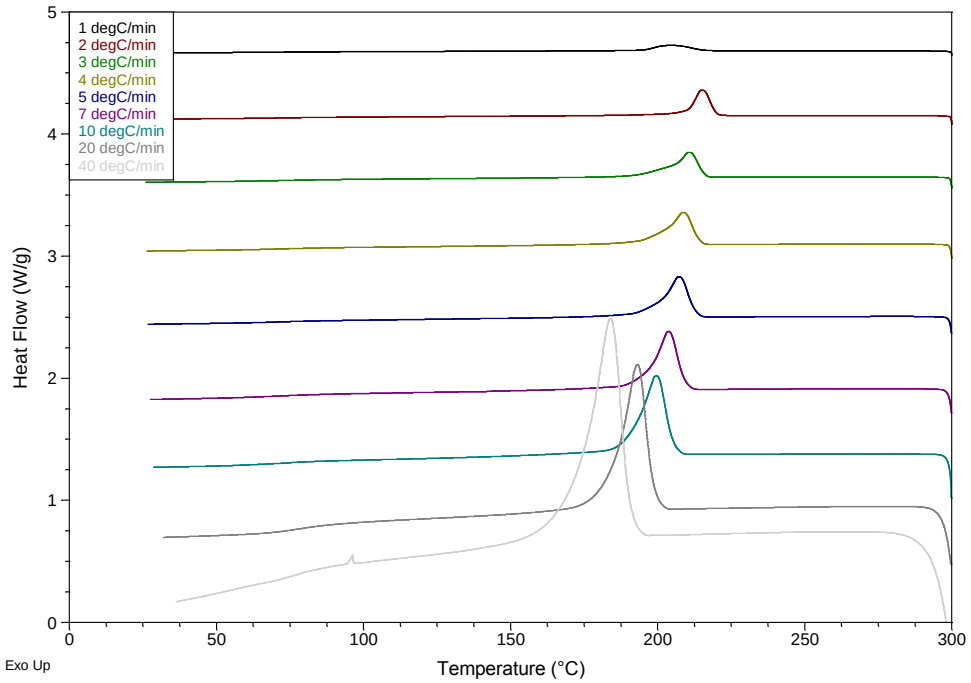

Figure 64 DSC thermogram of dynamic crystallisation in PET0.5G uniaxial. Cooling rates range between 1 ºC min^{-1} and 20 ºC min^{-1}.

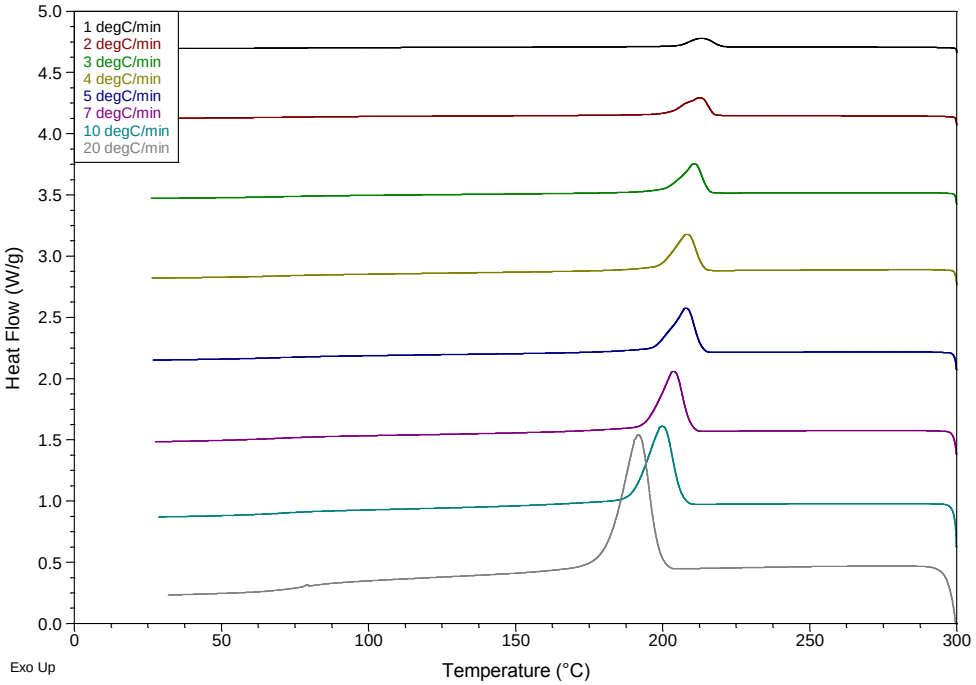

Figure 65 DSC thermogram of dynamic crystallisation in PET1.0G uniaxial. Cooling rates range between 1 ºC min^{-1} and 20 ºC min^{-1}.

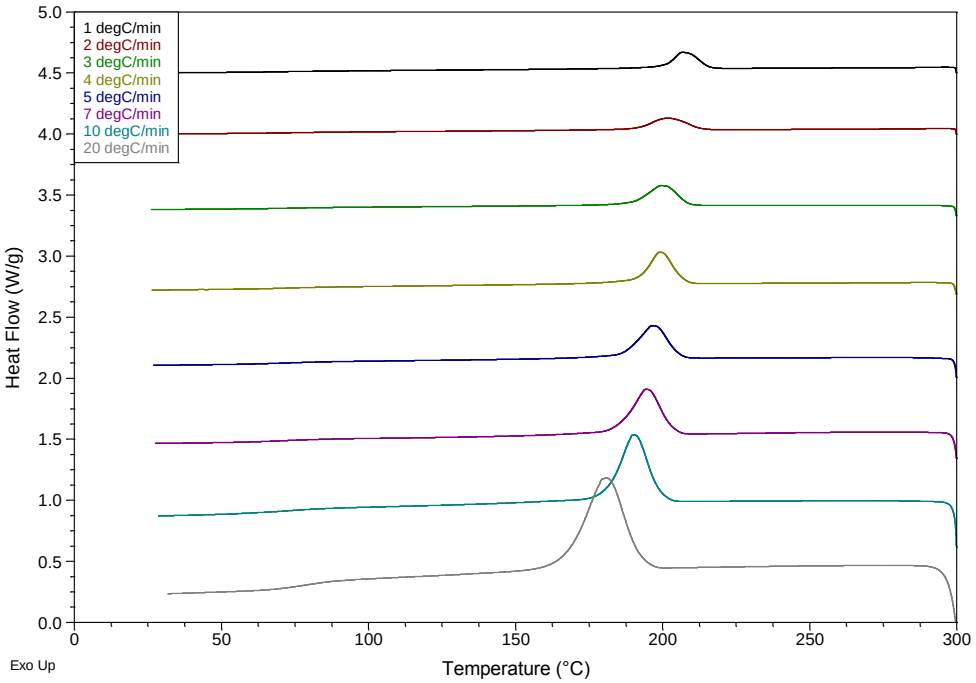

Figure 66 Replicate. DSC thermogram of dynamic crystallisation in PET uniaxial. Cooling rates range between 1 ºC min^{-1} and 20 ºC min^{-1}.

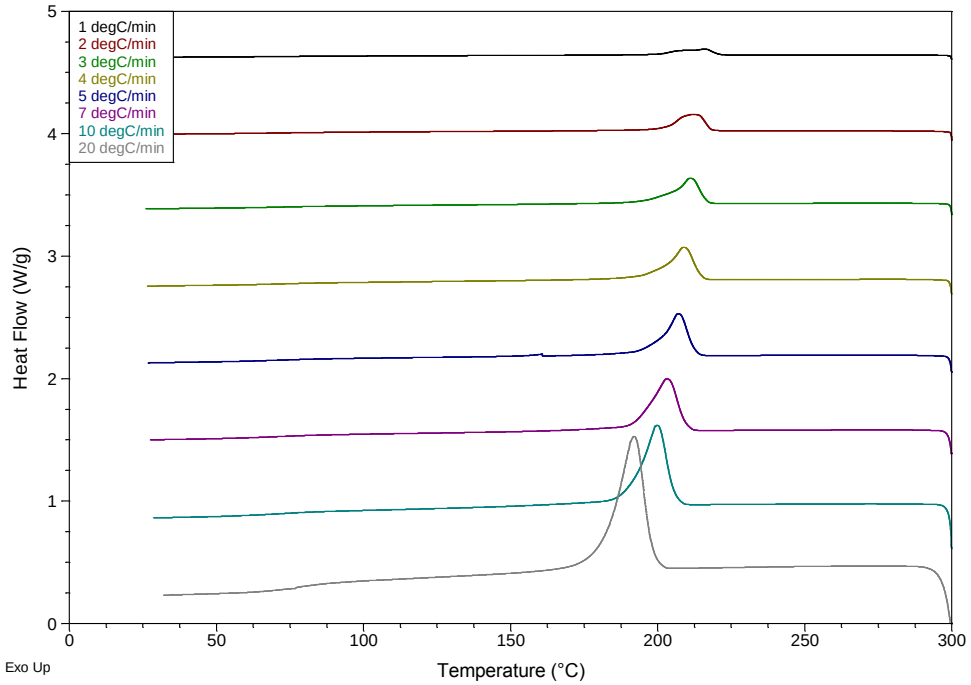

Figure 67 Replicate. DSC thermogram of dynamic crystallisation in PET 0.5G uniaxial. Cooling rates range between 1 ºC min^{-1} and 20 ºC min^{-1}.

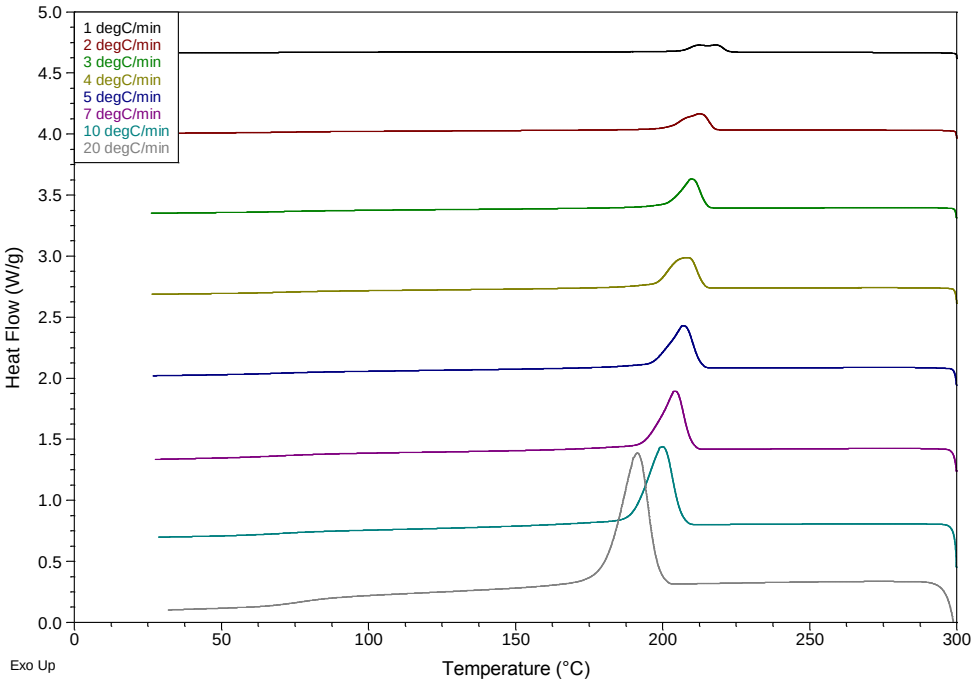

Figure 68 Replicate. DSC thermogram of dynamic crystallisation in PET 1.0G uniaxial. Cooling rates range between 1 ºC min^{-1} and 20 ºC min^{-1}.

Table 8 Enthalpies of crystallisation for samples under various cooling rate

Cooling rate / ºC min^{-1}	Replicate	ΔH_c / J g^{-1}					
		Amorphous chip			Uniaxial film		
		PET	PET0.5G	PET1.0G	PET	PET0.5G	PET1.0G
1	1	46.19	51.89	48.34	43.74	42.51	45.04
	2	47.70	50.18	47.32	44.40	46.88	43.12
	average	46.95	51.04	47.83	44.07	44.70	44.08
2	1	45.52	51.36	44.87	45.22	47.51	44.25
	2	45.36	51.76	49.20	43.85	46.45	46.13
	average	45.44	51.56	47.04	44.54	46.98	45.19
3	1	46.86	46.92	47.48	47.32	48.00	46.88
	2	46.67	49.56	46.45	42.83	47.21	45.29
	average	46.77	48.24	46.97	45.08	47.61	46.09
4	1	47.06	47.64	45.04	43.37	46.78	45.11
	2	45.61	45.11	43.47	43.62	46.46	47.44
	average	46.34	46.38	44.26	43.50	46.62	46.28
5	1	46.61	47.20	44.30	41.18	44.66	45.51
	2	47.11	42.90	44.20	41.70	44.29	45.02
	average	46.86	45.05	44.25	41.44	44.48	45.27
7	1	44.86	45.05	44.82	42.45	42.39	44.50
	2	45.51	42.96	44.23	41.58	42.99	45.03
	average	45.19	44.01	44.53	42.02	42.69	44.77
10	1	41.56	43.90	42.83	42.66	43.19	44.45
	2	41.02	40.99	42.10	41.48	42.79	45.24
	average	41.29	42.45	42.47	42.07	42.99	44.85
20	1	33.63	41.50	40.85	38.09	39.96	40.55
	2	34.33	39.98	40.32	37.52	39.17	39.30
	average	33.98	40.74	40.59	37.81	39.57	39.93

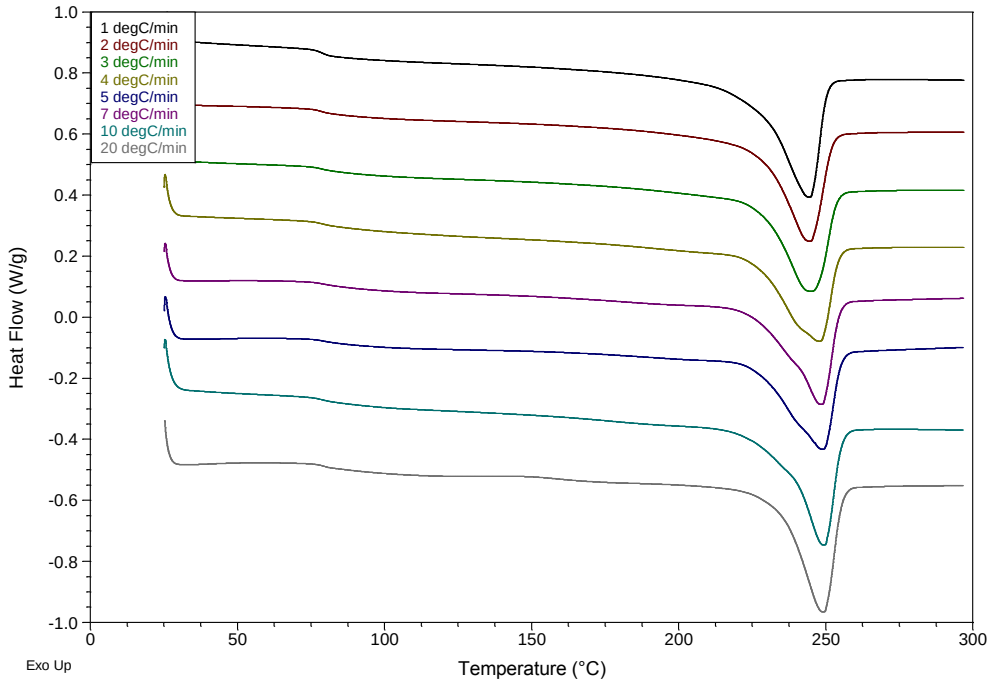

Figure 69 Replicate. DSC thermogram of the dynamic crystalline melting of PET chip after various dynamic cooling rates. The heating rate employed was 10 ºC min^{-1}.

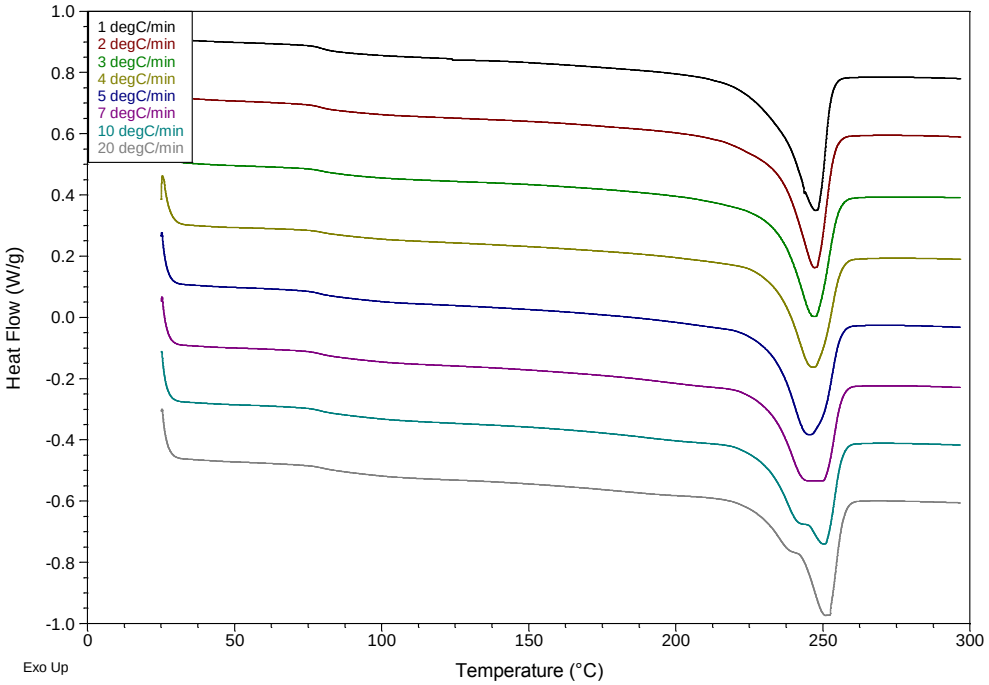

Figure 70 Replicate. DSC thermogram of the dynamic crystalline melting of PET0.5G chip after various dynamic cooling rates. The heating rate employed was 10 ºC min^{-1}.

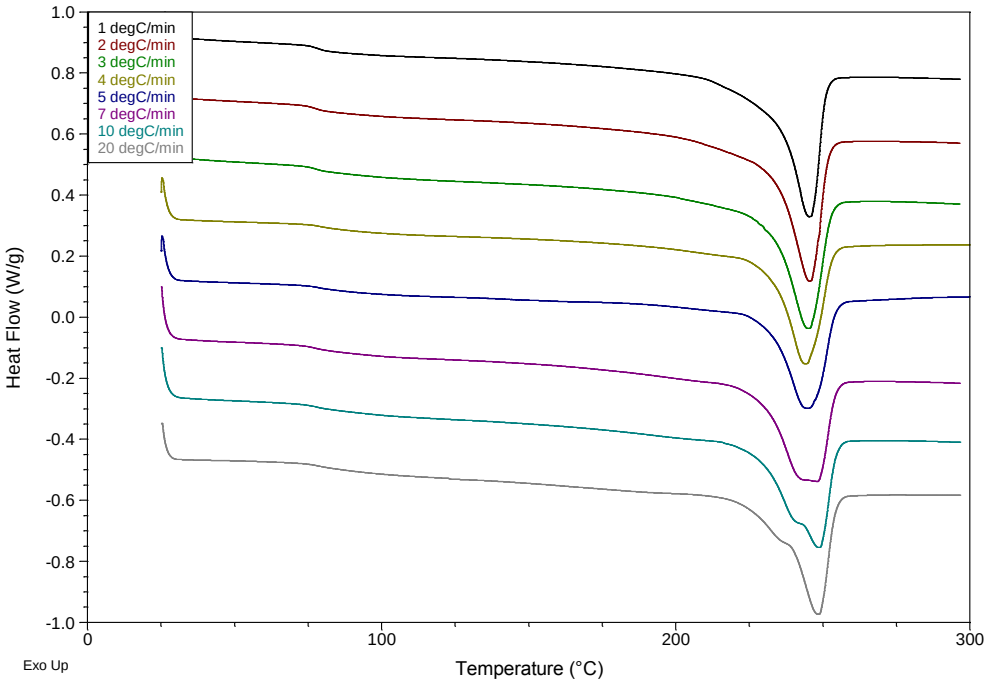

Figure 71 Replicate. DSC thermogram of the dynamic crystalline melting of PET1.0G chip after various dynamic cooling rates. The heating rate employed was 10 ºC min^{-1}.

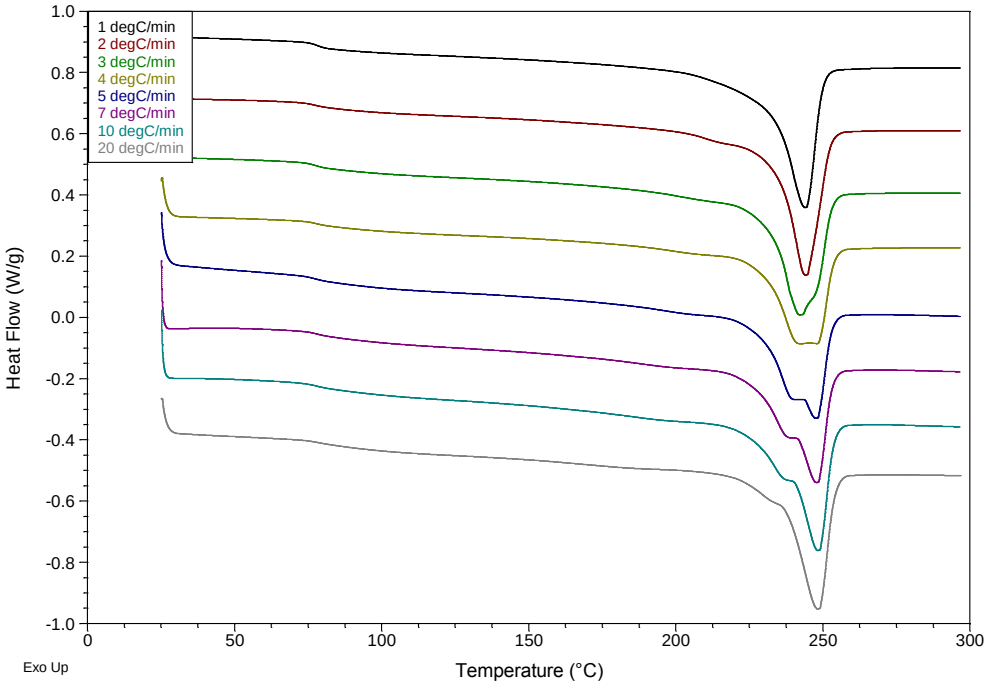

Figure 72 DSC thermogram of the dynamic crystalline melting of PET uniaxial film after various dynamic cooling rates. The heating rate employed was 10 ºC min^{-1}.

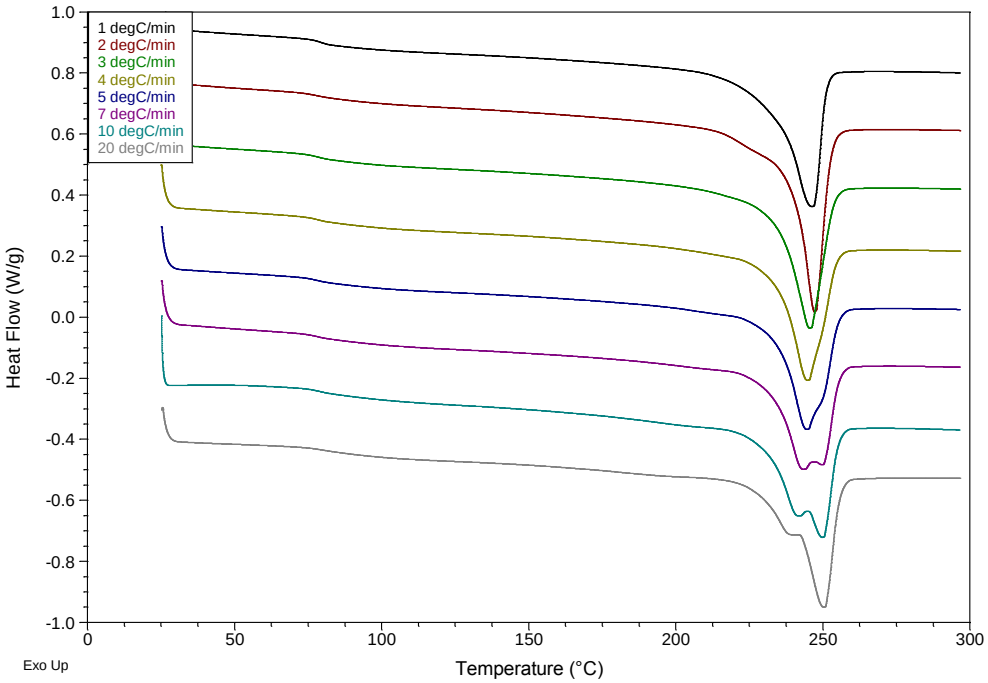

Figure 73 DSC thermogram of the dynamic crystalline melting of PET0.5G uniaxial film after various dynamic cooling rates. The heating rate employed was 10 ºC min^{-1}.

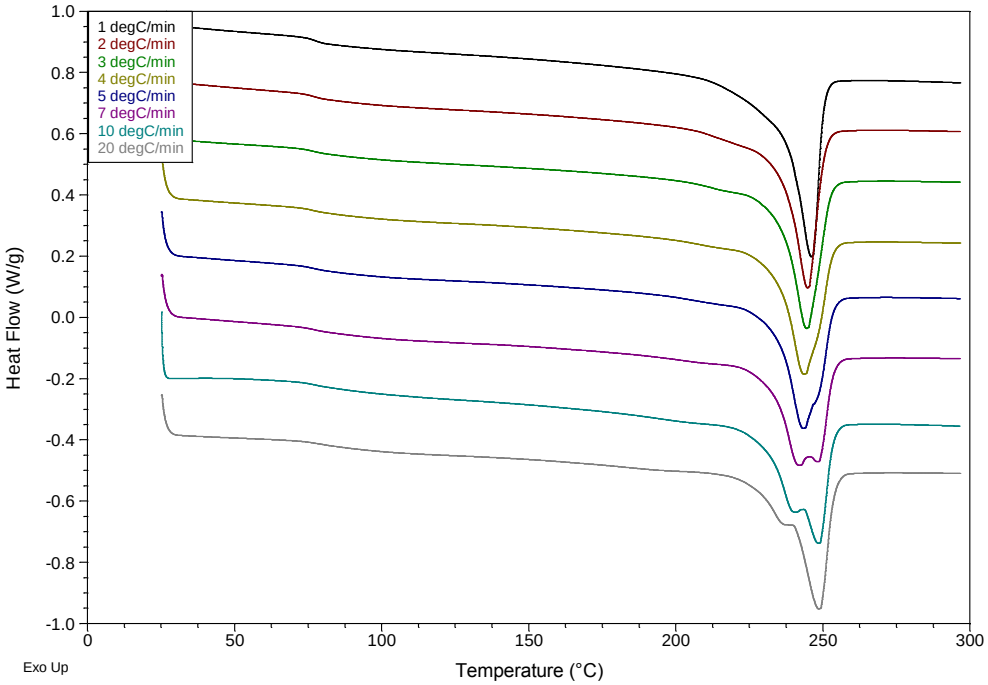

Figure 74 DSC thermogram of the dynamic crystalline melting of PET1.0G uniaxial film after various dynamic cooling rates. The heating rate employed was 10 ºC min^{-1}.

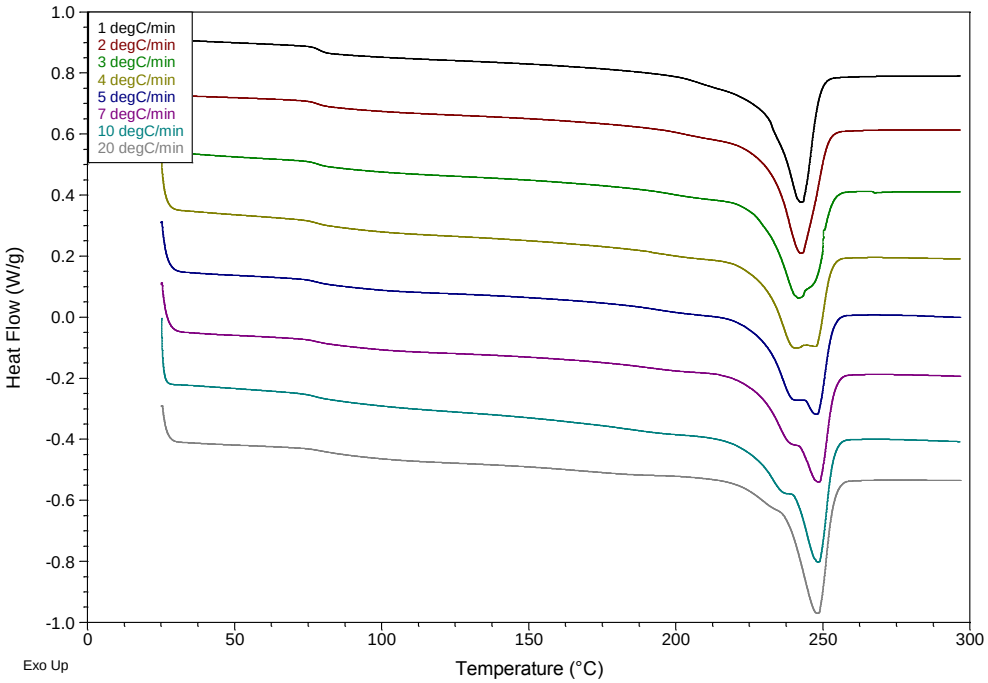

Figure 75 Replicate. DSC thermogram of the dynamic crystalline melting of PET uniaxial film after various dynamic cooling rates. The heating rate employed was 10 ºC min^{-1}.

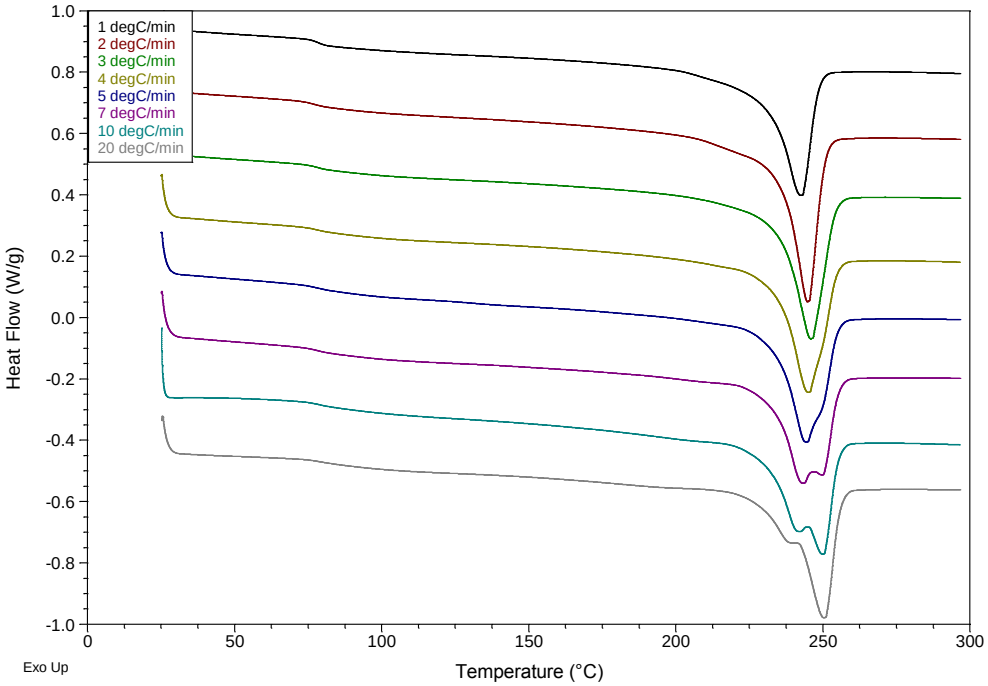

Figure 76 Replicate. DSC thermogram of the dynamic crystalline melting of PET0.5G uniaxial film after various dynamic cooling rates. The heating rate employed was 10 ºC min^{-1}.

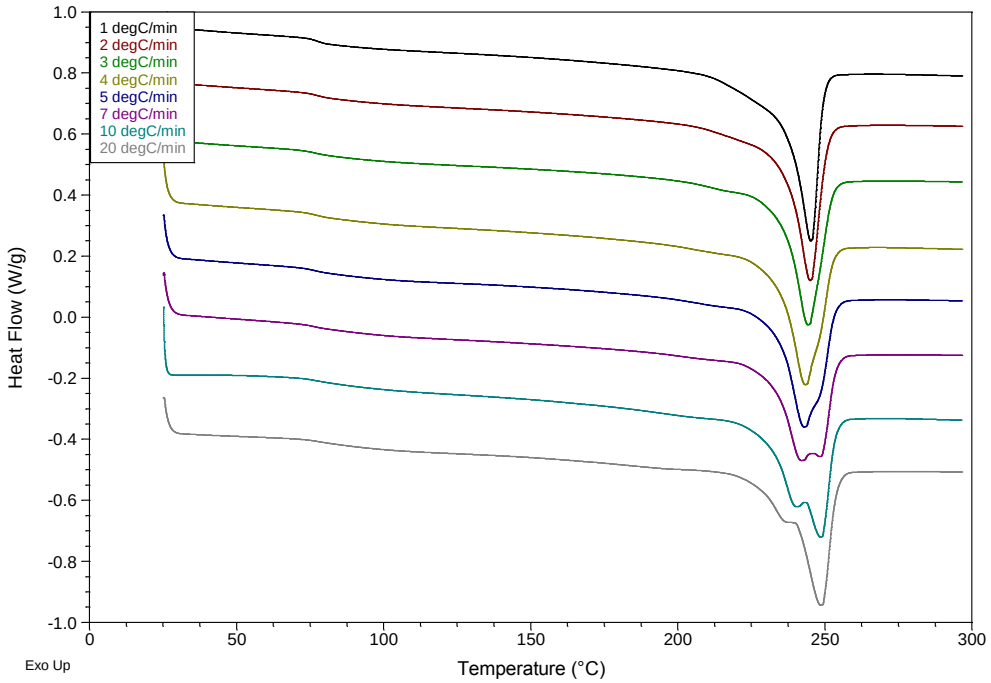

Figure 77 Replicate. DSC thermogram of the dynamic crystalline melting of PET1.0G uniaxial film after various dynamic cooling rates. The heating rate employed was 10 ºC min^{-1}.

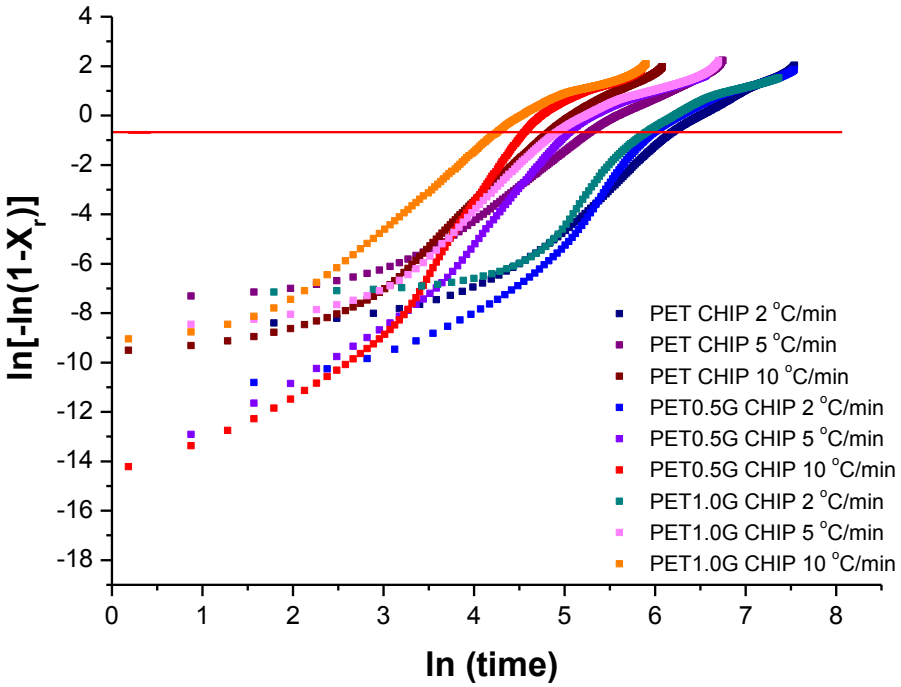

Figure 78 Replicate. Modified Avrami plots relating to the dynamic crystallisation of PET, PET0.5G and PET1.0G uniaxial film. The red line represents a crystallinity of 40% and the limits of the Avrami model.

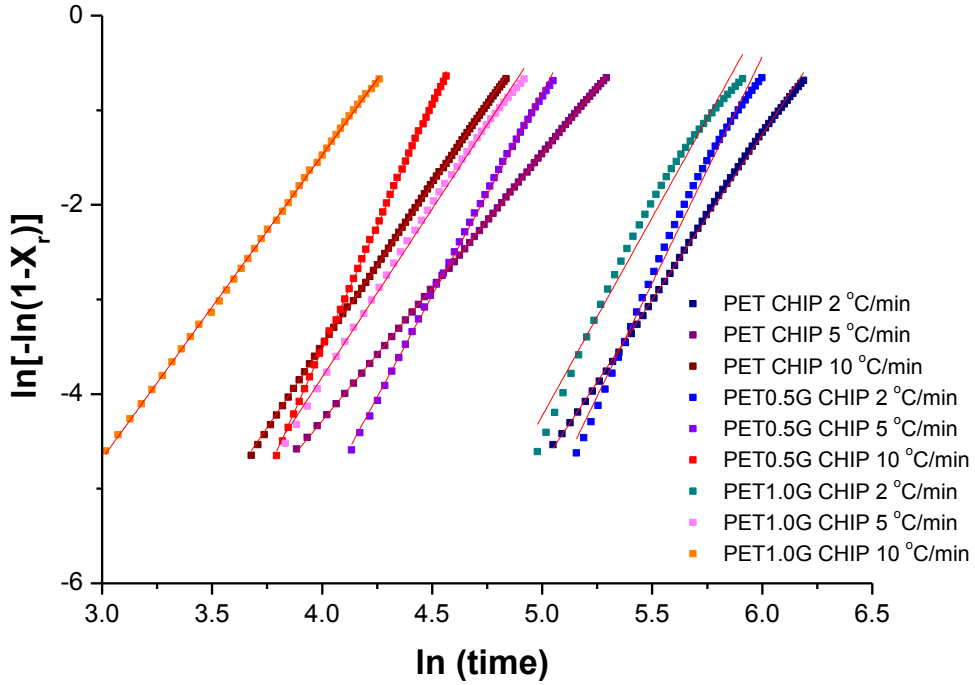

Figure 79 Replicate. Modified Avrami plots relating to the dynamic crystallisation of PET, PET0.5G and PET1.0G chip at crystallinities of between 1% and 40%.

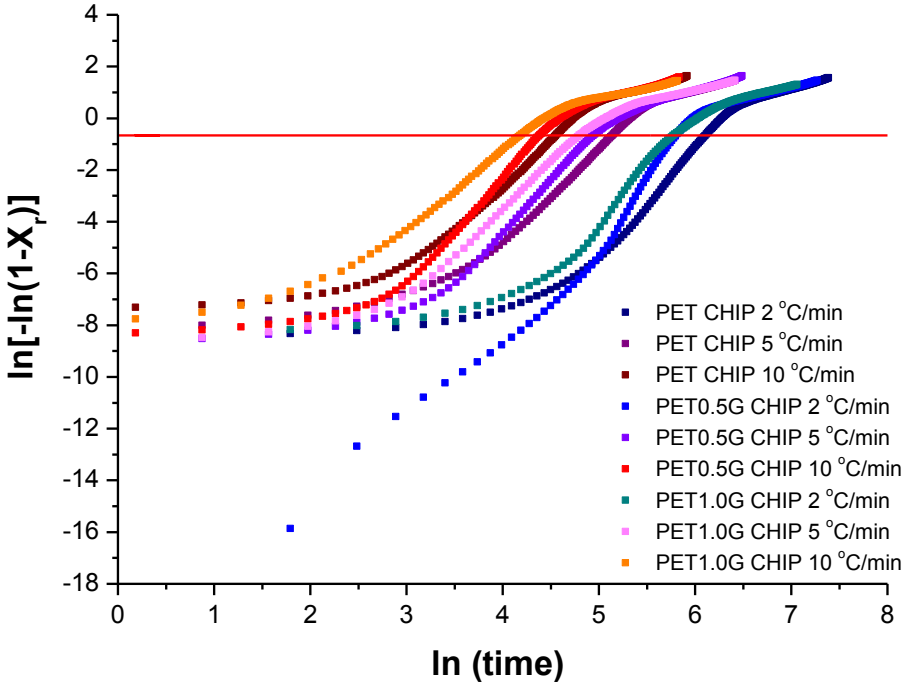

Figure 80 Modified Avrami plots relating to the dynamic crystallisation of PET, PET0.5G and PET1.0G uniaxial film. The red line represents a crystallinity of 40% and the limits of the Avrami model.

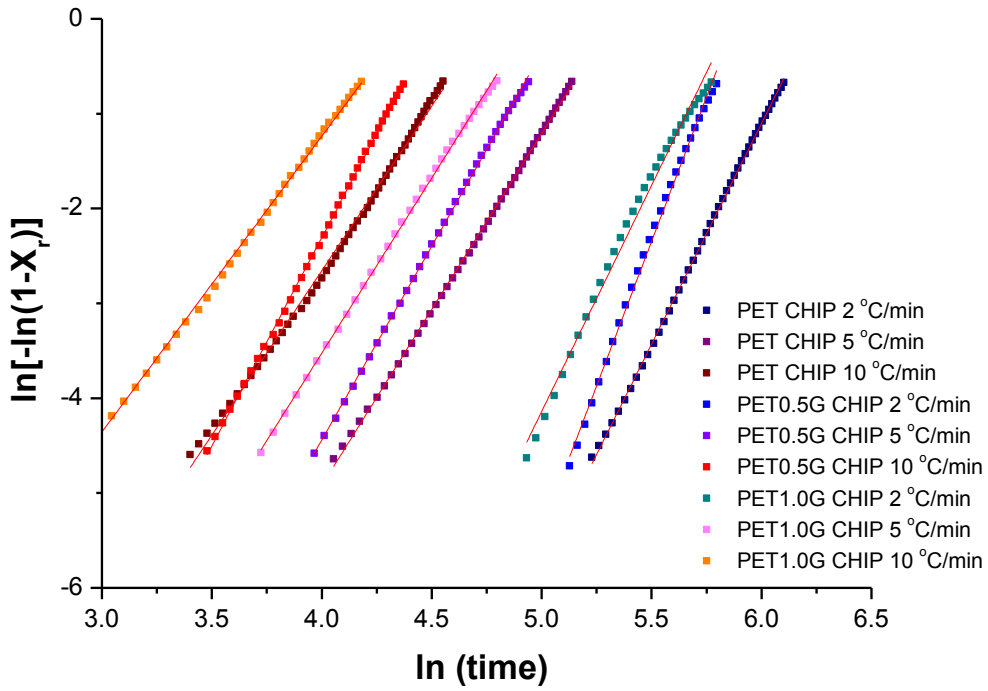

Figure 81 Replicate. Modified Avrami plots relating to the dynamic crystallisation of PET, PET0.5G and PET1.0G uniaxial film at crystallinities of between 1% and 40%.

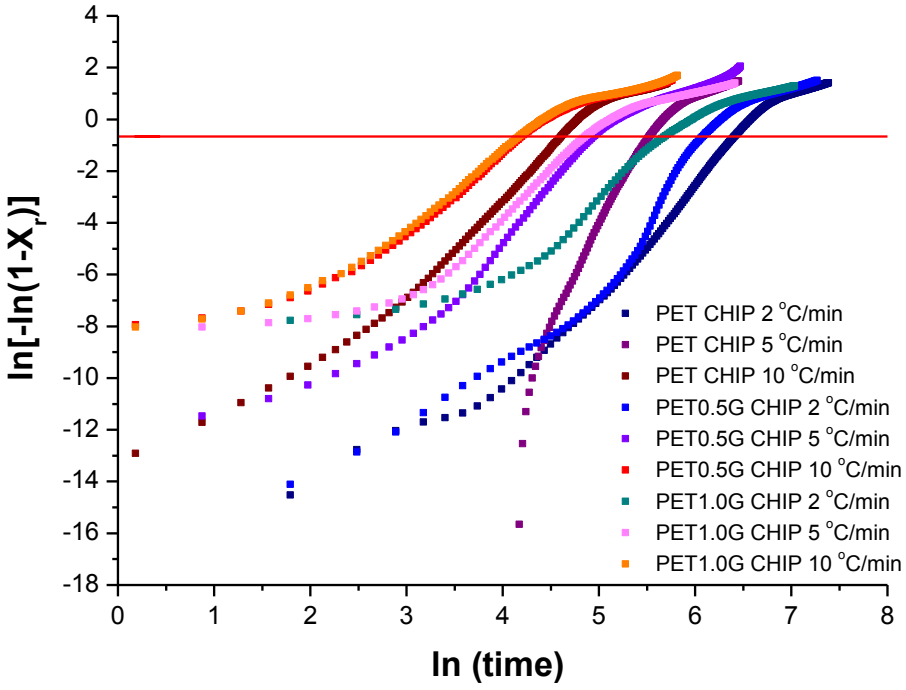

Figure 82 Replicate. Modified Avrami plots relating to the dynamic crystallisation of PET, PET0.5G and PET1.0G uniaxial film. The red line represents a crystallinity of 40% and the limits of the Avrami model.

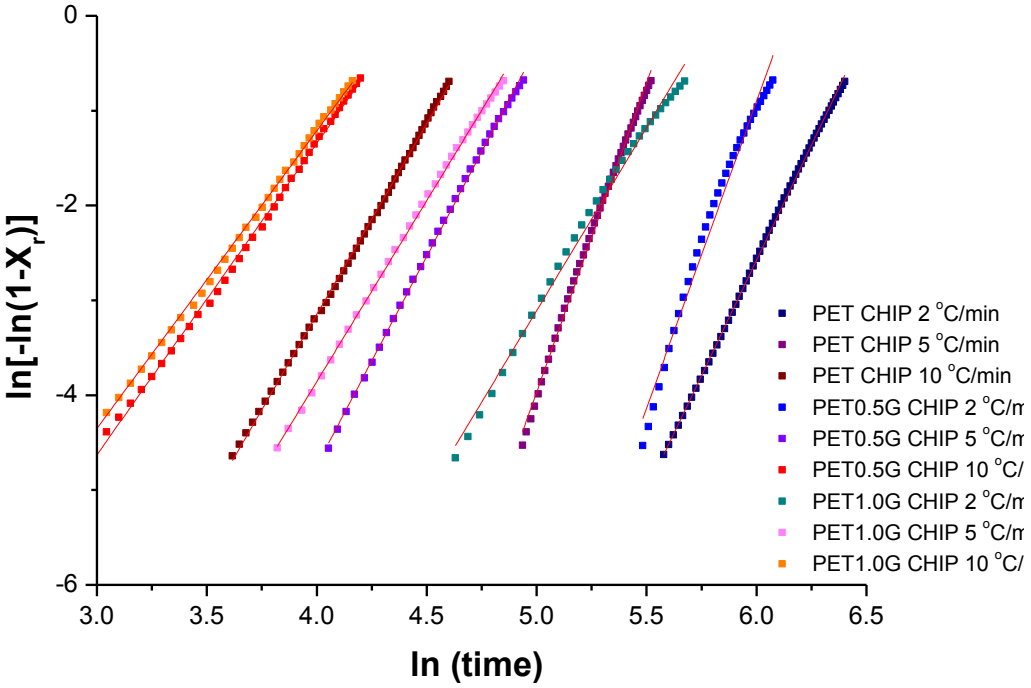

Figure 83 Replicate. Modified Avrami plots relating to the dynamic crystallisation of PET, PET0.5G and PET1.0G uniaxial film at crystallinities of between 1% and 40%.

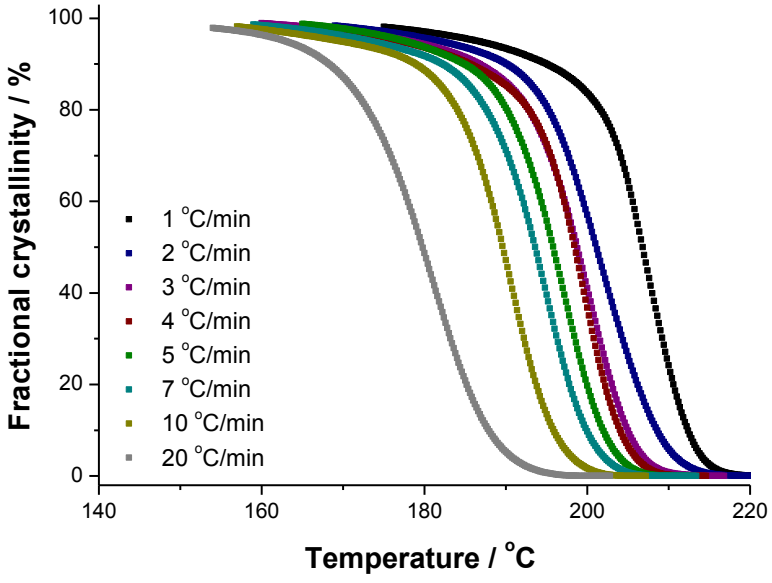

Figure 84 Fractional crystallinity during the dynamic crystallisation of PET uniaxial film at various cooling rates.

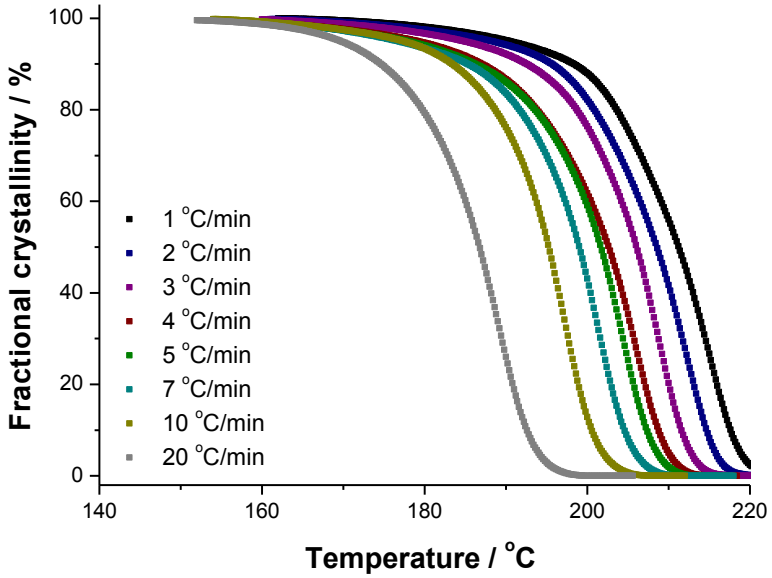

Figure 85 Fractional crystallinity during the dynamic crystallisation of PET0.5G uniaxial film at various cooling rates.

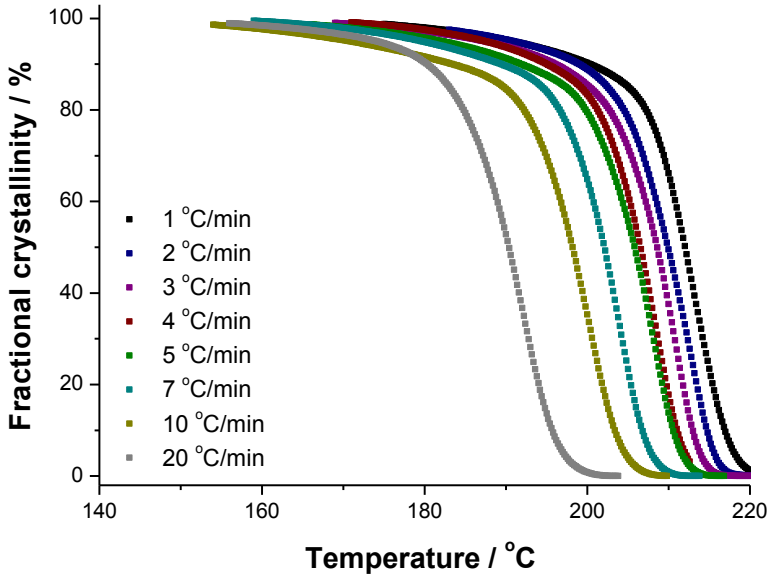

Figure 86 Fractional crystallinity during the dynamic crystallisation of PET1.0G uniaxial film at various cooling rates.

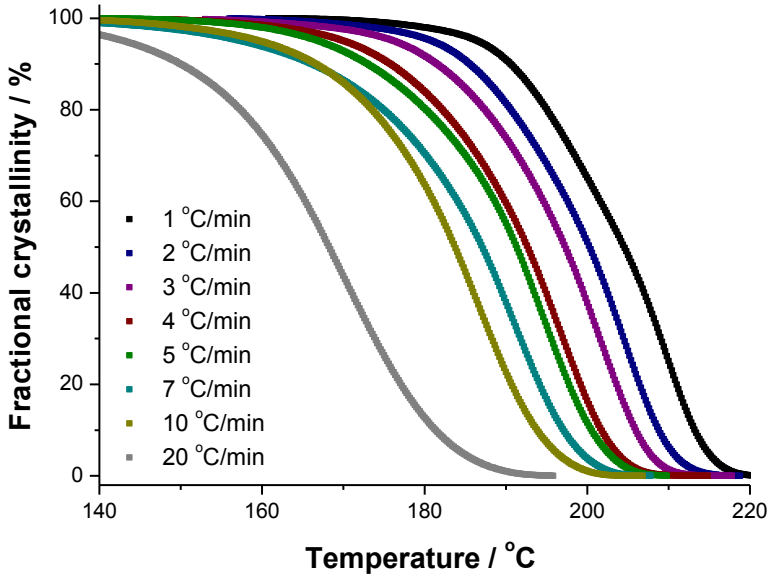

Figure 87 Replicate. Fractional crystallinity during the dynamic crystallisation of PET chip at various cooling rates.

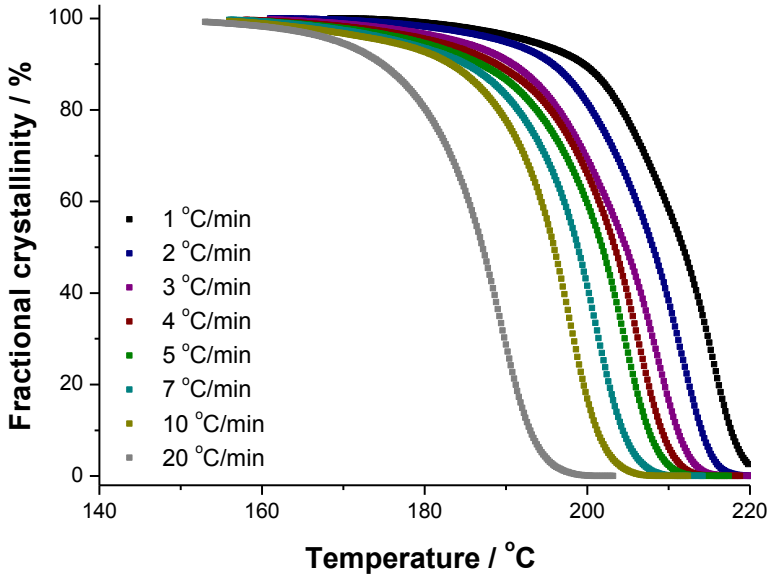

Figure 88 Replicate. Fractional crystallinity during the dynamic crystallisation of PET0.5G chip at various cooling rates.

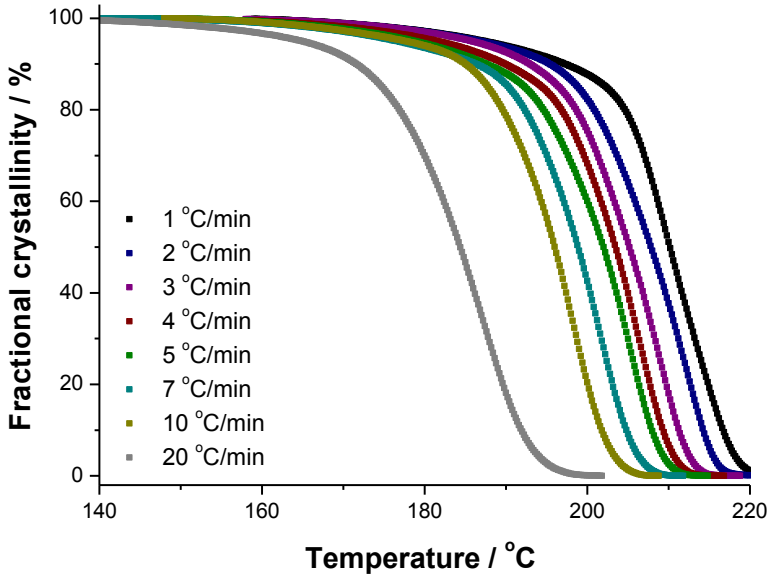

Figure 89 Replicate. Fractional crystallinity during the dynamic crystallisation of PET1.0G chip at various cooling rates.

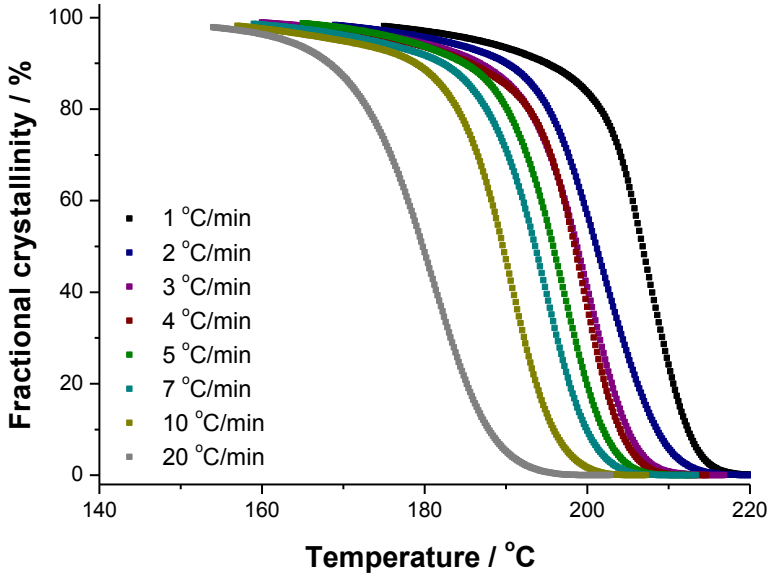

Figure 90 Replicate. Fractional crystallinity during the dynamic crystallisation of PET uniaxial film at various cooling rates.

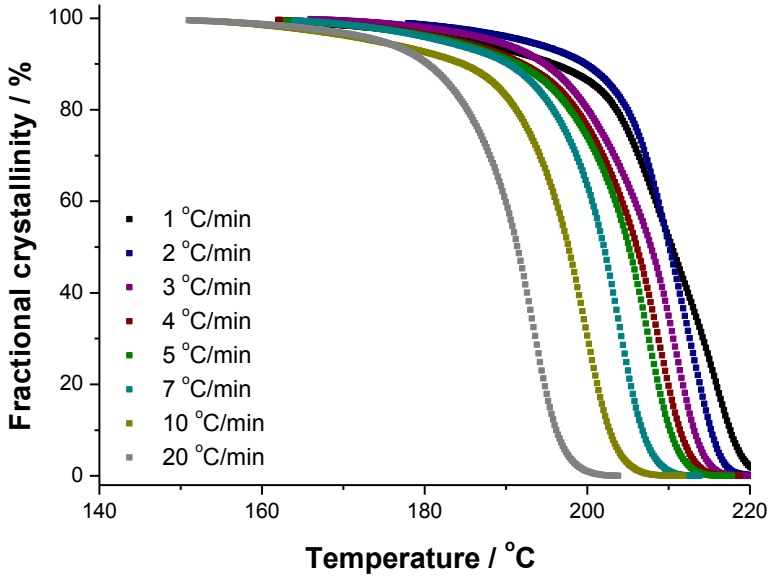

Figure 91 Replicate. Fractional crystallinity during the dynamic crystallisation of PET0.5G uniaxial film at various cooling rates.

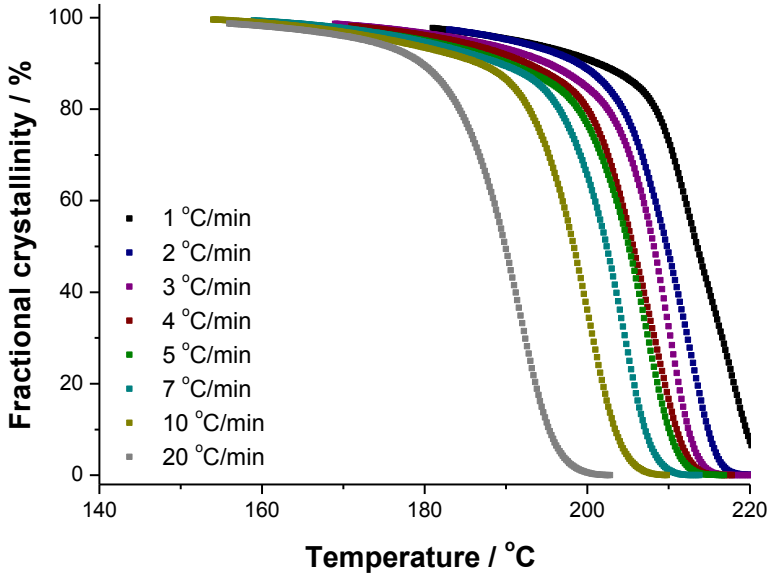

Figure 92 Replicate. Fractional crystallinity during the dynamic crystallisation of PET1.0G uniaxial film at various cooling rates.

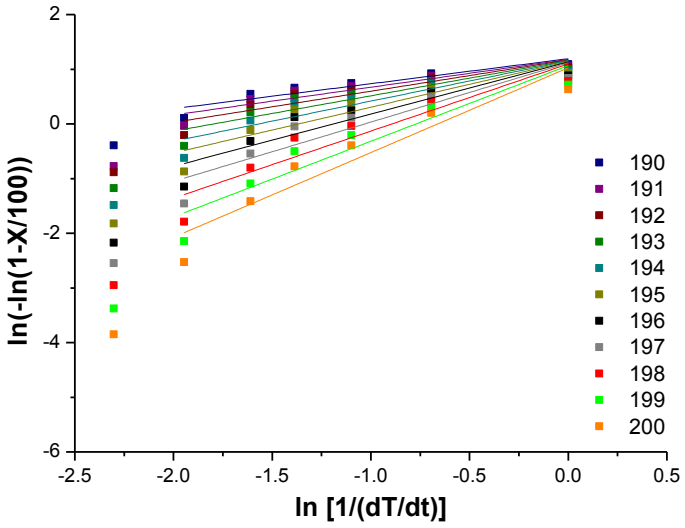

Figure 93 Ozawa plot of PET uniaxial film at temperatures between 200 ºC and 190 ºC.

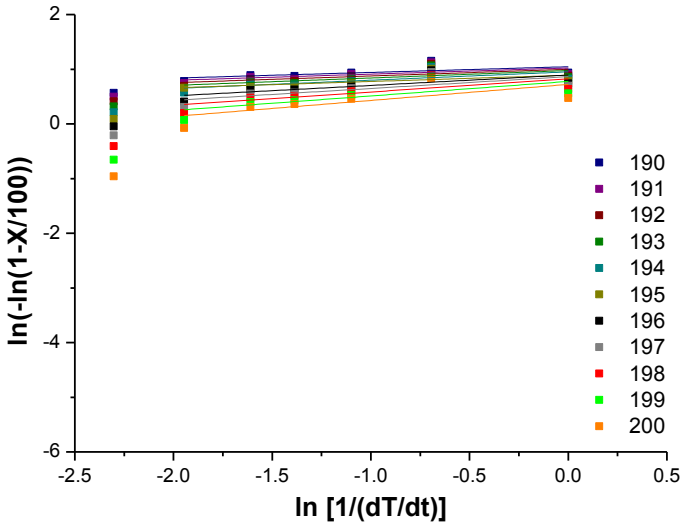

Figure 94 Ozawa plot of PET0.5G uniaxial film at temperatures between 200 ºC and 190 ºC.

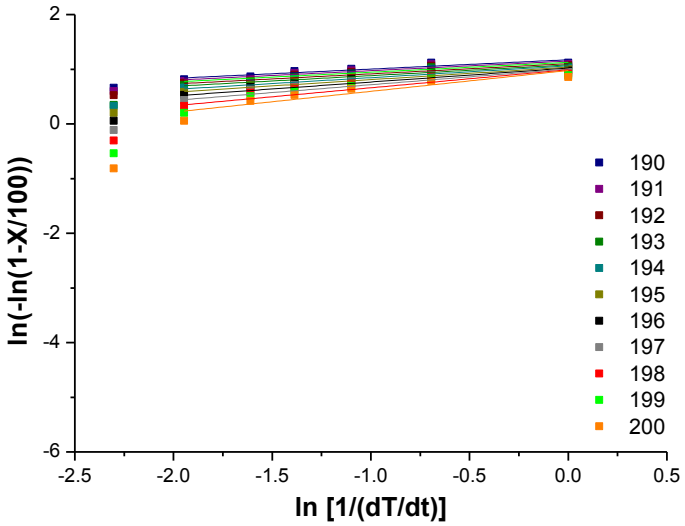

Figure 95 Ozawa plot of PET1.0G uniaxial film at temperatures between 200 ºC and 190 ºC.

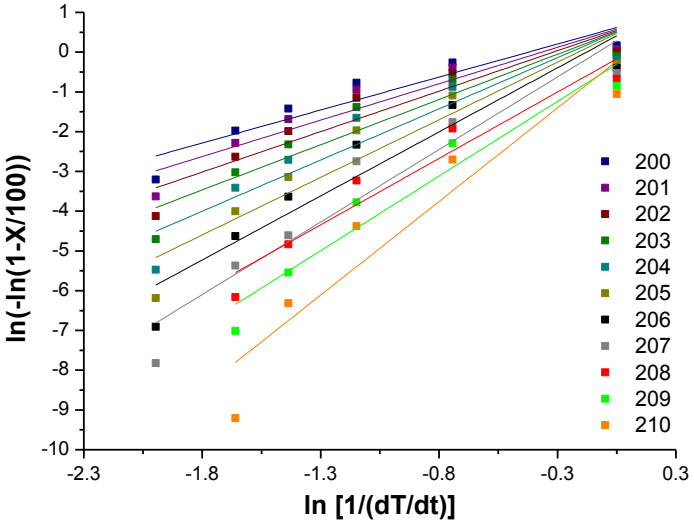

Figure 96 Ozawa plot of PET chip at temperatures between 200 ºC and 190 ºC.

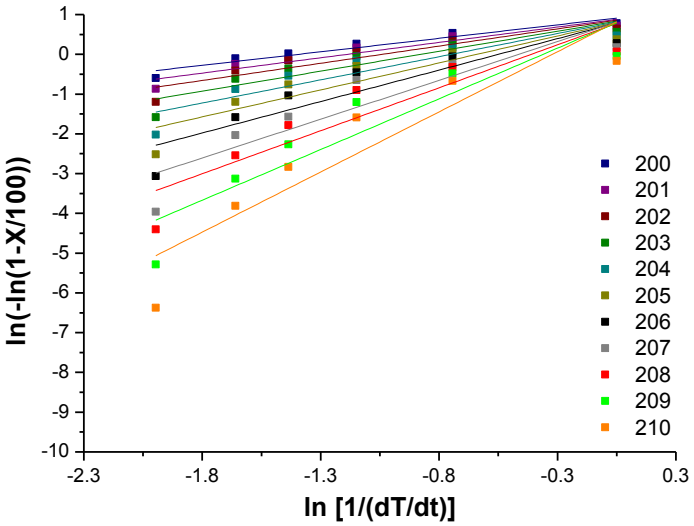

Figure 97 Ozawa plot of PET0.5G chip at temperatures between 200 ºC and 190 ºC.

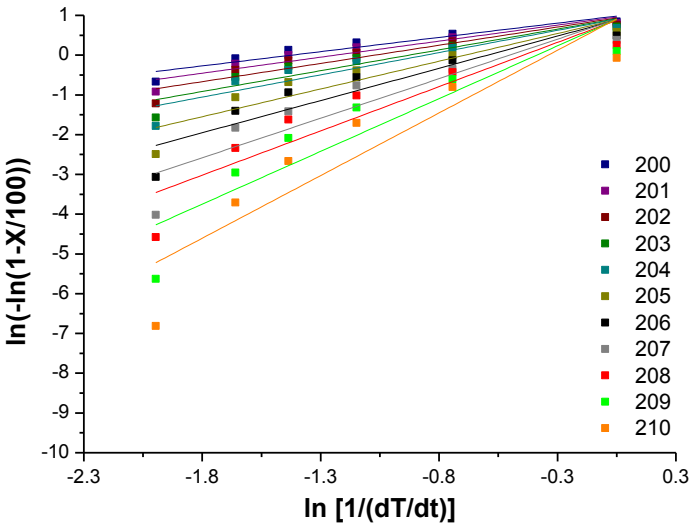

Figure 98 Ozawa plot of PET1.0G chip at temperatures between 200 ºC and 190 ºC.

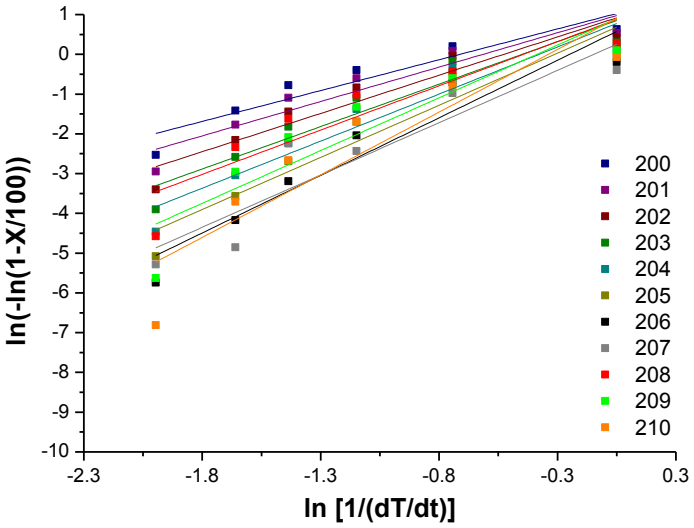

Figure 99 Ozawa plot of PET uniaxial film at temperatures between 200 ºC and 190 ºC.

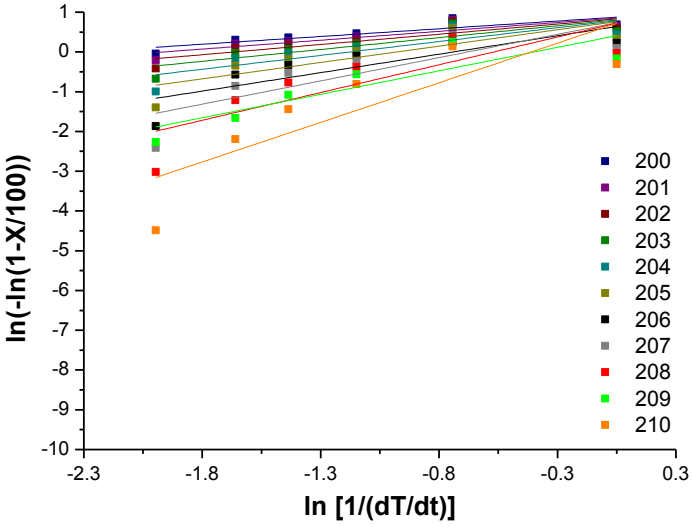

Figure 100 Ozawa plot of PET0.5G uniaxial film at temperatures between 200 ºC and 190 ºC.

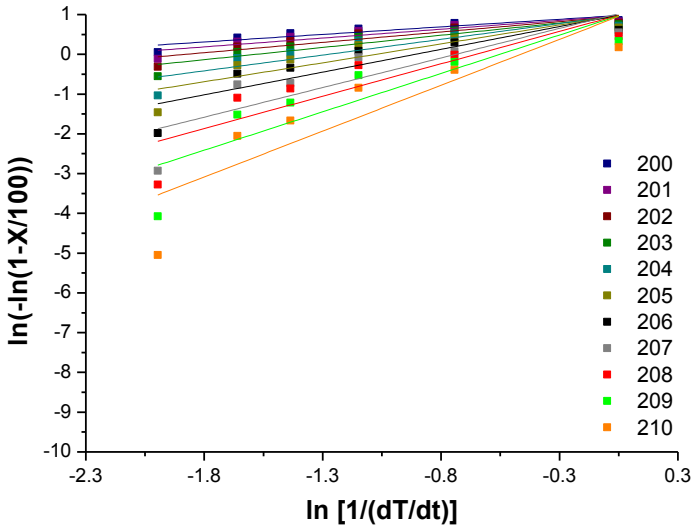

Figure 101 Ozawa plot of PET1.0G uniaxial film at temperatures between 200 ºC and 190 ºC.

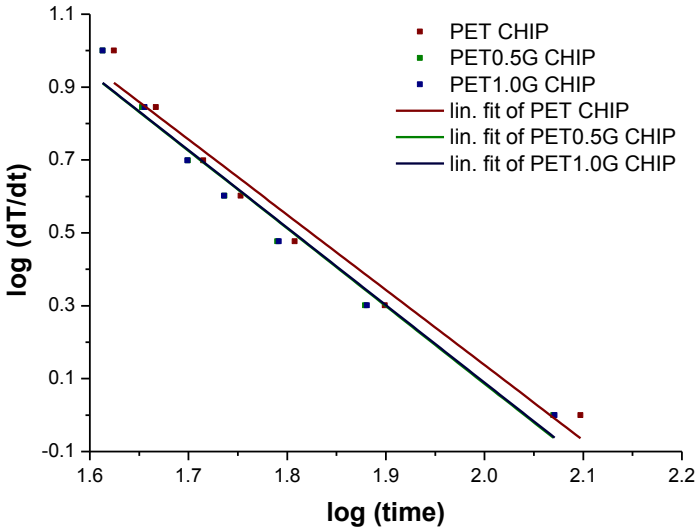

Figure 102 Combined Avrami-Ozawa plots for PET, PET0.5G and PET1.0G chip at 40% crystallinity.

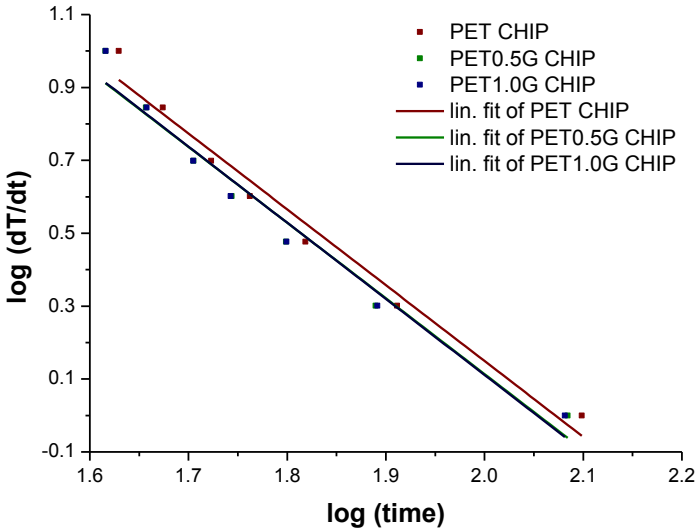

Figure 103 Combined Avrami-Ozawa plots for PET, PET0.5G and PET1.0G chip at 60% crystallinity.

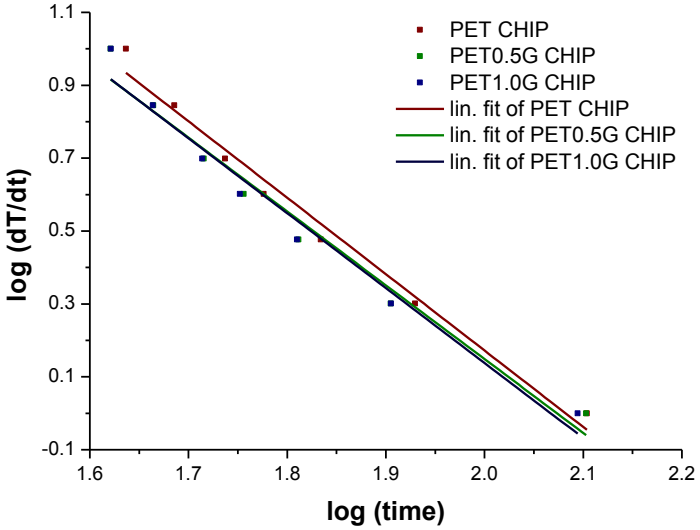

Figure 104 Combined Avrami-Ozawa plots for PET, PET0.5G and PET1.0G chip at 80% crystallinity.

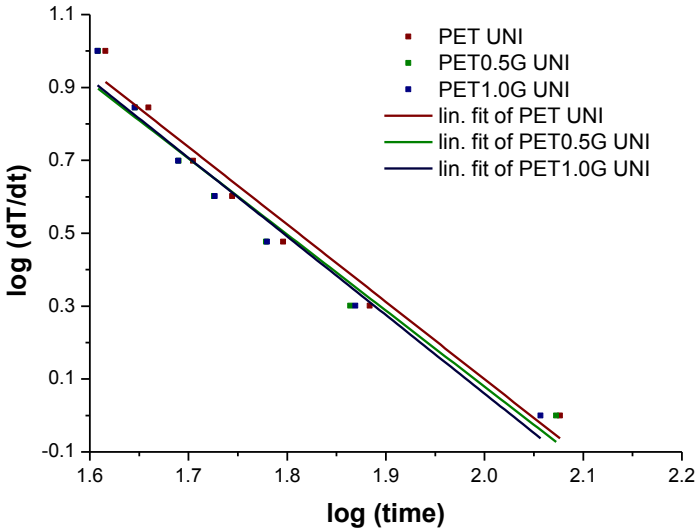

Figure 105 Combined Avrami-Ozawa plots for PET, PET0.5G and PET1.0G uniaxial film at 20% crystallinity.

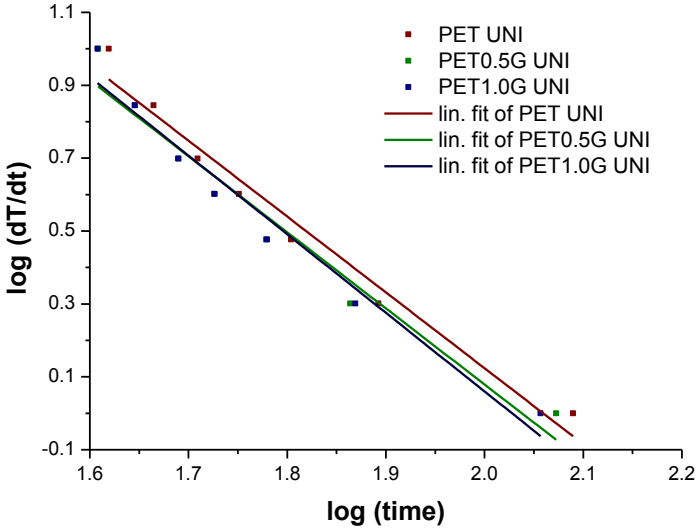

Figure 106 Combined Avrami-Ozawa plots for PET, PET0.5G and PET1.0G uniaxial film at 40% crystallinity.

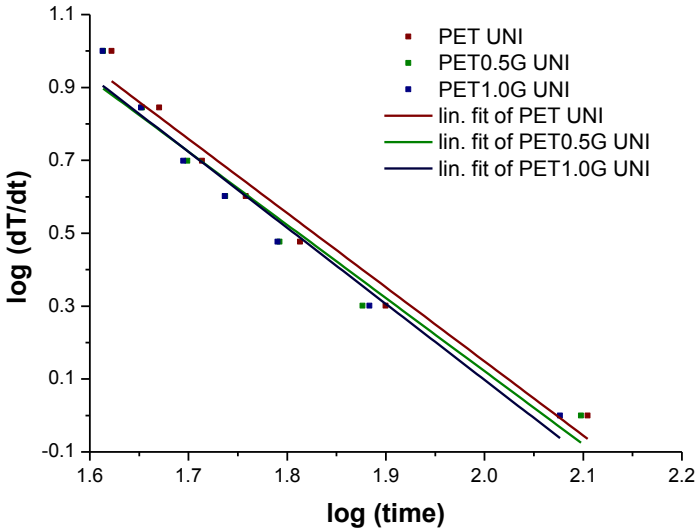

Figure 107 Combined Avrami-Ozawa plots for PET, PET0.5G and PET1.0G uniaxial film at 60% crystallinity.

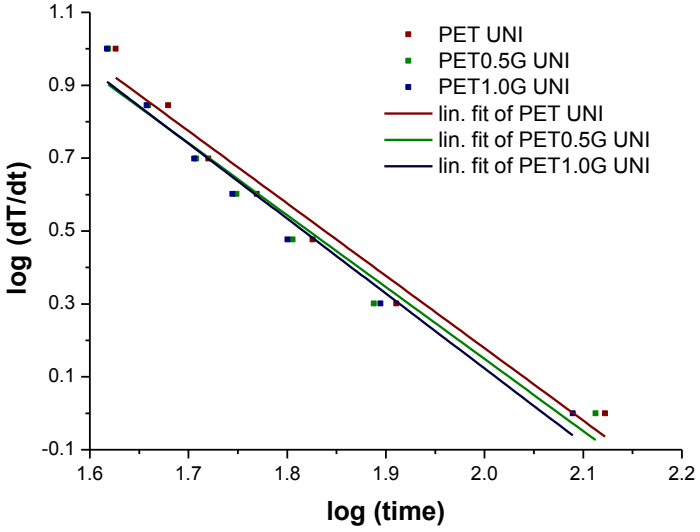

Figure 108 Combined Avrami-Ozawa plots for PET, PET0.5G and PET1.0G uniaxial film at 80% crystallinity.

APPENDIX 5: THERMAL DEGRADATION (DSC/TGA)

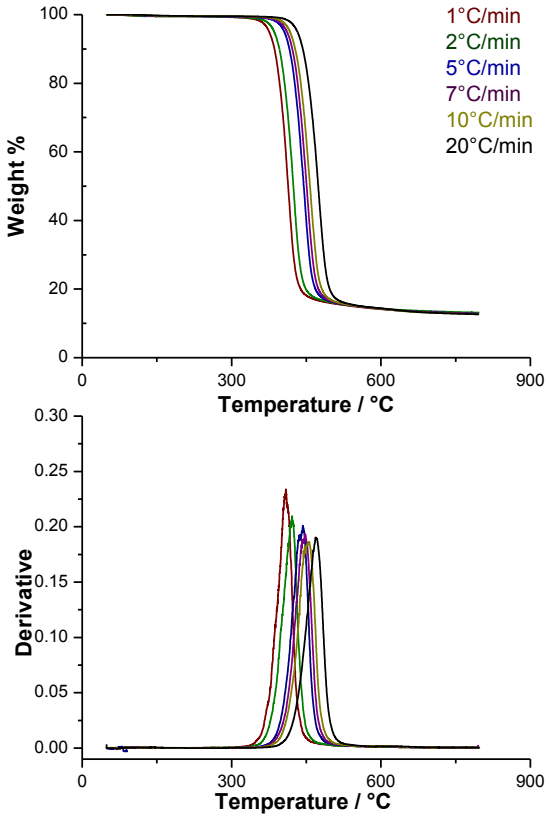

Figure 109 TGA thermograms for PET0.5G uniaxial film during thermal degradation under helium.

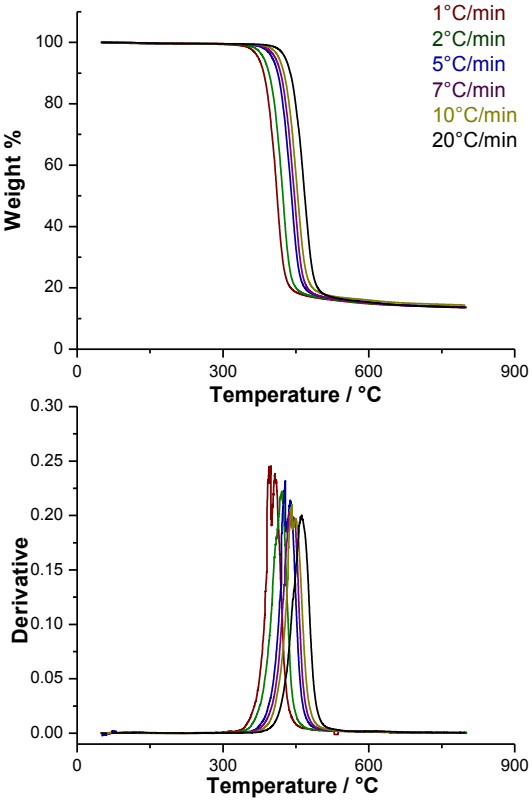

Figure 110 TGA thermograms for PET1.0G uniaxial film during thermal degradation under helium.

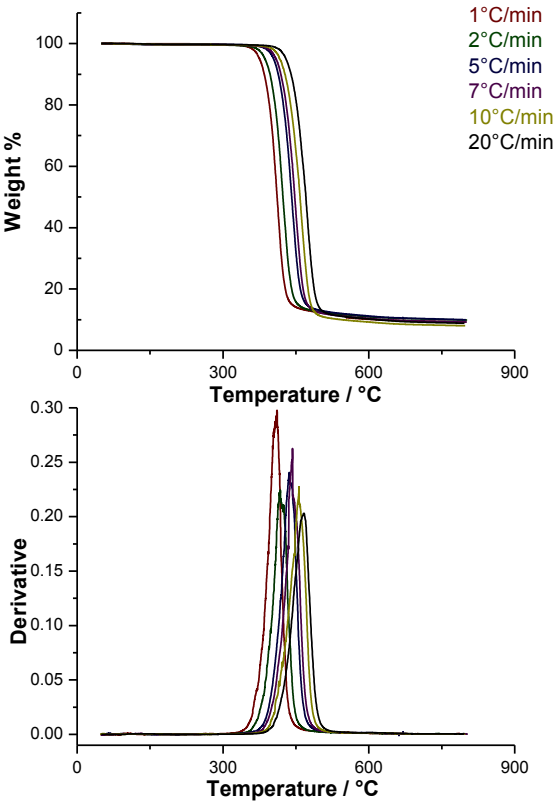

Figure 111 Replicate. TGA thermograms for PET uniaxial film during thermal degradation under helium.

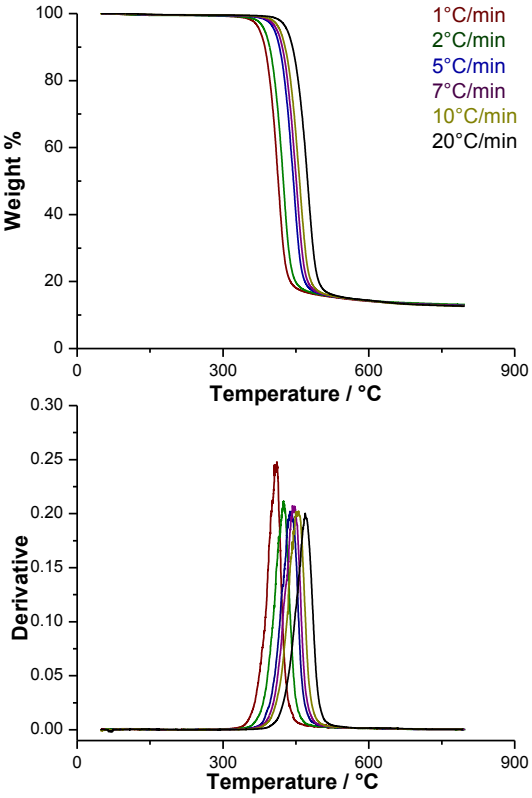

Figure 112 Replicate. TGA thermograms for PET0.5G uniaxial film during thermal degradation under helium.

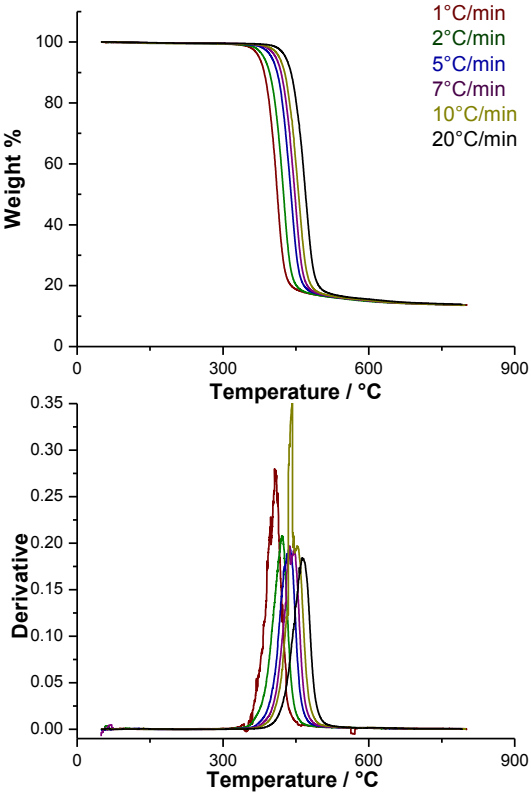

Figure 113 Replicate. TGA thermograms for PET1.0G uniaxial film during thermal degradation under helium.

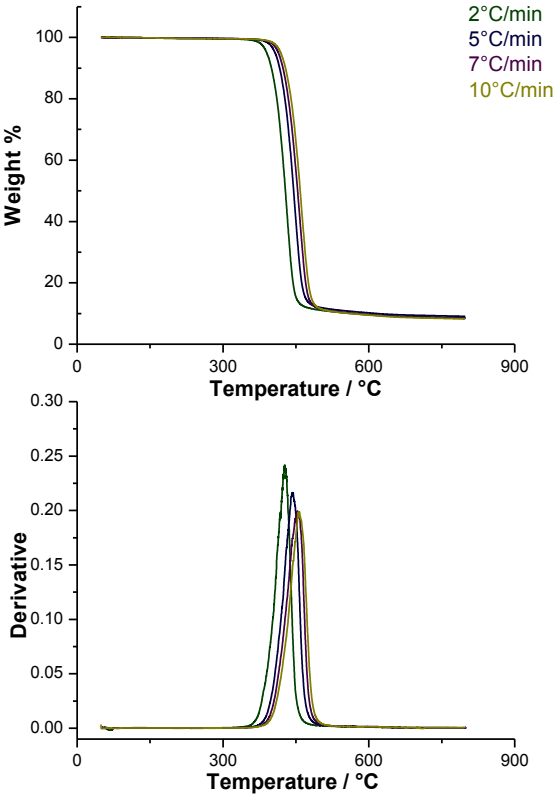

Figure 114 TGA thermograms for PET chip during thermal degradation under helium.

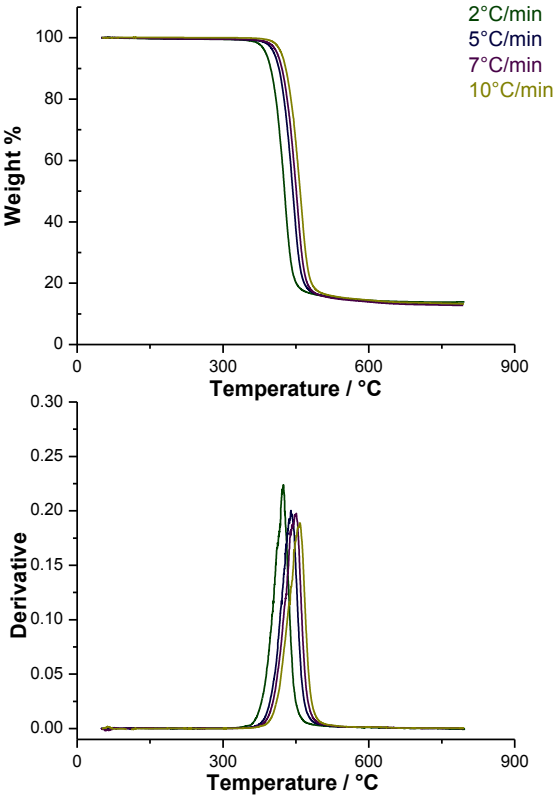

Figure 115 TGA thermograms for PET0.5G chip during thermal degradation under helium.

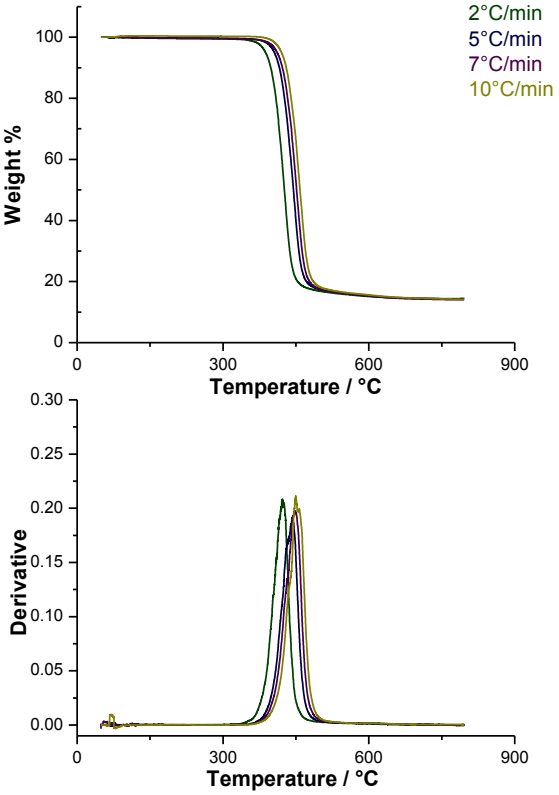

Figure 116 TGA thermograms for PET1.0G chip during thermal degradation under helium.

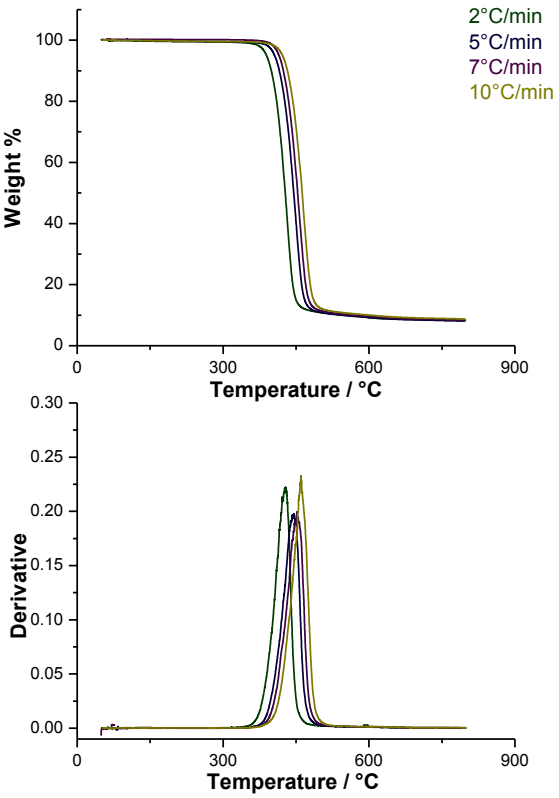

Figure 117 Replicate. TGA thermograms for PET chip during thermal degradation under helium.

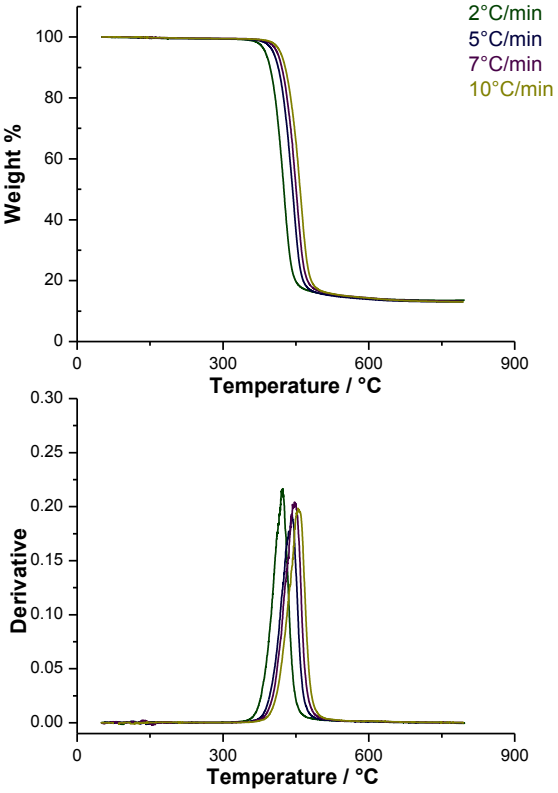

Figure 118 Replicate. TGA thermograms for PET0.5G chip during thermal degradation under helium.

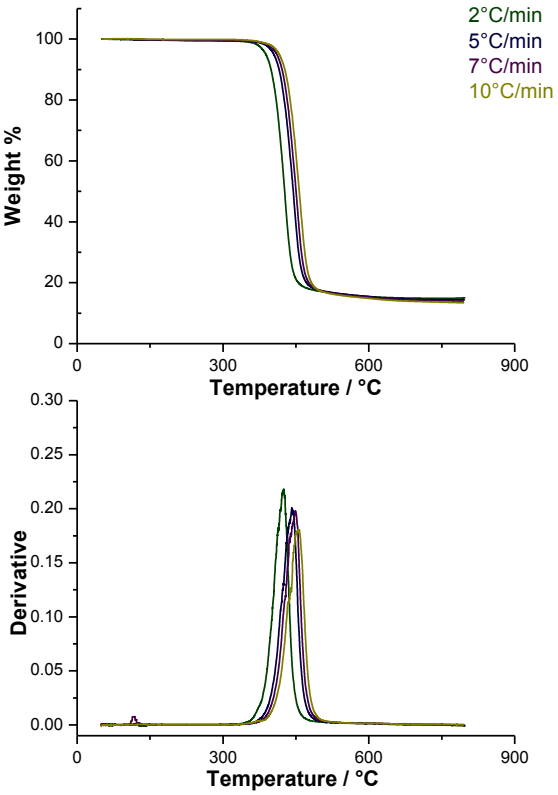

Figure 119 Replicate. TGA thermograms for PET1.0G chip during thermal degradation under helium.

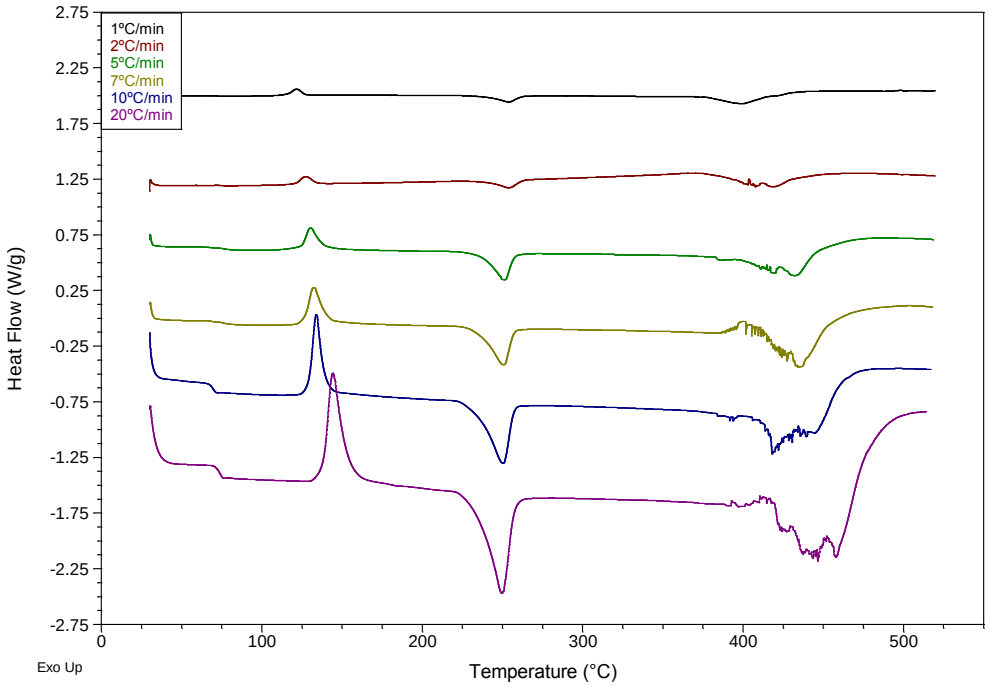

Figure 120 Replicate. Dynamic thermal degradation profiles of PET at various heating rates under nitrogen.

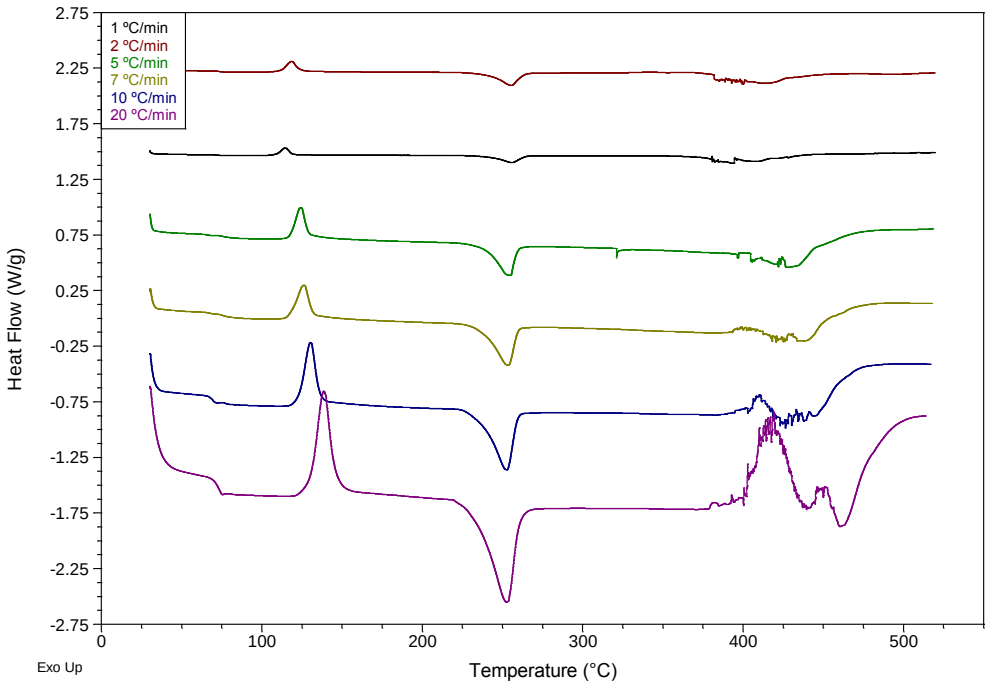

Figure 121 Replicate. Dynamic thermal degradation profiles of PET0.5G at various heating rates under nitrogen.

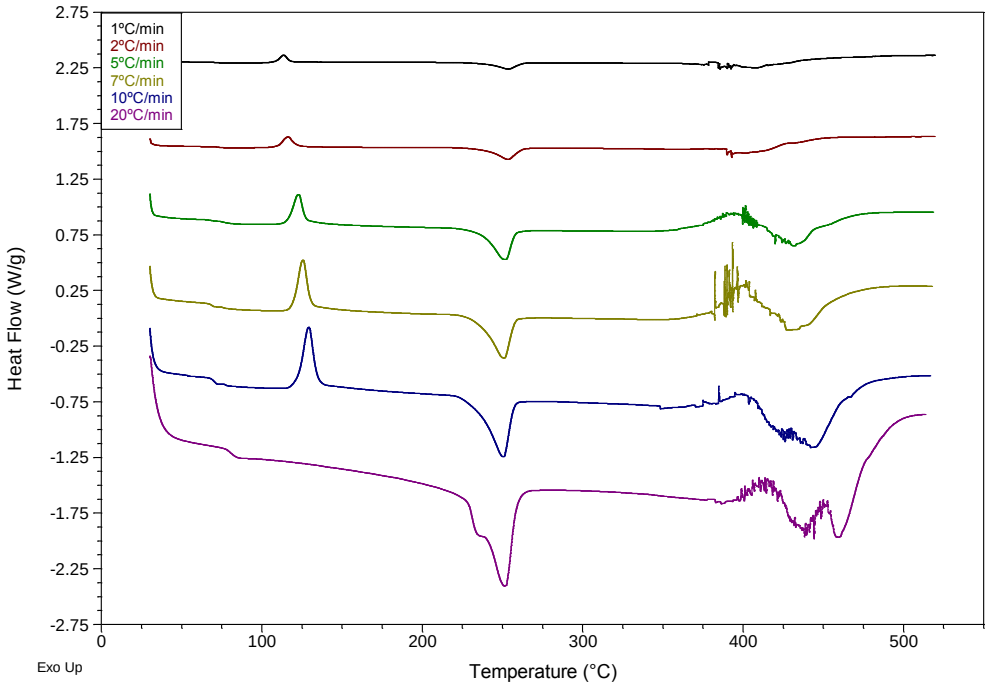

Figure 122 Replicate. Dynamic thermal degradation profiles of PET1.0G at various heating rates under nitrogen.

APPENDIX 6: THERMAL DEGRADATION (TVA)

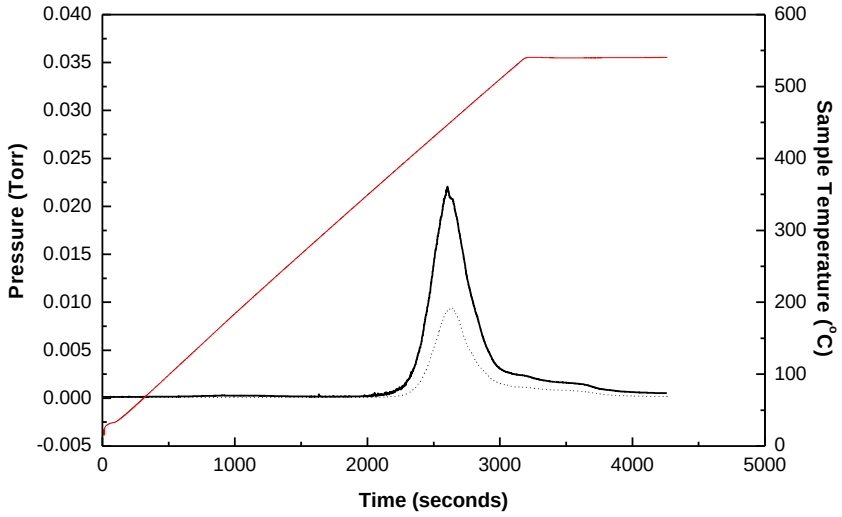

Figure 123 Pressure measurements from the pre- and post-sub-ambient trap during thermal degradation of PET chip. The solid and dashed plots represent pressure measurements pre- and post- sub-ambient trap, respectfully. The red plot represents the furnace temperature.

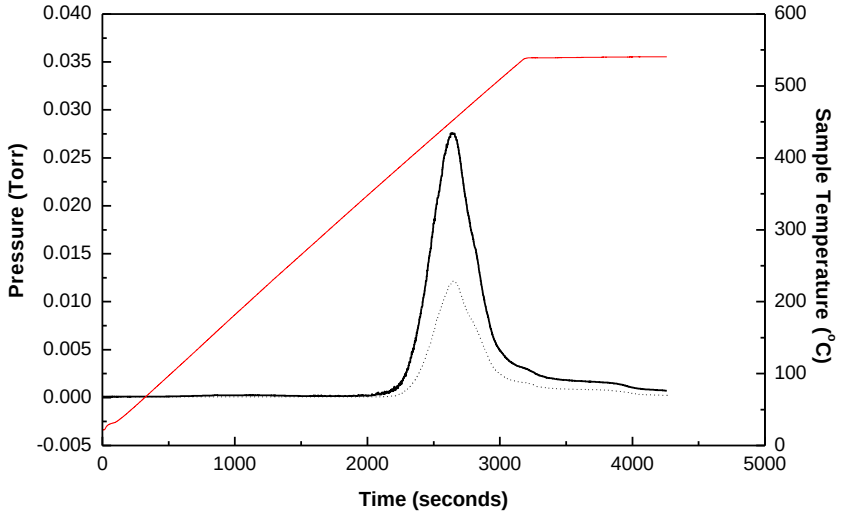

Figure 124 Pressure measurements from the pre- and post-sub-ambient trap during thermal degradation of PET0.5G chIp. The solid and dashed plots represent pressure measurements pre- and post- sub-ambient trap, respectfully. The red plot represents the furnace temperature.

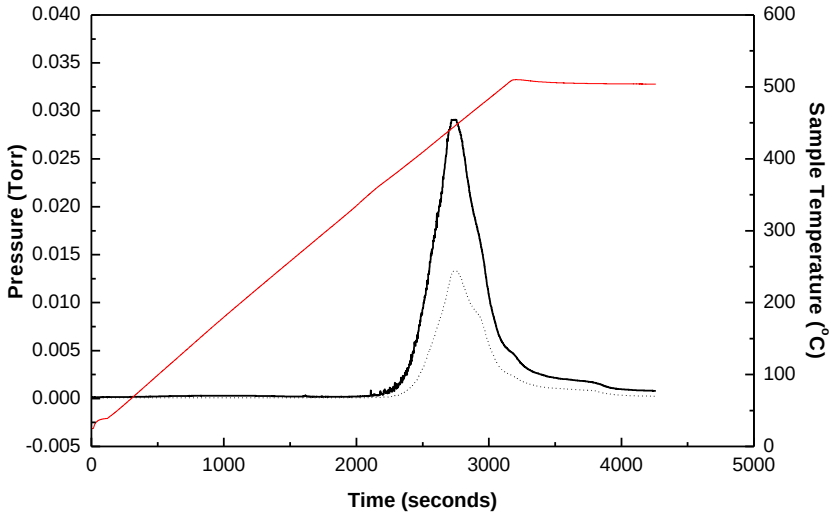

Figure 125 Pressure measurements from the pre- and post-sub-ambient trap during thermal degradation of PET1.0G chIp. The solid and dashed plots represent pressure measurements pre- and post- sub-ambient trap, respectfully. The red plot represents the furnace temperature.

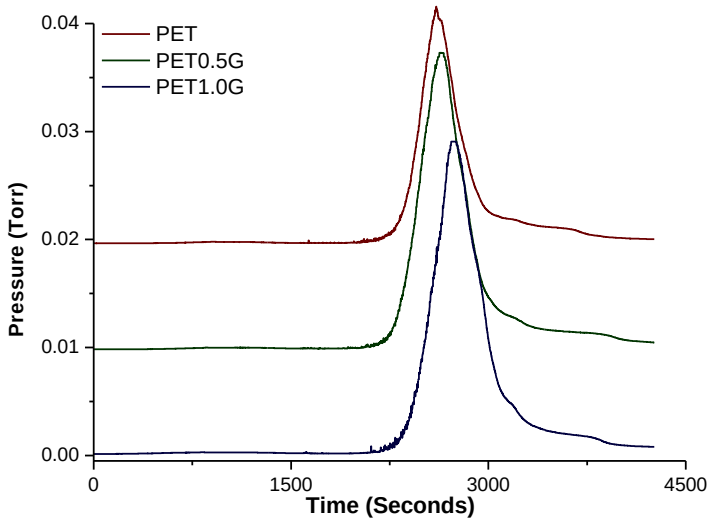

Figures 126 Pressure readings of pre-subambient traps during the thermal degradation of PET, PET0.5G and PET1.0G chip.

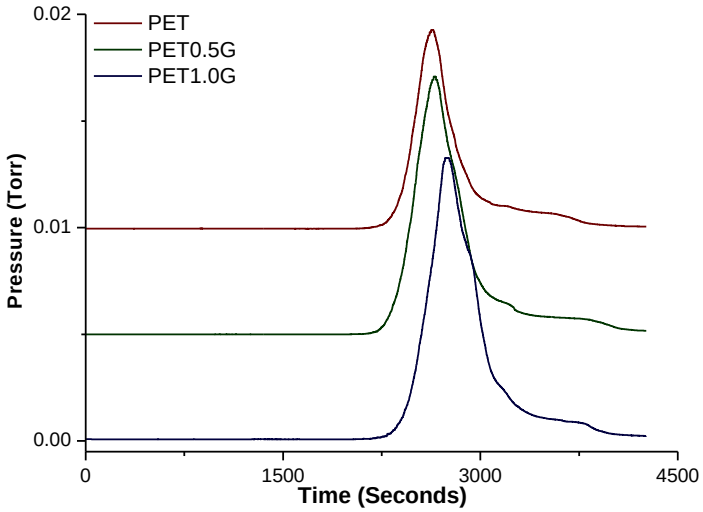

Figures 127 Pressure readings of posy-subambient traps during the thermal degradation of PET, PET0.5G and PET1.0G chip.

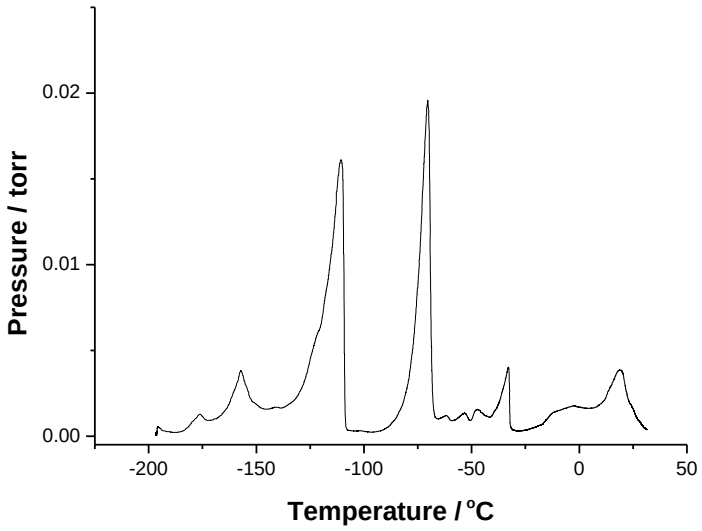

Figure 128 Pressure measurements during the subambient TVA run of PET chip. The subambient run is performed under a 4ºC min^{-1} heating rate from -196 ºC to +40 ºC.

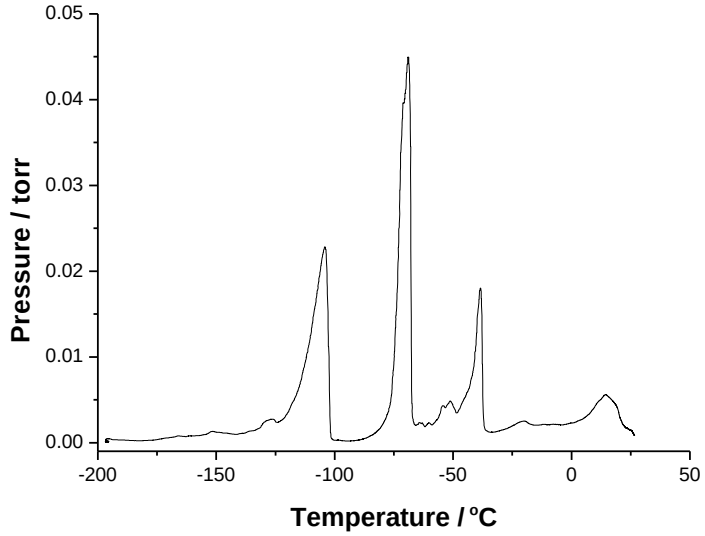

Figure 129 Pressure measurements during the subambient TVA run of PET0.5G chip. The subambient run is performed under a 4ºC min^{-1} heating rate from -196 ºC to +40 ºC.

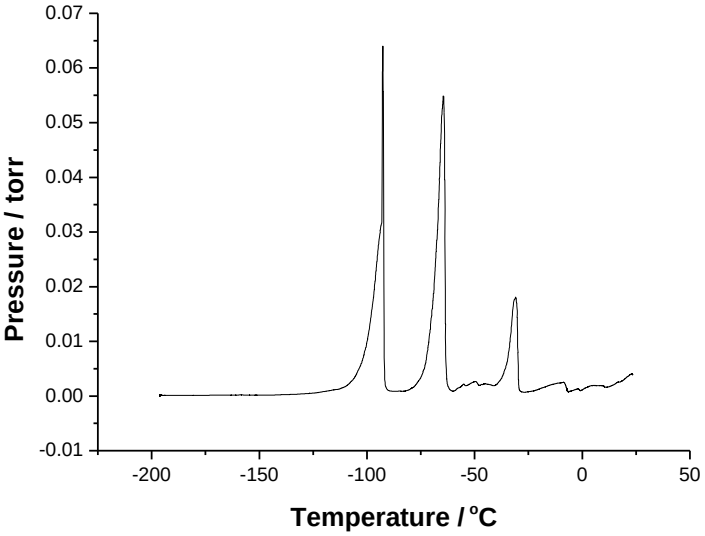

Figure 130 Pressure measurements during the subambient TVA run of PET1.0G chip. The subambient run is performed under a 4ºC min^{-1} heating rate from -196 ºC to +40 ºC.

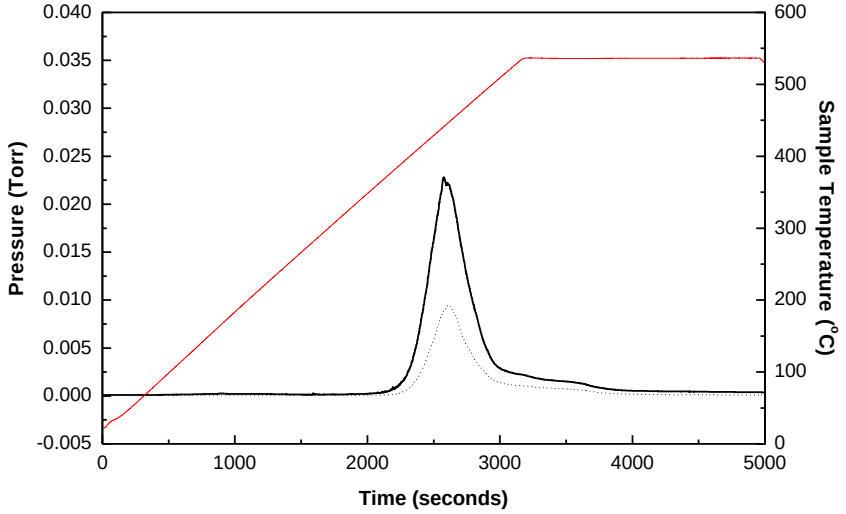

Figure 131 Replicate. Pressure measurements from the pre- and post-sub-ambient trap during thermal degradation of PET chip. The solid and dashed plots represent pressure measurements pre- and post- sub-ambient trap, respectfully. The red plot represents the furnace temperature.

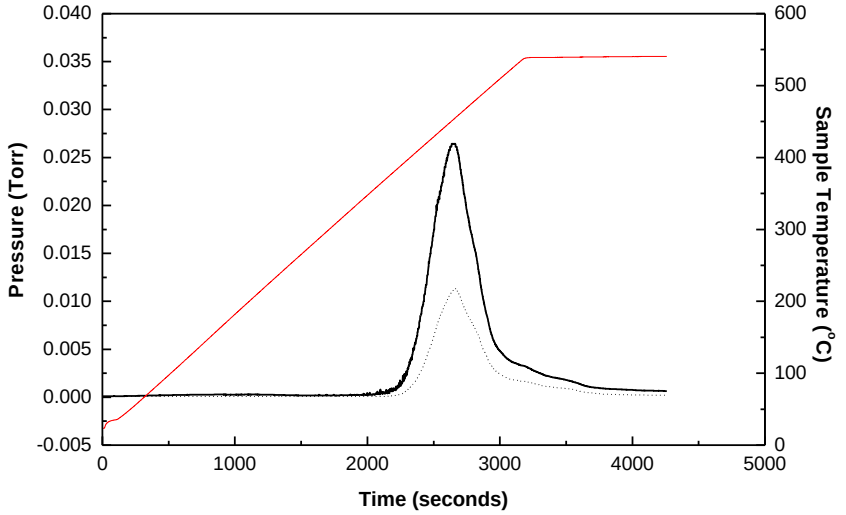

Figure 132 Replicate. Pressure measurements from the pre- and post-sub-ambient trap during thermal degradation of PET0.5G chip. The solid and dashed plots represent pressure measurements pre- and post- sub-ambient trap, respectfully. The red plot represents the furnace temperature.

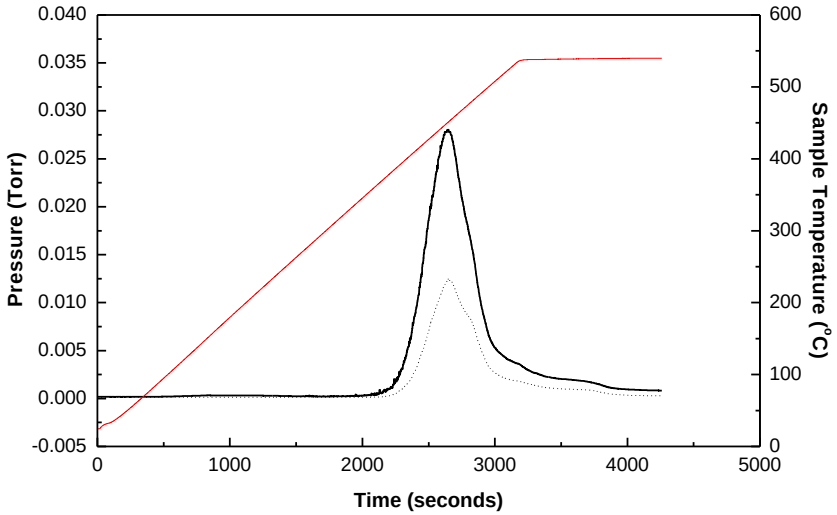

Figure 133 Replicate. Pressure measurements from the pre- and post-sub-ambient trap during thermal degradation of PET1.0G chip. The solid and dashed plots represent pressure measurements pre- and post- sub-ambient trap, respectfully. The red plot represents the furnace temperature.

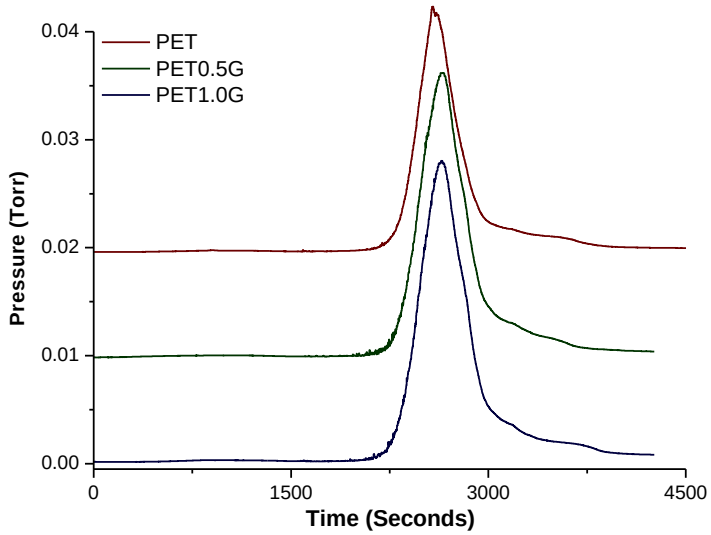

Figures 134 Replicate. Pressure readings of pre-subambient traps during the thermal degradation of PET, PET0.5G and PET1.0G chip.

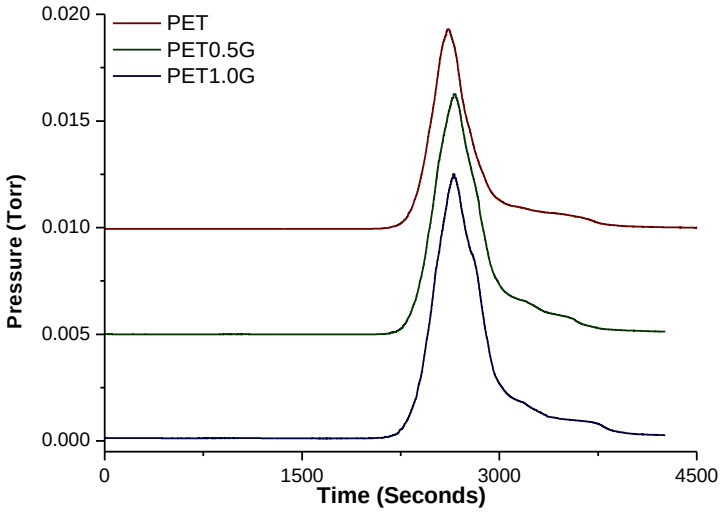

Figures 135 Replicate. Pressure readings of post-subambient traps during the thermal degradation of PET, PET0.5G and PET1.0G chip.

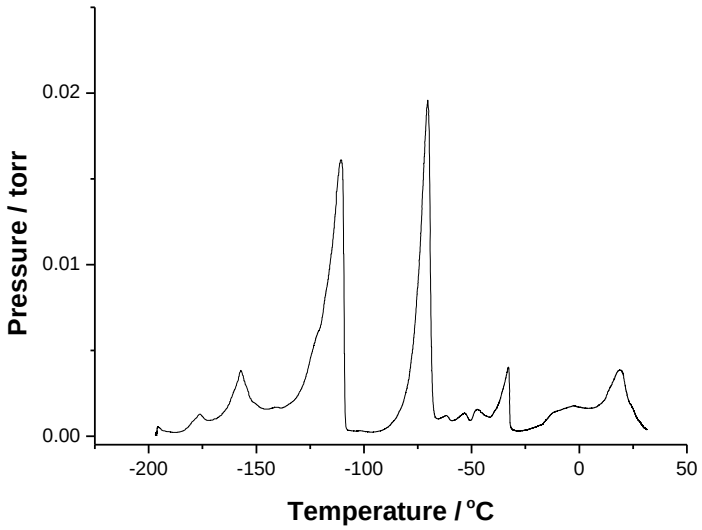

Figure 136 Replicate. Pressure measurements during the subambient TVA run of PET chip. The subambient run is performed under a 4ºC min^{-1} heating rate from -196 ºC to +40 ºC.

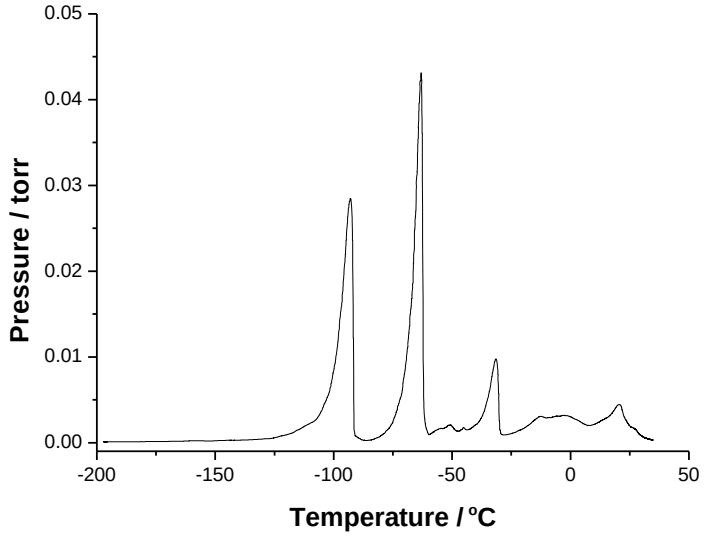

Figure 137 Replicate. Pressure measurements during the subambient TVA run of PET0.5G chip. The subambient run is performed under a 4ºC min^{-1} heating rate from -196 ºC to +40 ºC.

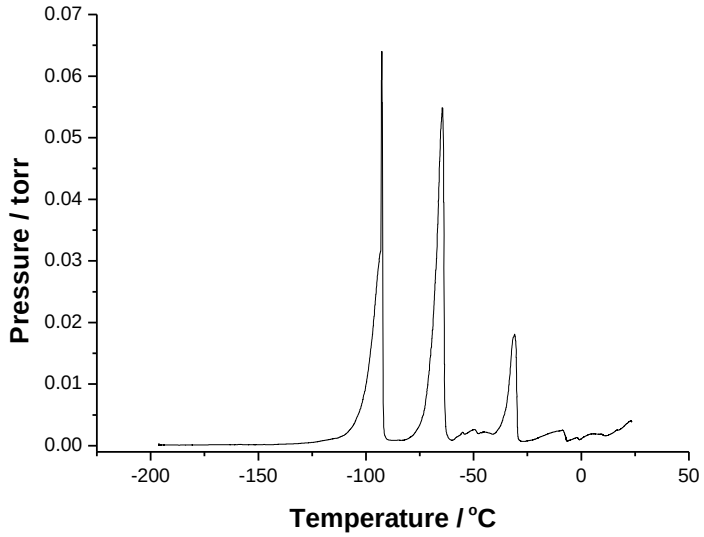

Figure 138 Replicate. Pressure measurements during the subambient TVA run of PET1.0 G chip. The subambient run is performed under a 4ºC min^{-1} heating rate from -196 ºC to +40 ºC.

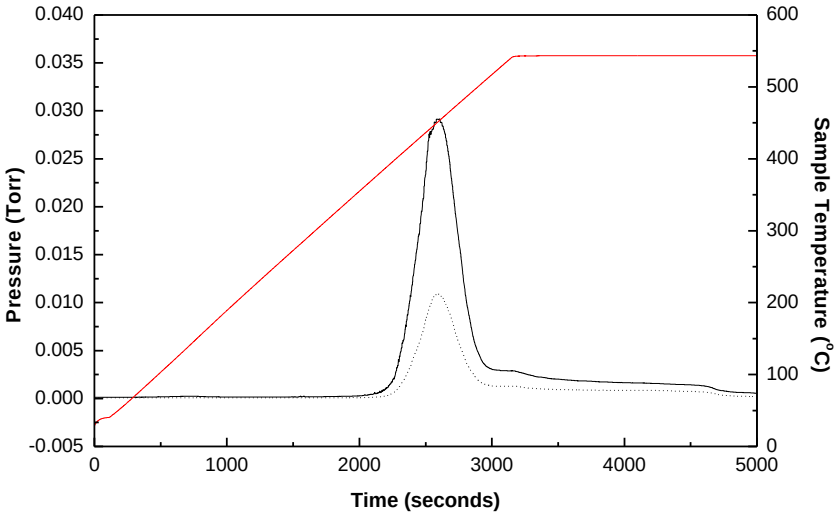

Figure 139 Pressure measurements from the pre- and post-sub-ambient trap during thermal degradation of PET uniaxial film. The solid and dashed plots represent pressure measurements pre- and post- sub-ambient trap, respectfully. The red plot represents the furnace temperature.

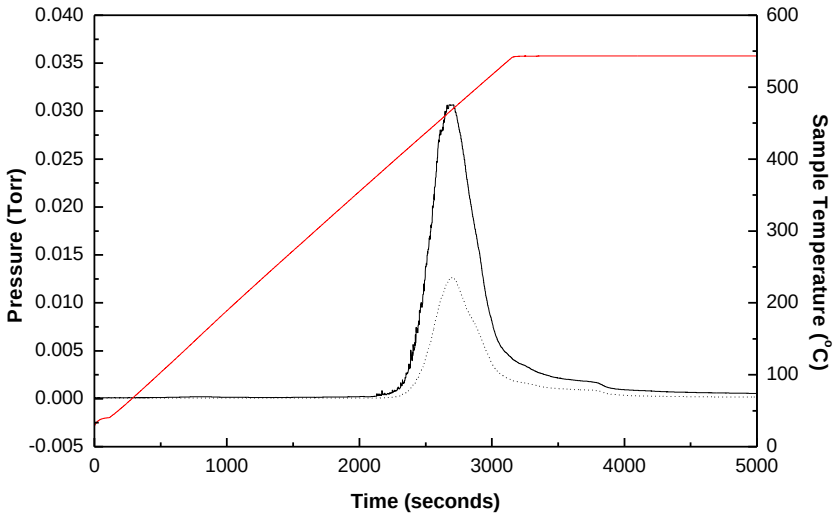

Figure 140 Pressure measurements from the pre- and post-sub-ambient trap during thermal degradation of PET0.5G uniaxial film. The solid and dashed plots represent pressure measurements pre- and post- sub-ambient trap, respectfully. The red plot represents the furnace temperature.

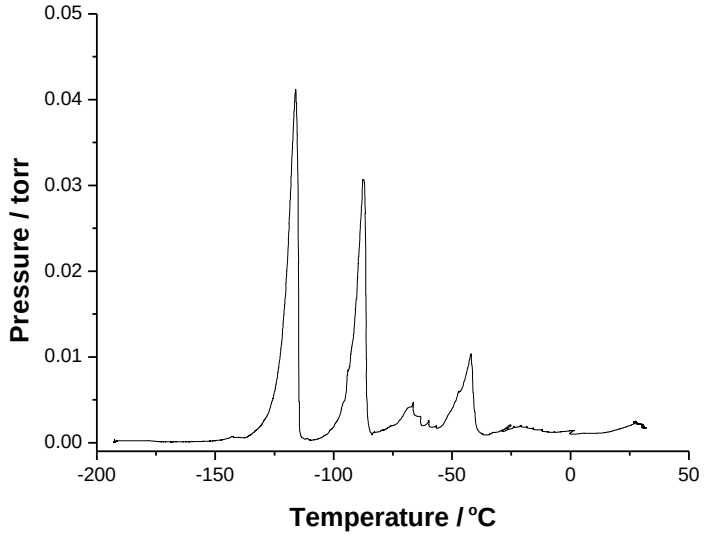

Figure 141 Pressure measurements during the subambient TVA run of PET uniaxial film. The subambient run is performed under a 4ºC min^{-1} heating rate from -196 ºC to +40 ºC.

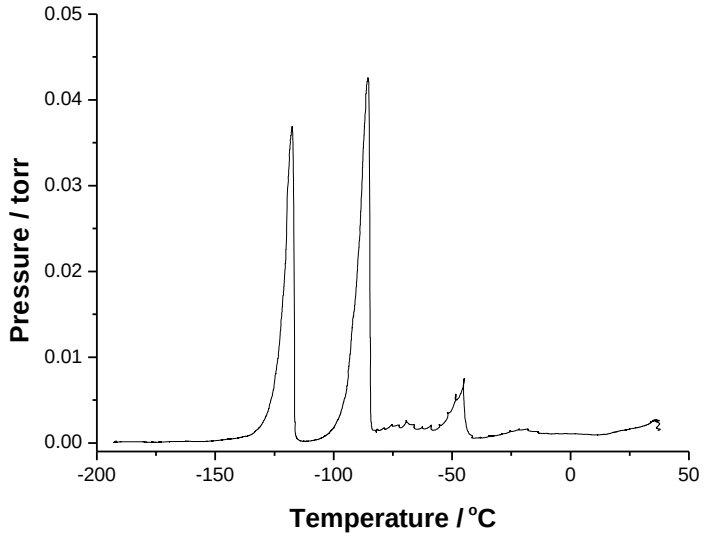

Figure 142 Pressure measurements during the subambient TVA run of PET0.5G uniaxial film. The subambient run is performed under a 4ºC min^{-1} heating rate from -196 ºC to +40 ºC.

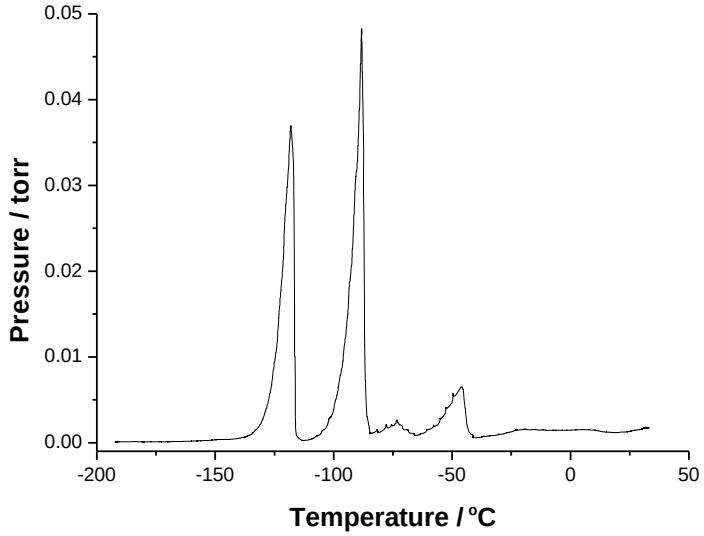

Figure 143 Pressure measurements during the subambient TVA run of PET1.0G uniaxial film. The subambient run is performed under a 4ºC min^{-1} heating rate from -196 ºC to +40 ºC.

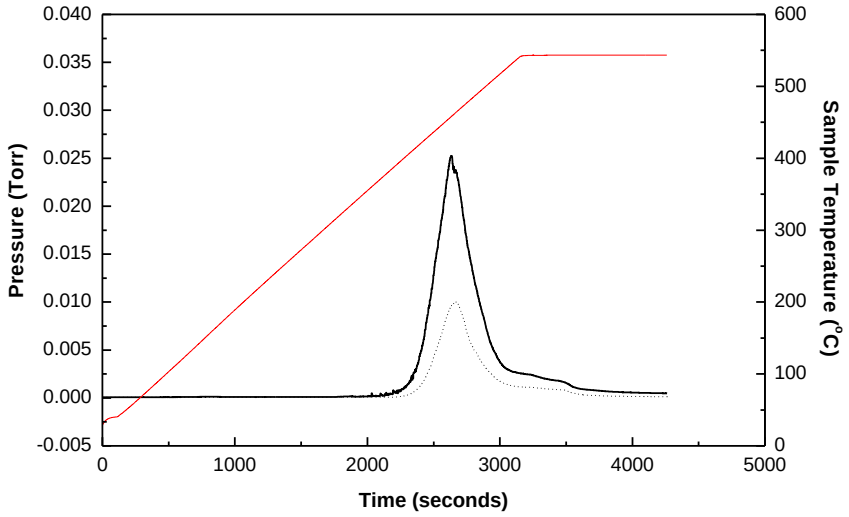

Figure 144 Replicate. Pressure measurements from the pre- and post-sub-ambient trap during thermal degradation of PET uniaxial film. The solid and dashed plots represent pressure measurements pre- and post- sub-ambient trap, respectfully. The red plot represents the furnace temperature.

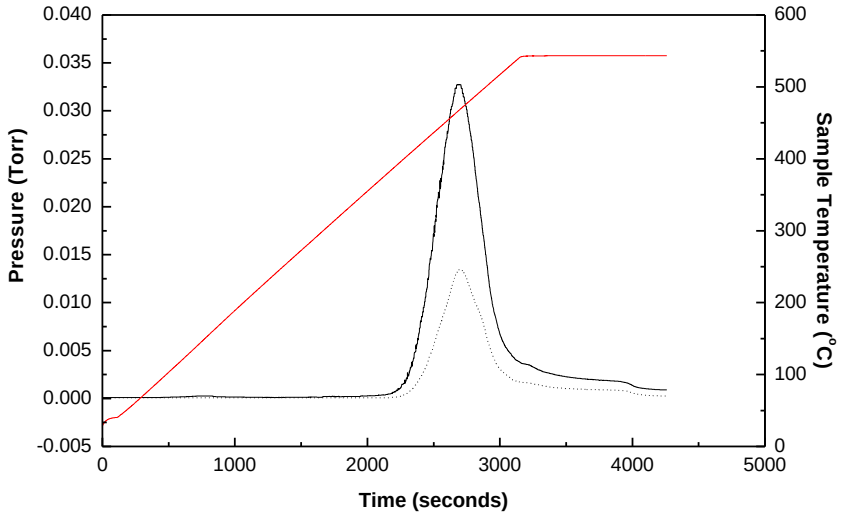

Figure 145 Replicate. Pressure measurements from the pre- and post-sub-ambient trap during thermal degradation of PET0.5G uniaxial film. The solid and dashed plots represent pressure measurements pre- and post- sub-ambient trap, respectfully. The red plot represents the furnace temperature.

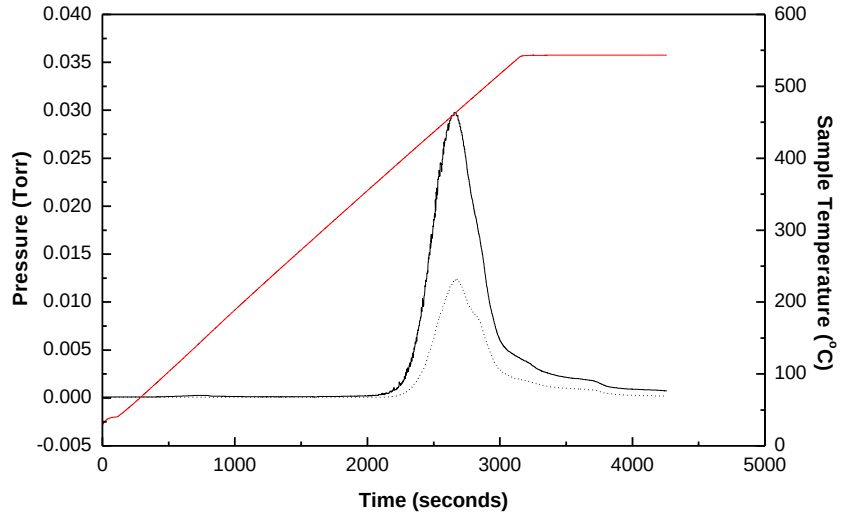

Figure 146 Replicate. Pressure measurements from the pre- and post-sub-ambient trap during thermal degradation of PET1.0G uniaxial film. The solid and dashed plots represent pressure measurements pre- and post- sub-ambient trap, respectfully. The red plot represents the furnace temperature.

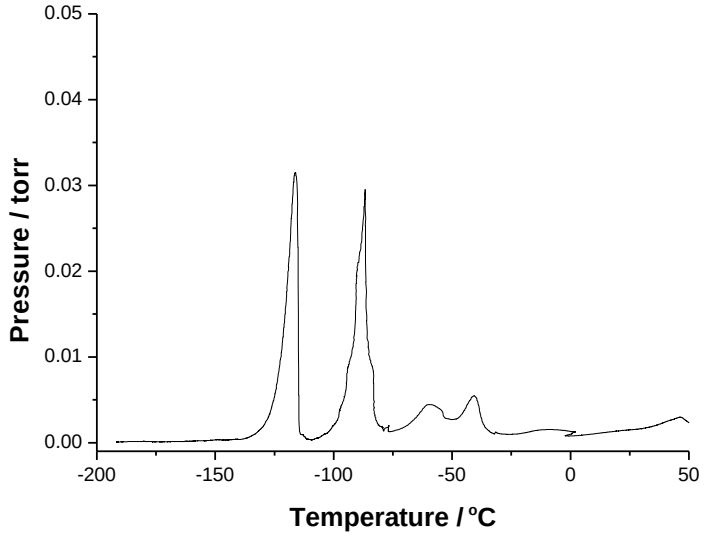

Figure 147 Replicate. Pressure measurements during the subambient TVA run of PET uniaxial film. The subambient run is performed under a 4ºC min^{-1} heating rate from -196 ºC to +40 ºC.

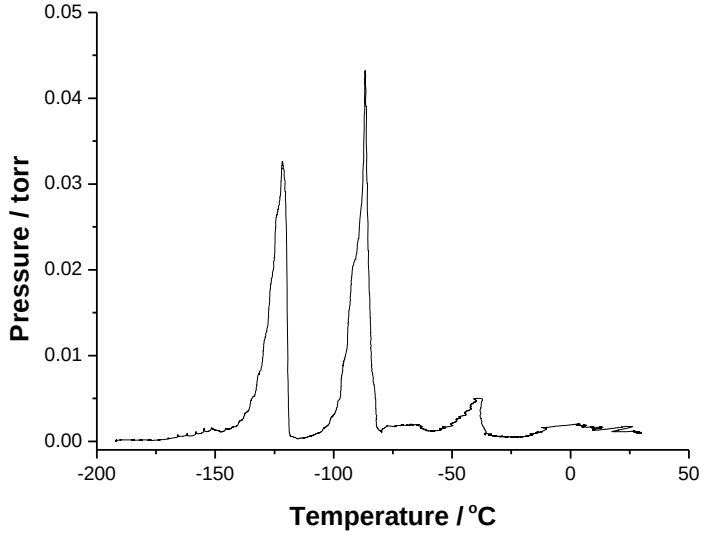

Figure 148 Replicate. Pressure measurements during the subambient TVA run of PET0.5G uniaxial film. The subambient run is performed under a 4ºC min^{-1} heating rate from -196 ºC to +40 ºC.

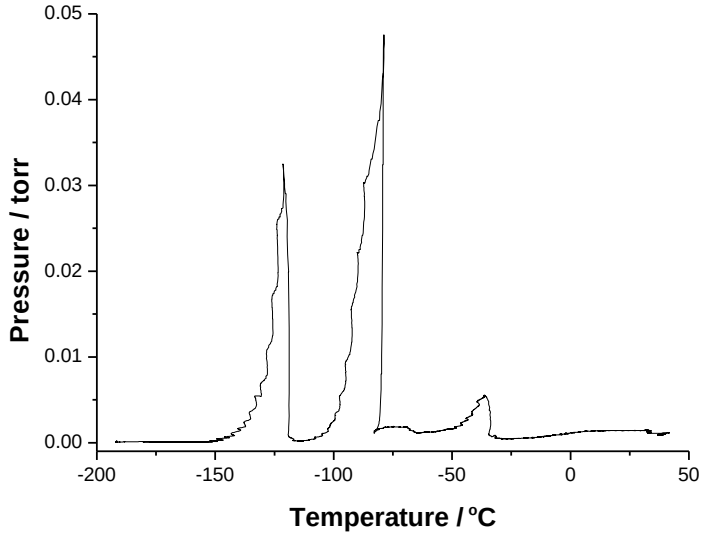

Figure 149 Replicate. Pressure measurements during the subambient TVA run of PET1.0G uniaxial film. The subambient run is performed under a 4ºC min^{-1} heating rate from -196 ºC to +40 ºC.

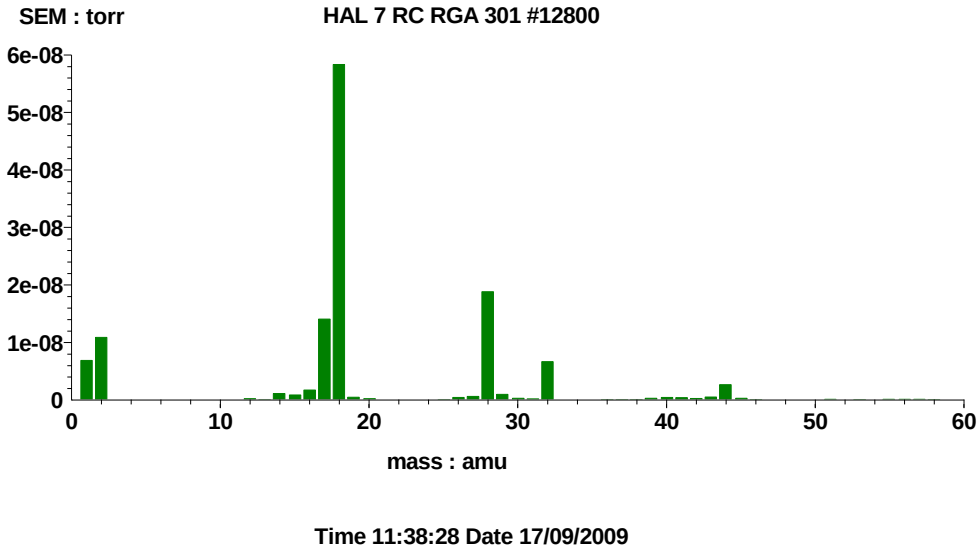

Figure 150 Cycle 420 during the TVA degradation run of PET uniaxial film.

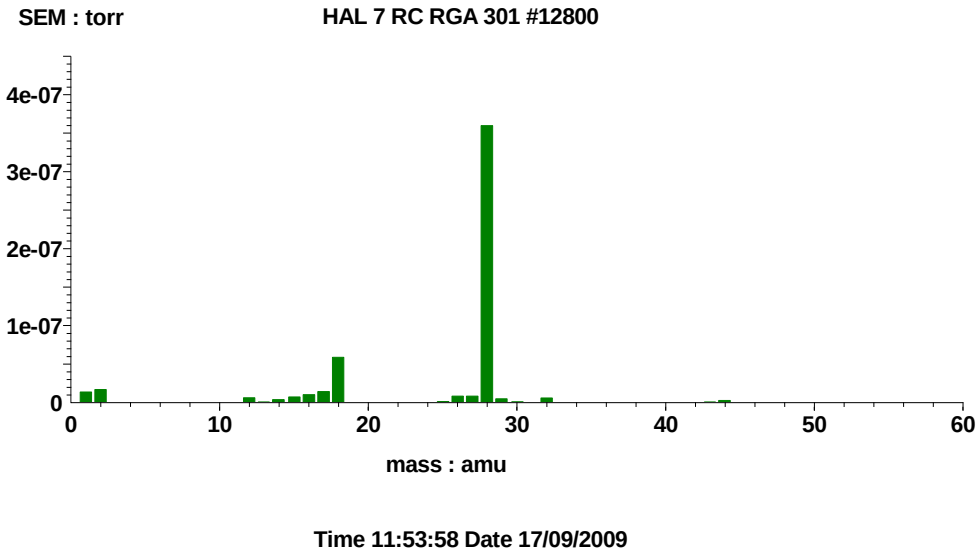

Figure 151 Cycle 710 during the TVA degradation run of PET uniaxial film.

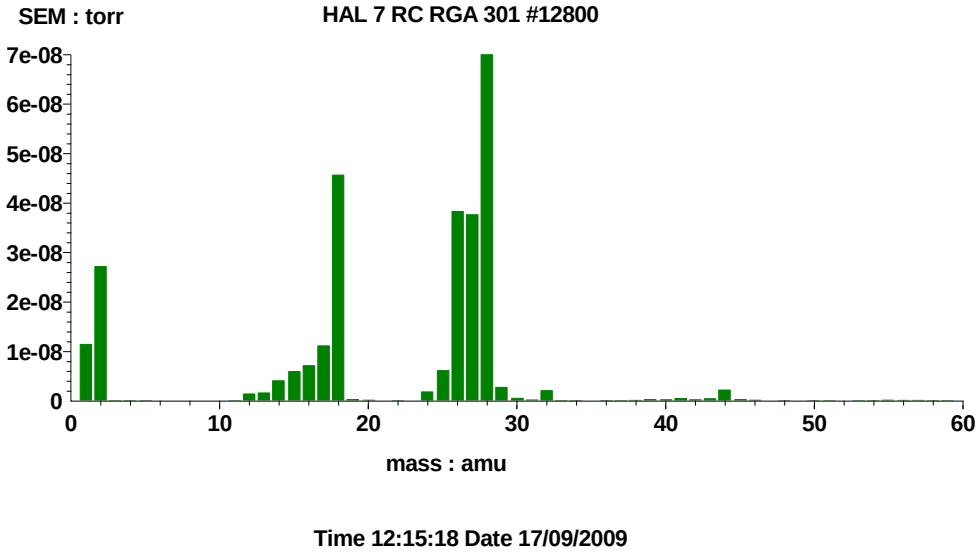

Figure 152 Cycle 1109 during the TVA degradation run of PET uniaxial film.

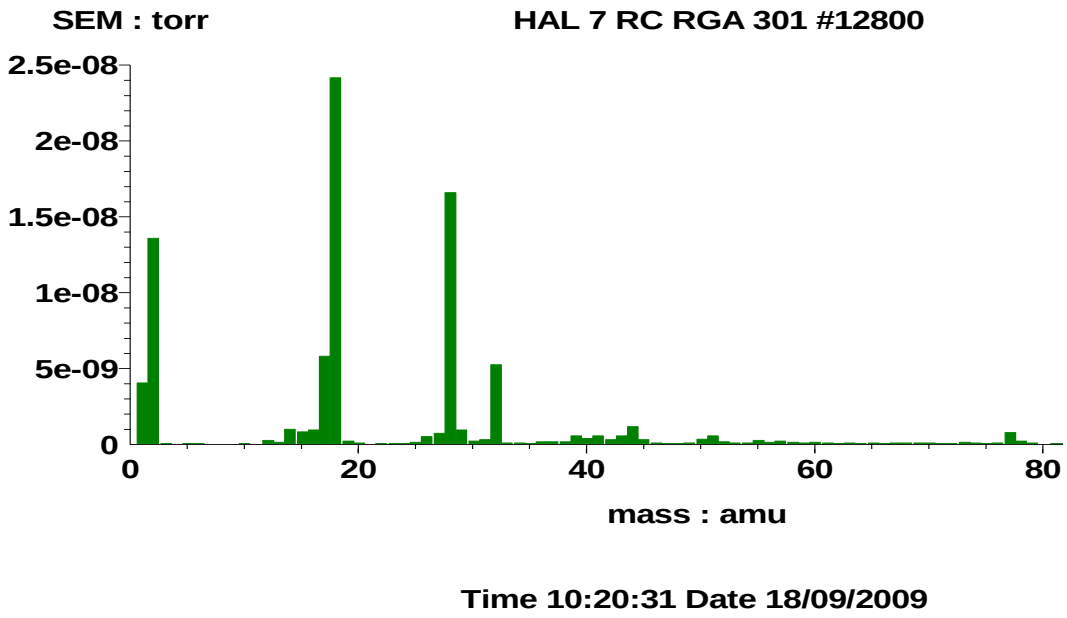

Figure 153 Cycle 420 during the TVA degradation run of PET0.5G uniaxial film.

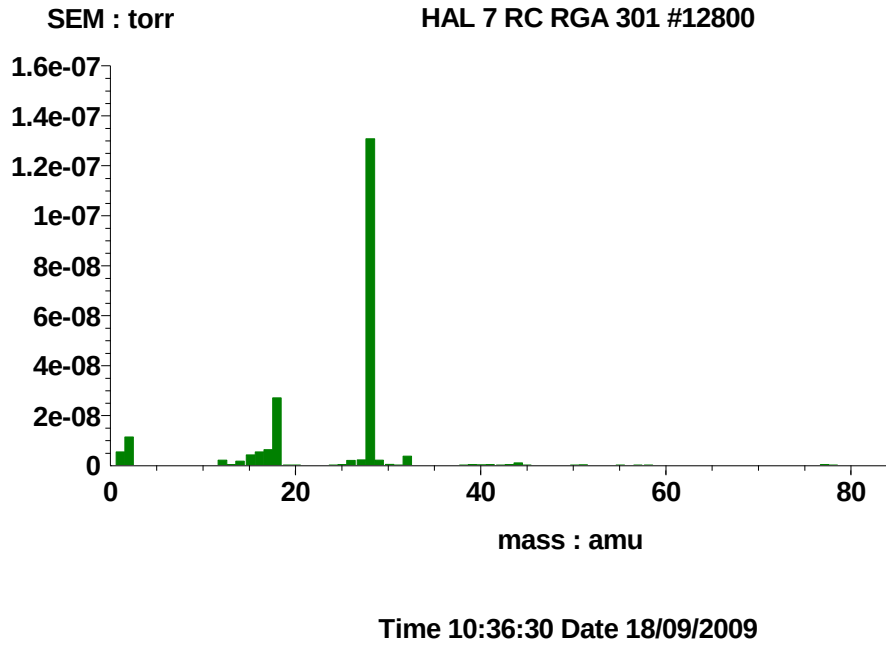

Figure 154 Cycle 720 during the TVA degradation run of PET0.5G uniaxial film.

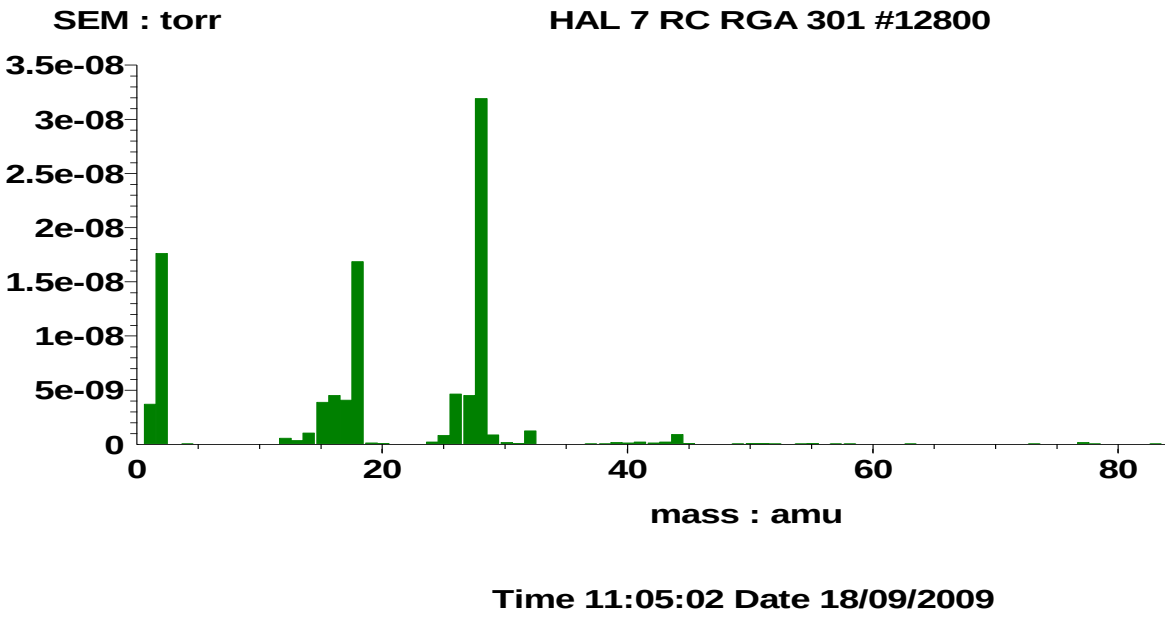

Figure 155 Cycle 1109 during the TVA degradation run of PET0.5G uniaxial film.

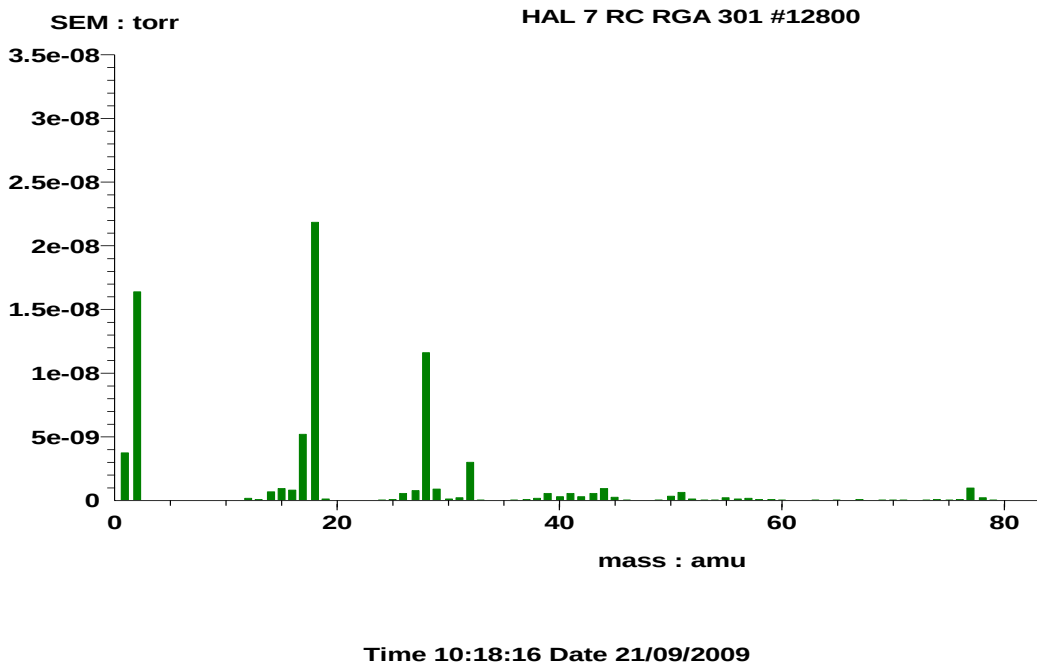

Figure 156 Cycle 420 during the TVA degradation run of PET1.0G uniaxial film.

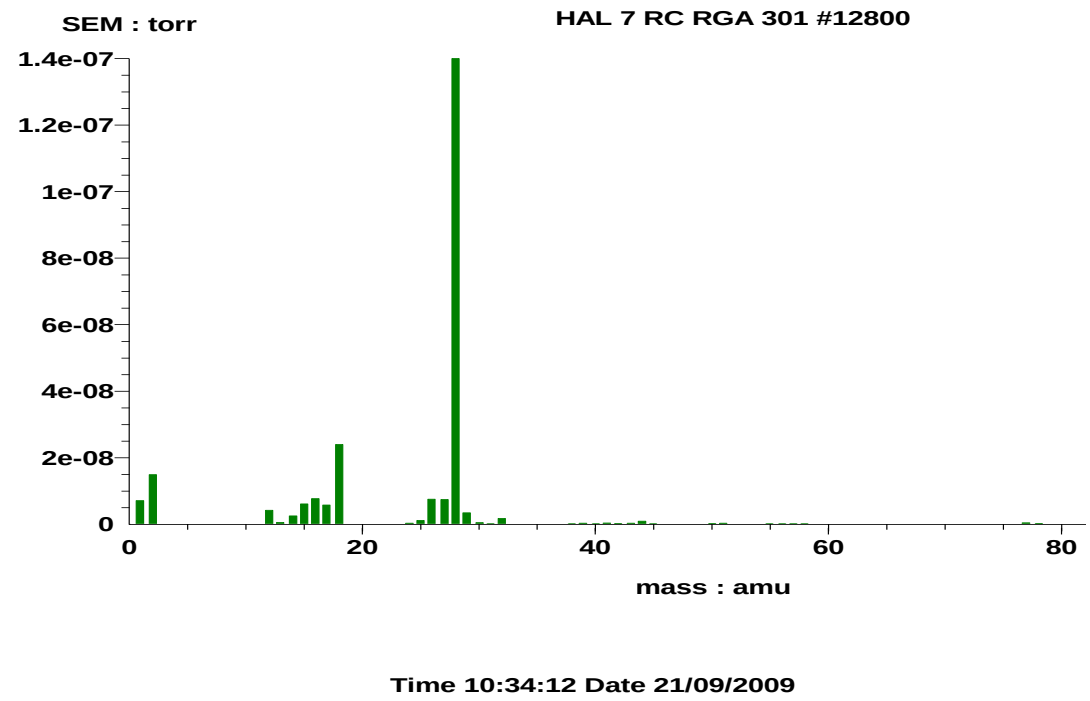

Figure 157 Cycle 718 during the TVA degradation run of PET1.0G uniaxial film.

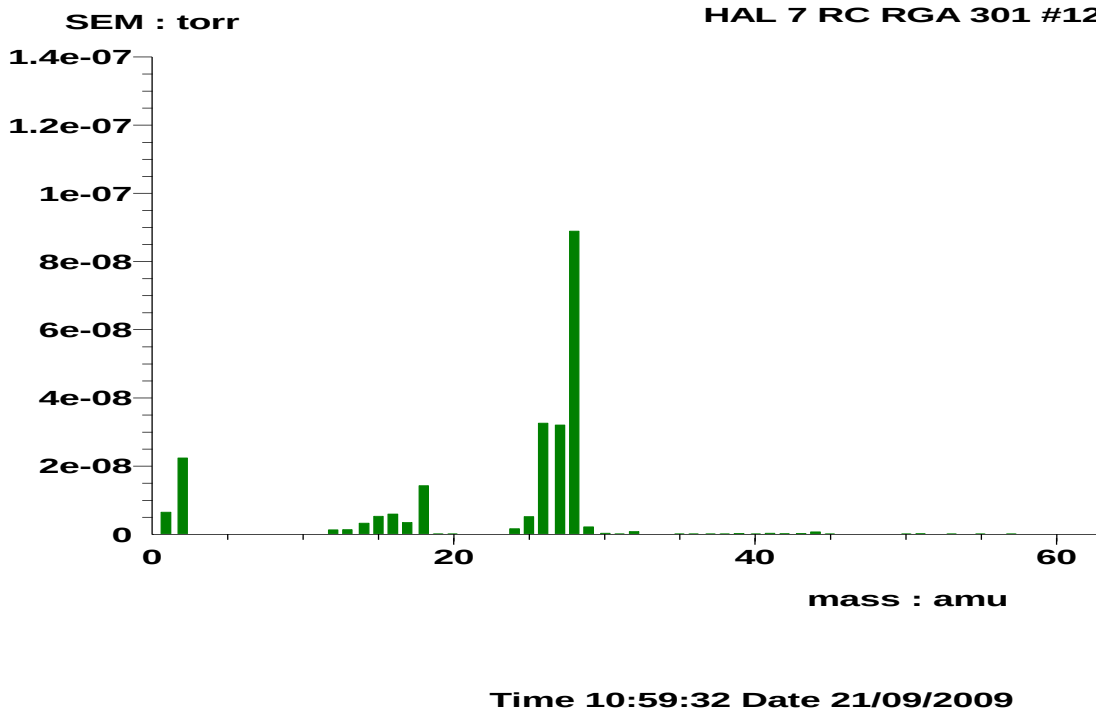

Figure 158 Cycle 1192 during the TVA degradation run of PET1.0G uniaxial film.

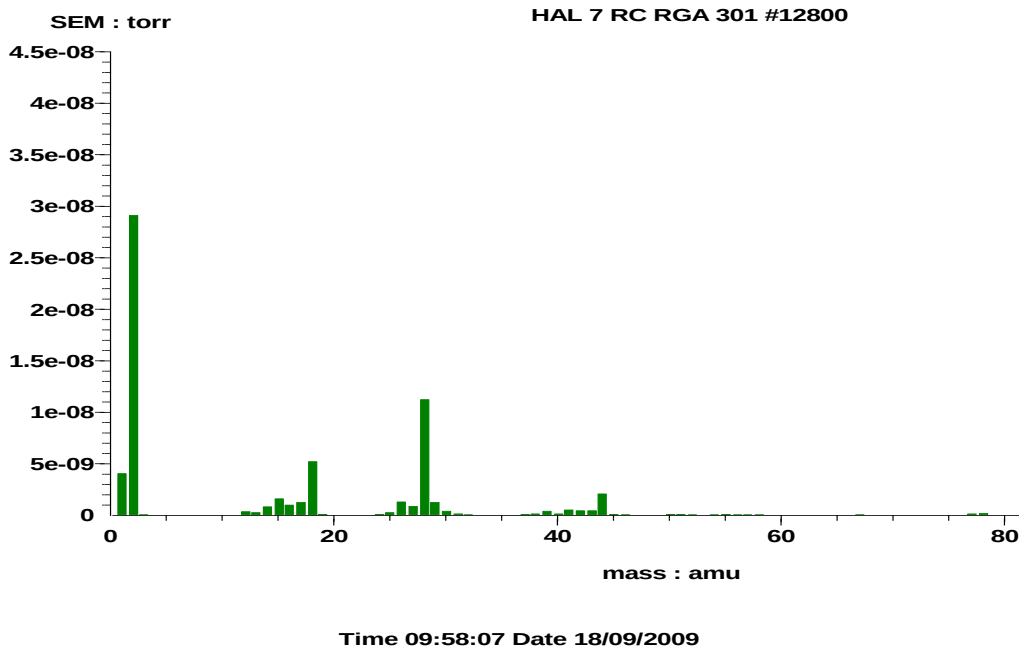

Figure 159 Mass spectrum of fraction 1 (cycle 34) during the SATVA run of PET0.5G uniaxial film.

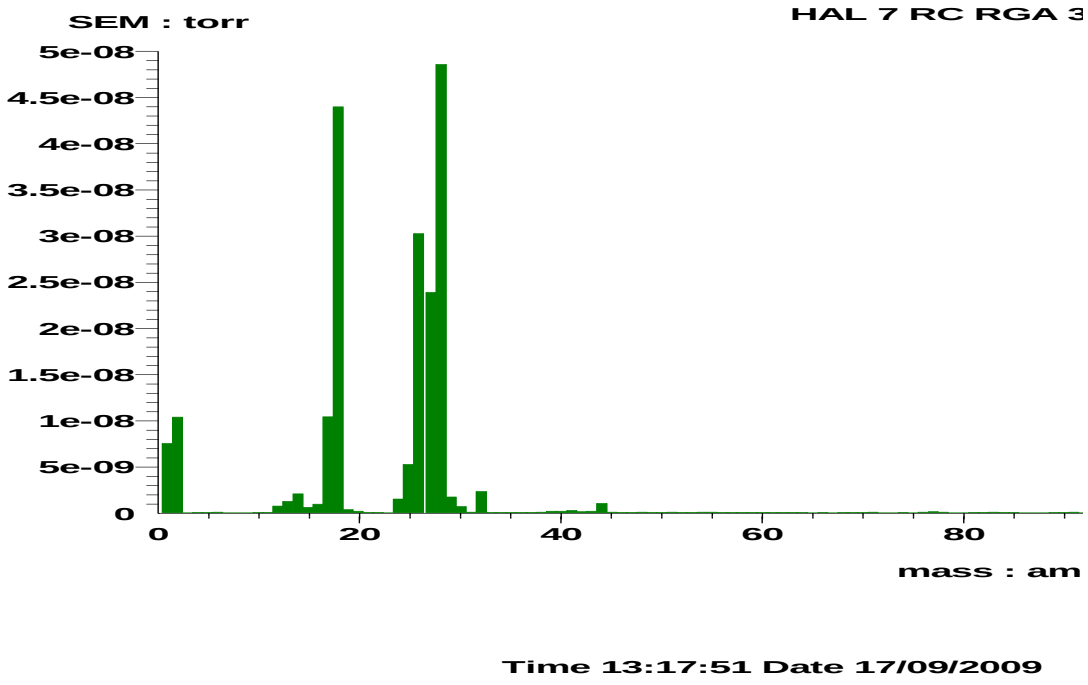

Figure 160 Mass spectrum of fraction 1 (cycle 57) during the SATVA run of PET0.5G uniaxial film.

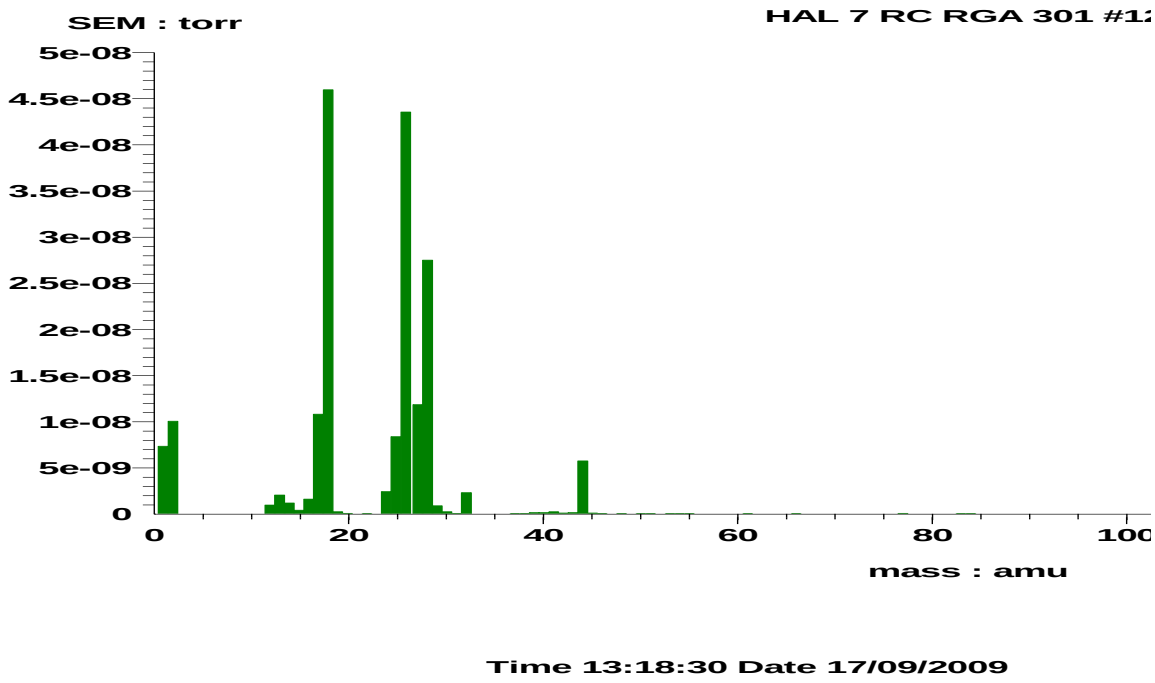

Figure 161 Mass spectrum of fraction 1 (cycle 62) during the SATVA run of PET0.5G uniaxial film.

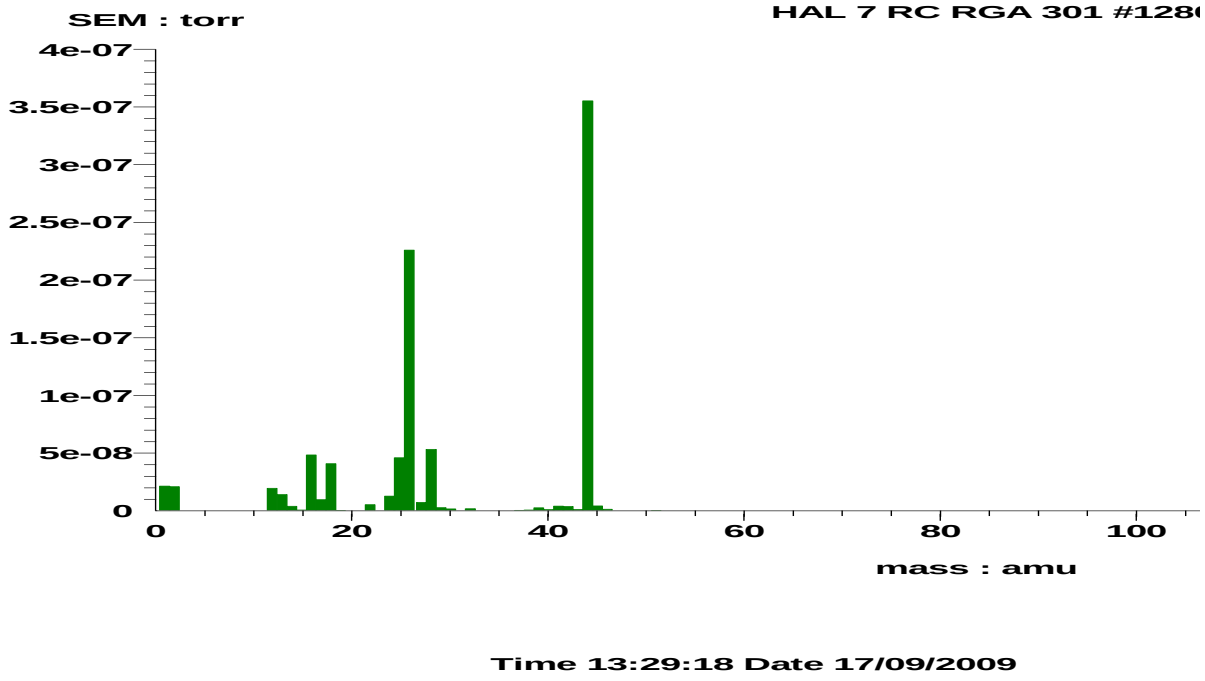

Figure 162 Mass spectrum of fraction 1 (cycle 146) during the SATVA run of PET0.5G uniaxial film.

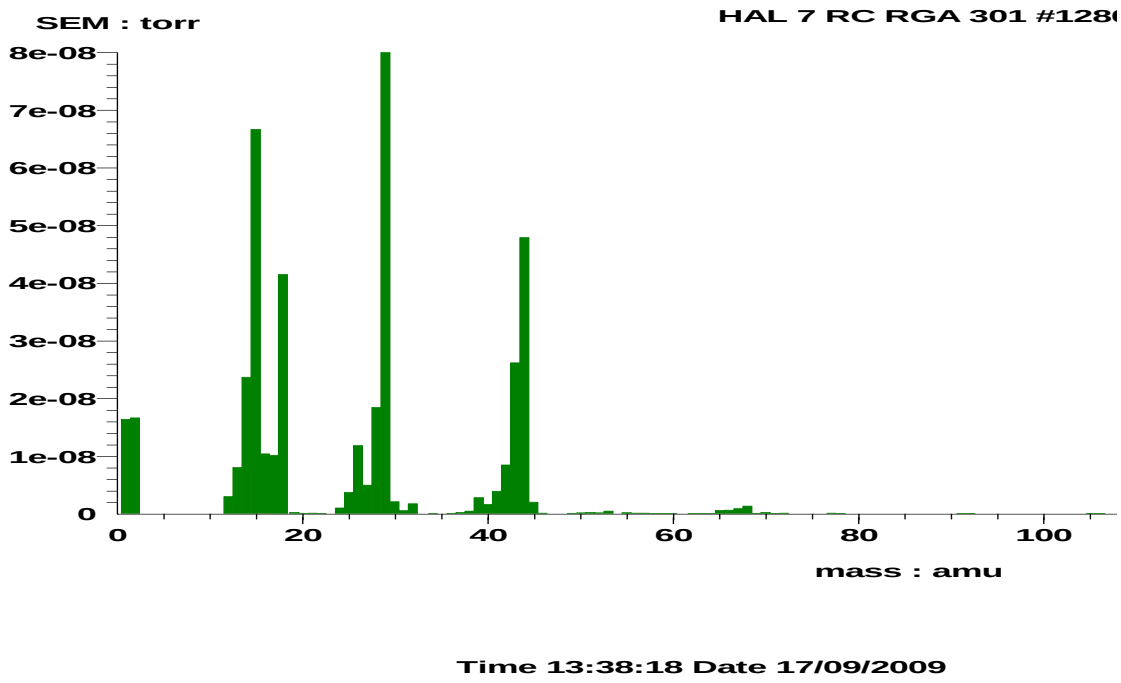

Figure 163 Mass spectrum of fraction 2 (cycle 216) during the SATVA run of PET0.5G uniaxial film.

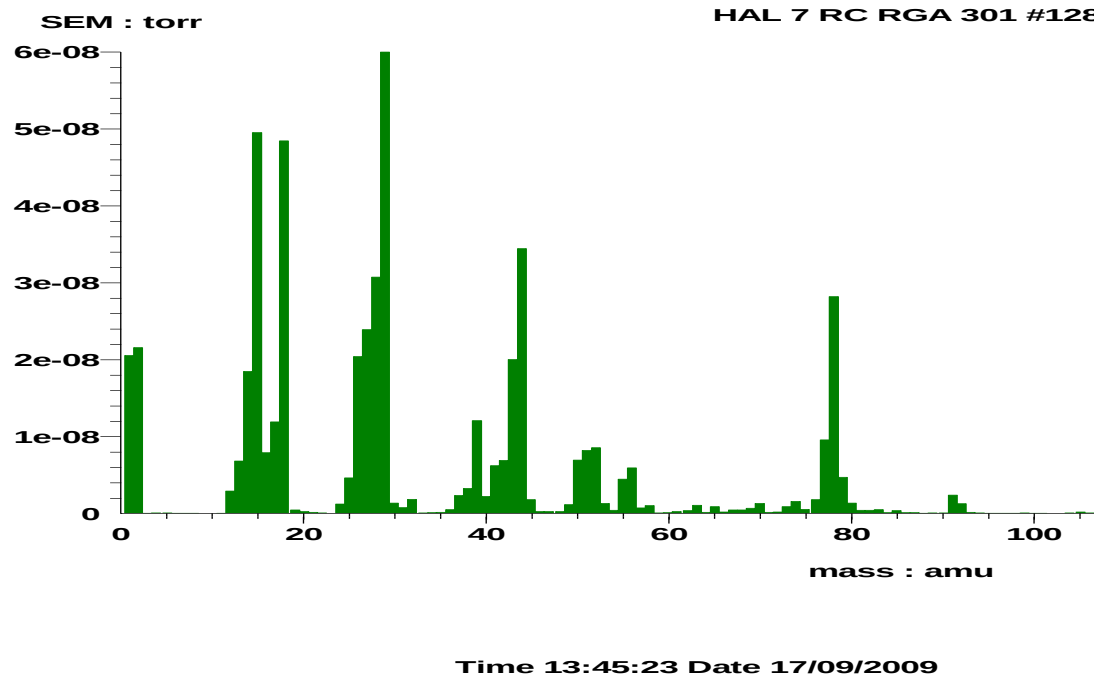

Figure 164 Mass spectrum of fraction 2 (cycle 271) during the SATVA run of PET0.5G uniaxial film.

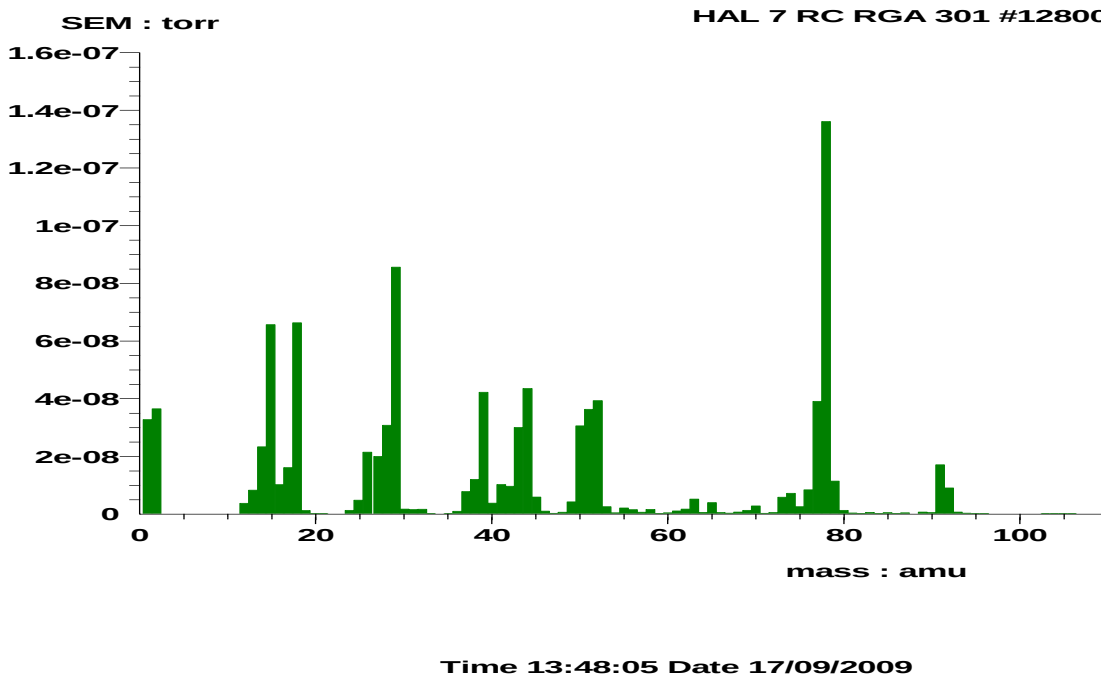

Figure 165 Mass spectrum of fraction 3 (cycle 292) during the SATVA run of PET0.5G uniaxial film.

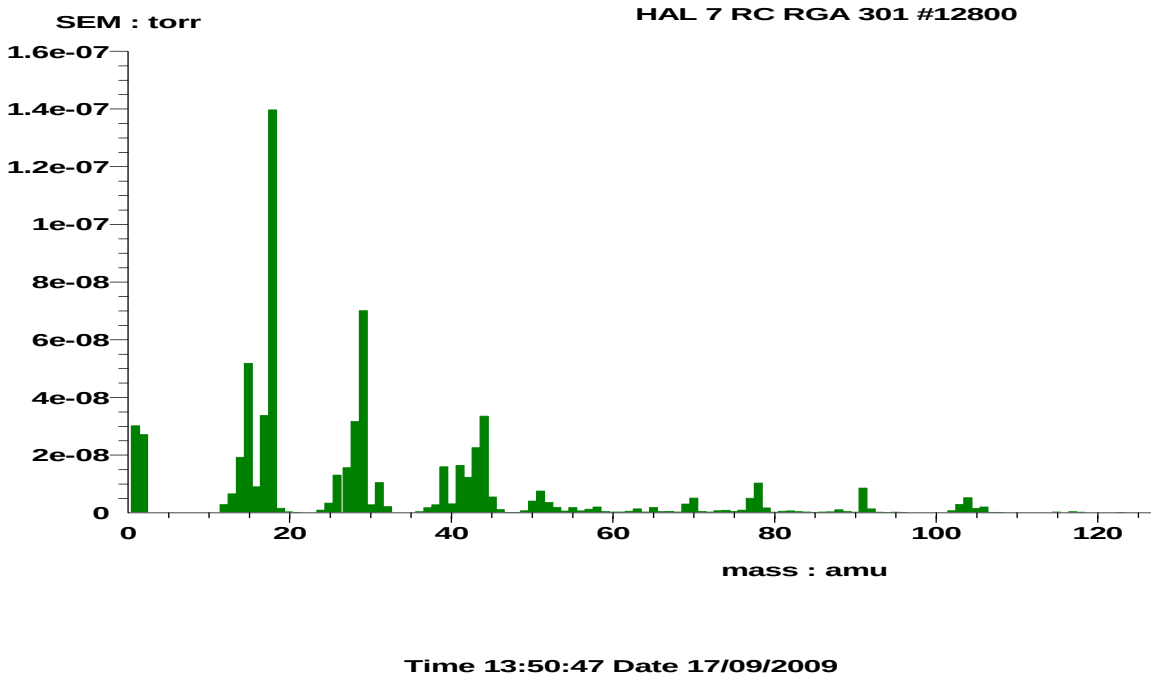

Figure 166 Mass spectrum of fraction 3 (cycle 313) during the SATVA run of PET0.5G uniaxial film.

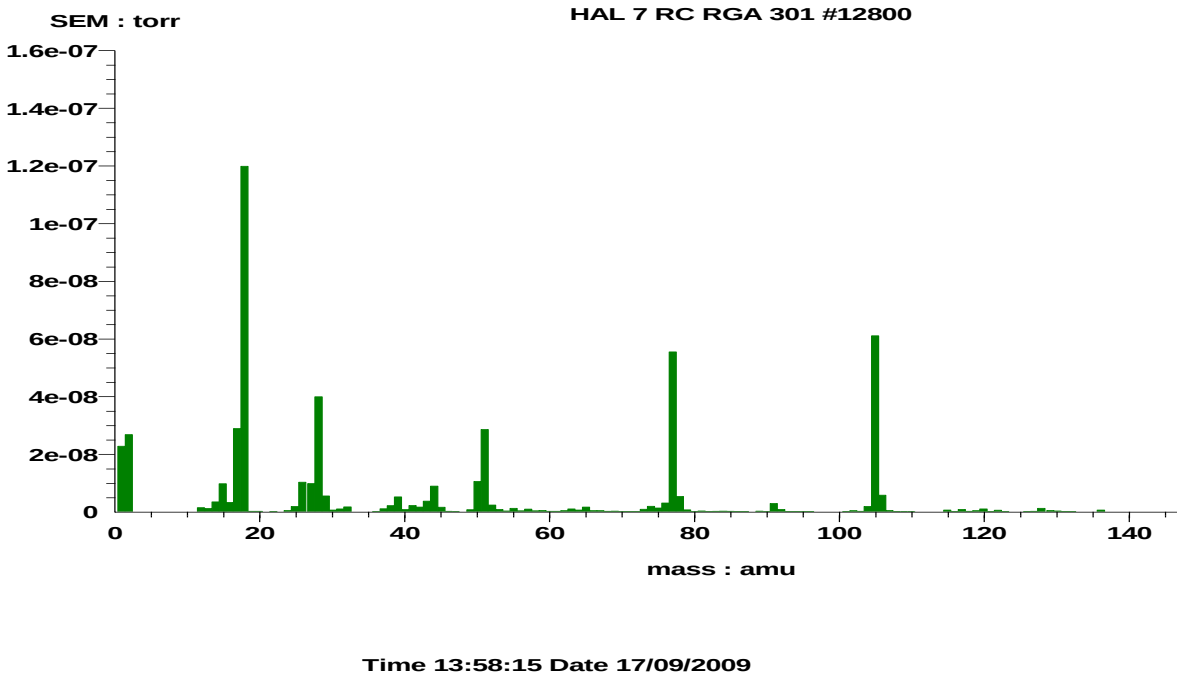

Figure 167 Mass spectrum of fraction 3 (cycle 371) during the SATVA run of PET0.5G uniaxial film.

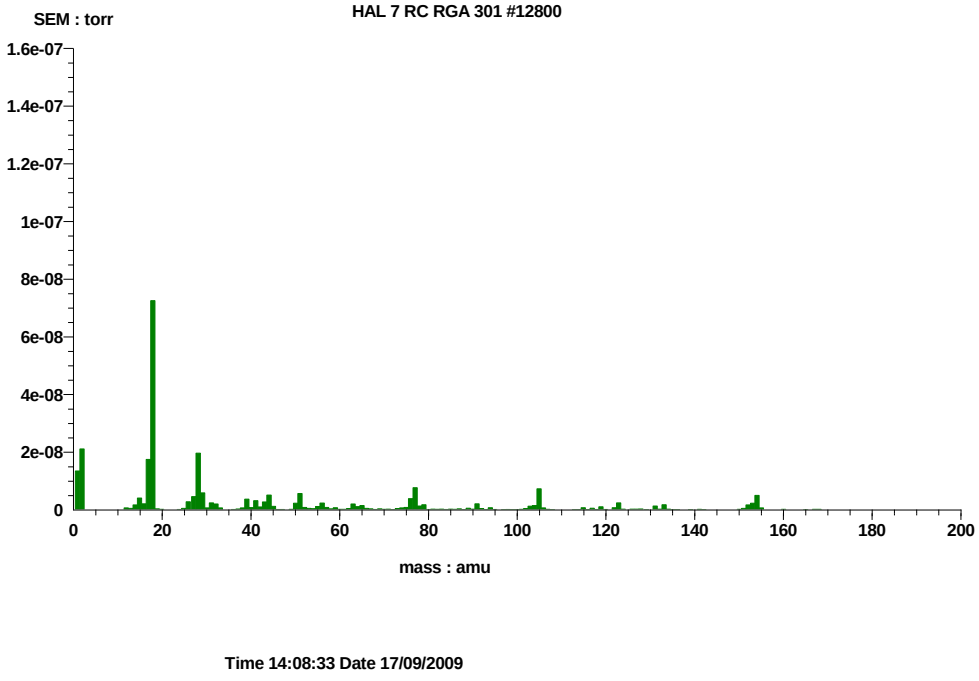

Figure 168 Mass spectrum of fraction 4 (cycle 453) during the SATVA run of PET0.5G uniaxial film.

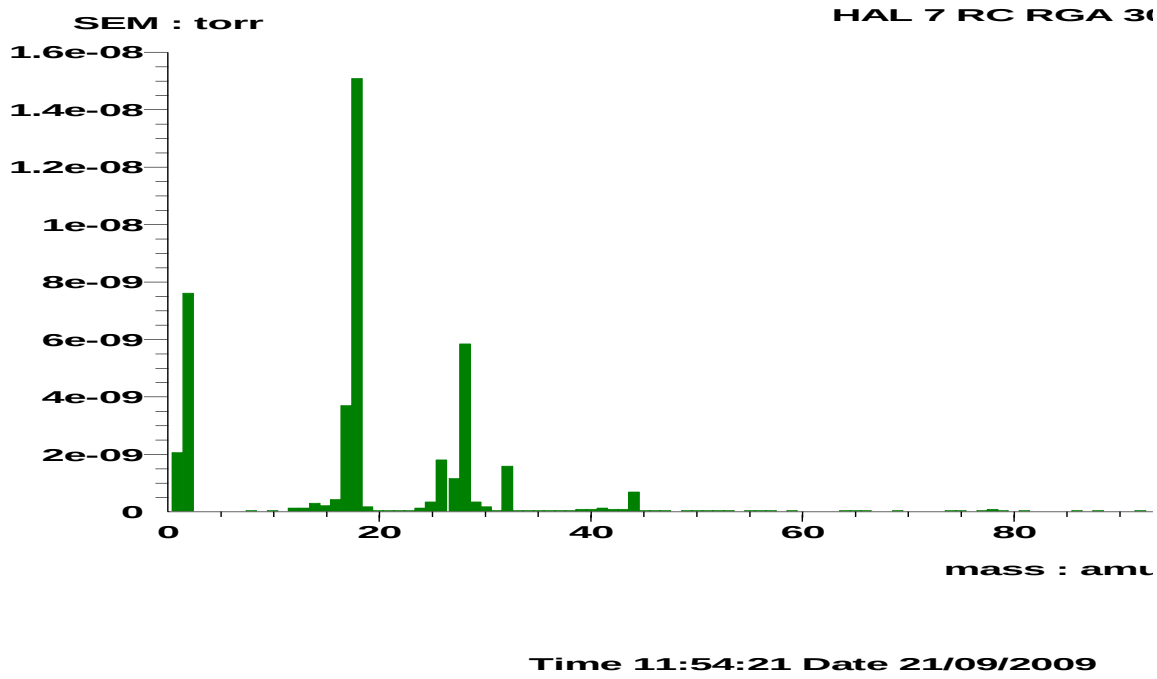

Figure 169 Mass spectrum of fraction 1 (cycle 34) during the SATVA run of PET1.0G uniaxial film.

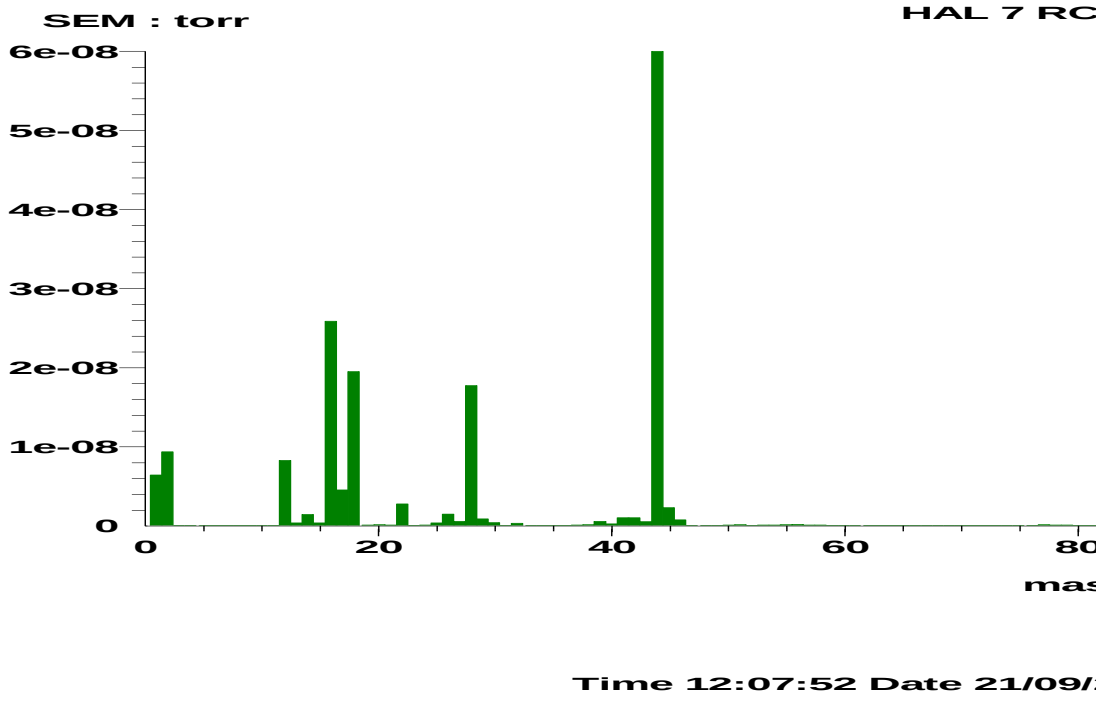

Figure 170 Mass spectrum of fraction 1 (cycle 139) during the SATVA run of PET1.0G uniaxial film.

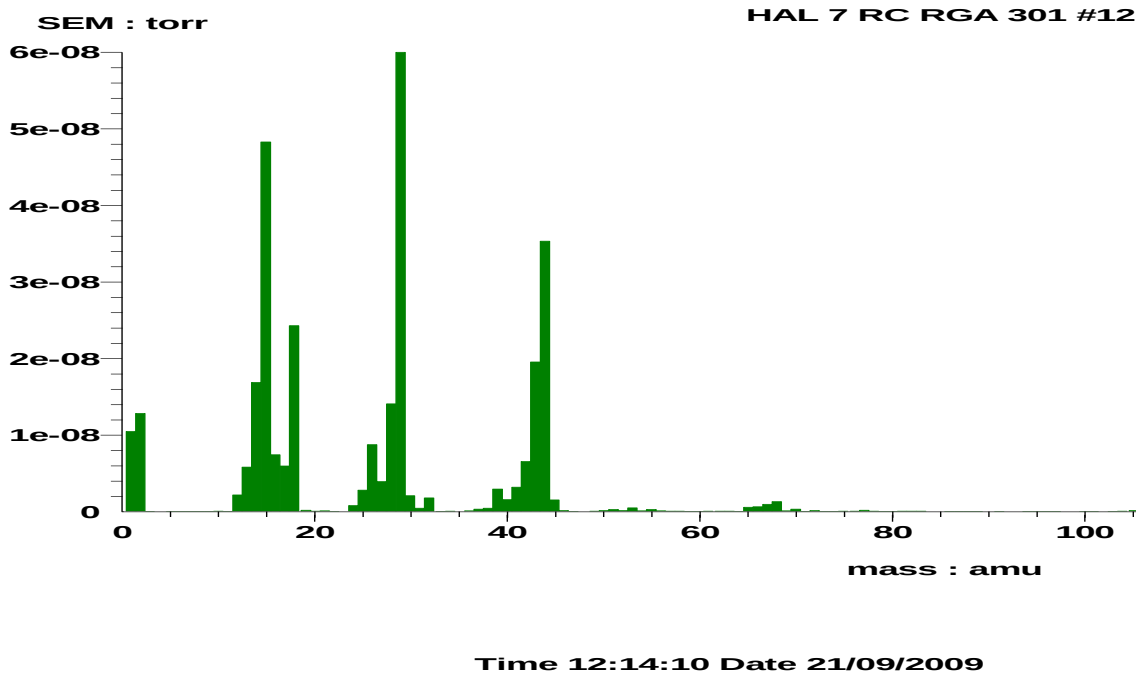

Figure 171 Mass spectrum of fraction 2 (cycle 188) during the SATVA run of PET1.0G uniaxial film.

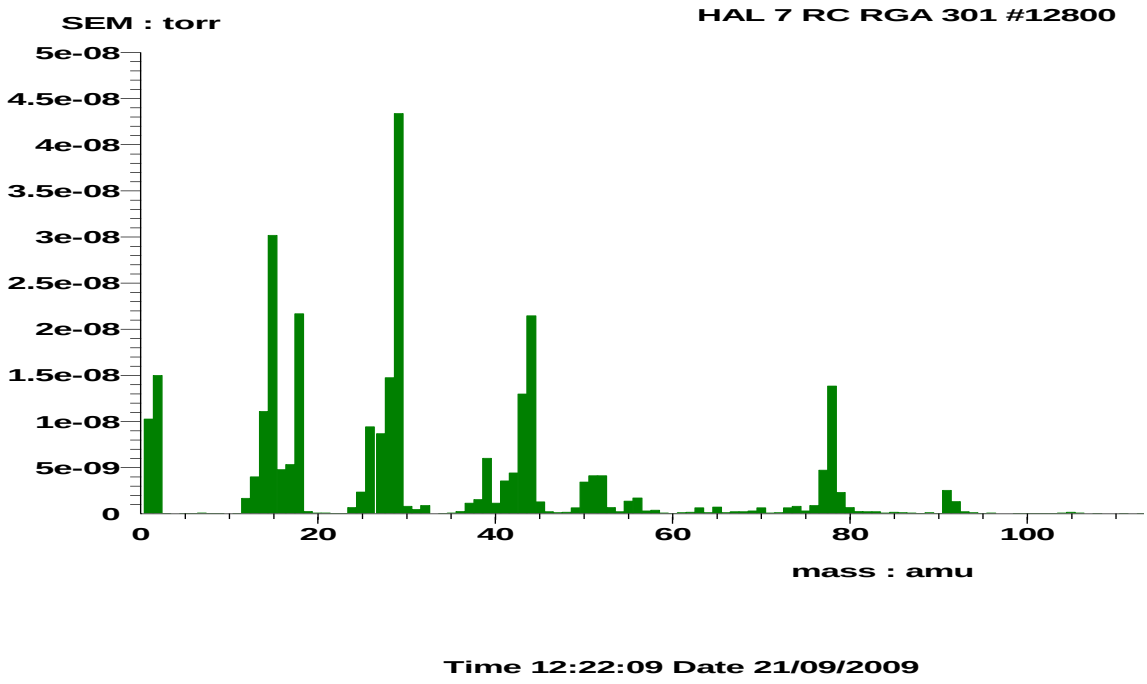

Figure 172 Mass spectrum of fraction 3 (cycle 250) during the SATVA run of PET1.0G uniaxial film.

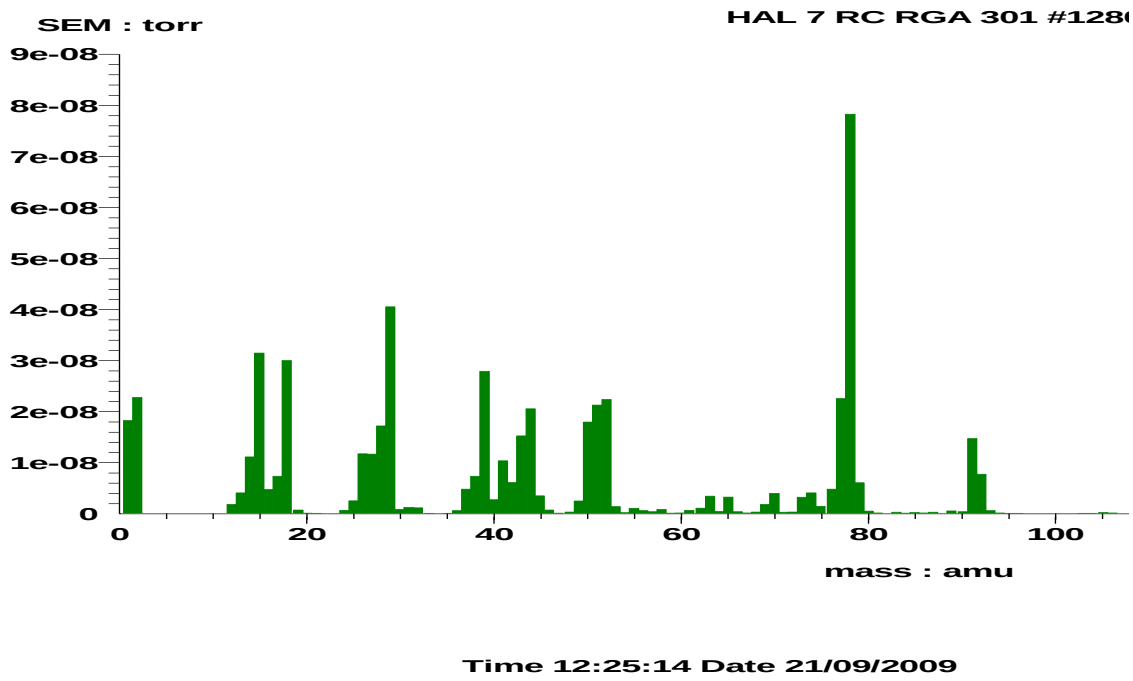

Figure 173 Mass spectrum of fraction 3 (cycle 274) during the SATVA run of PET1.0G uniaxial film.

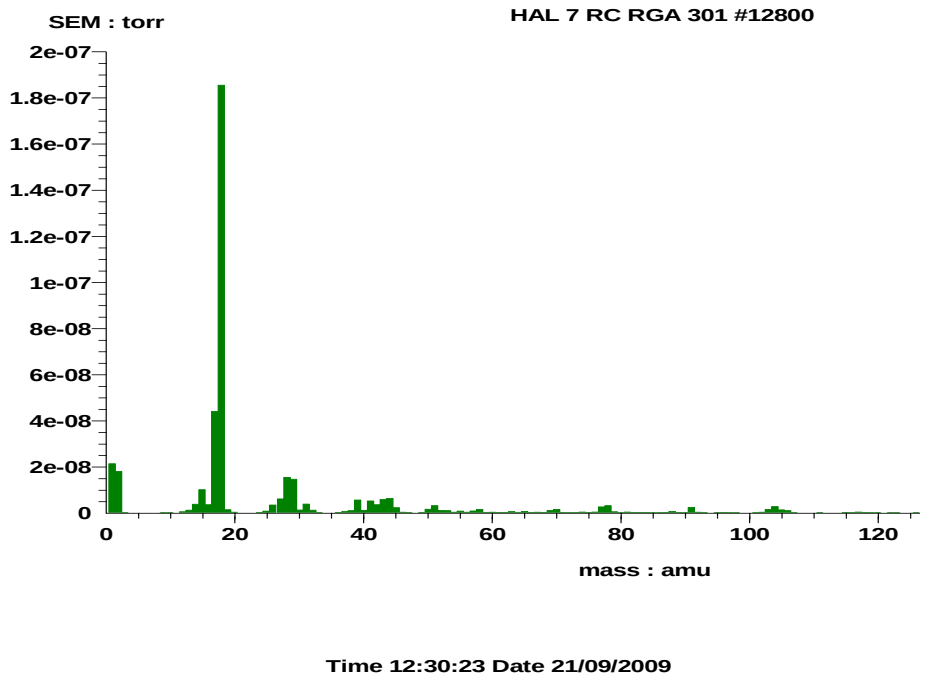

Figure 174 Mass spectrum of fraction 3 (cycle 314) during the SATVA run of PET1.0G uniaxial film.

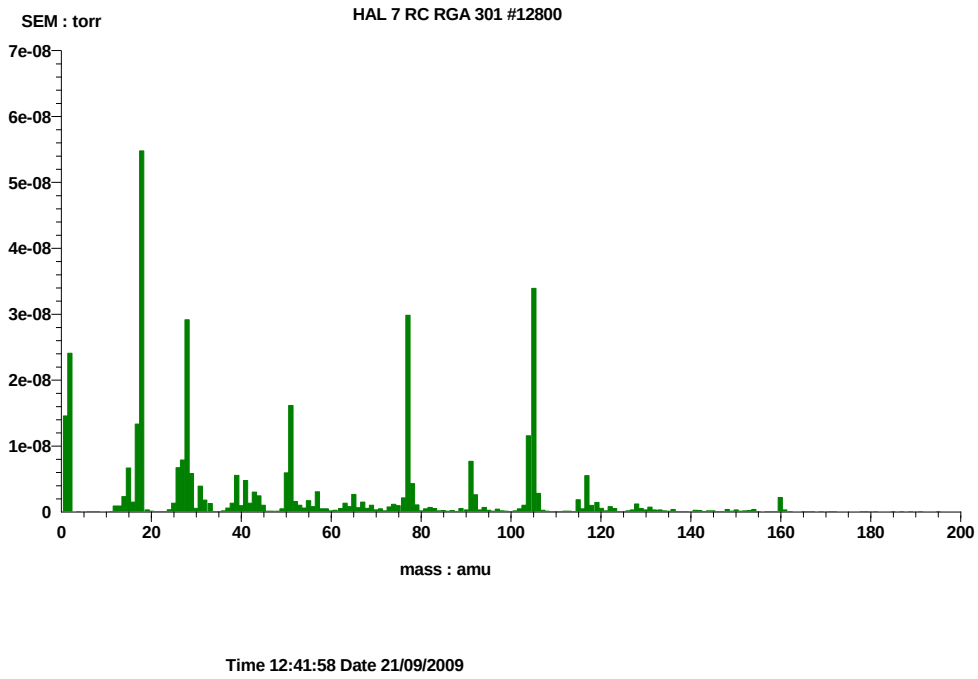

Figure 175 Mass spectrum of fraction 4 (cycle 404) during the SATVA run of PET1.0G uniaxial film.

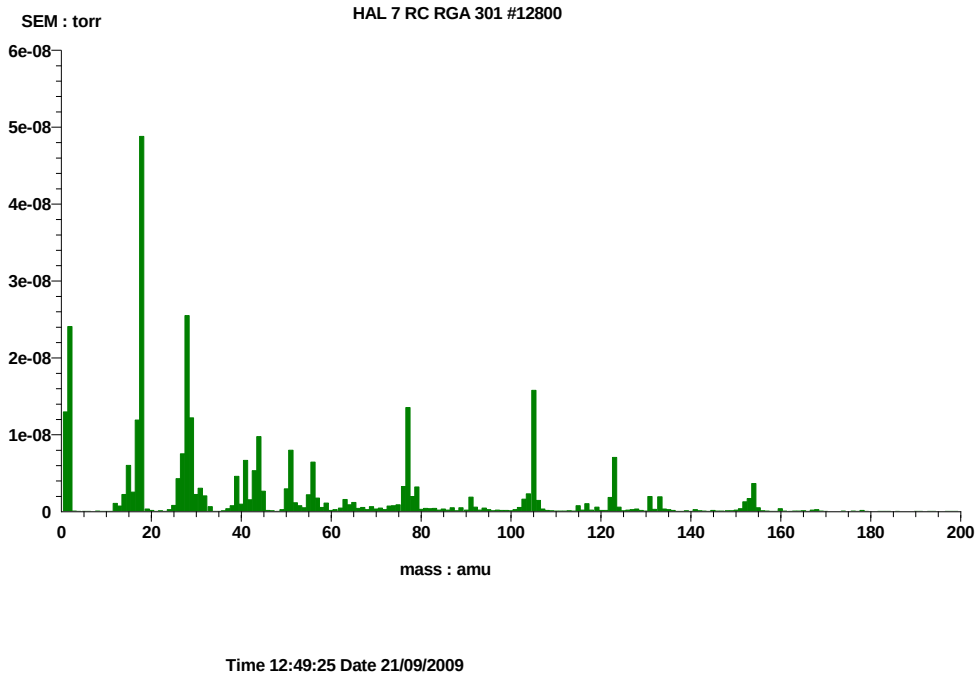

Figure 176 Mass spectrum of fraction 4 (cycle 462) during the SATVA run of PET1.0G uniaxial film.

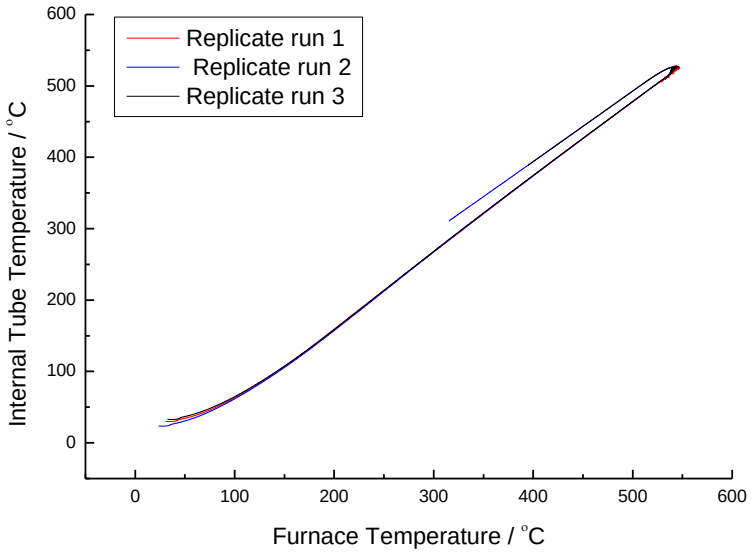

Figure 177 Calibration plot of TVA tube C

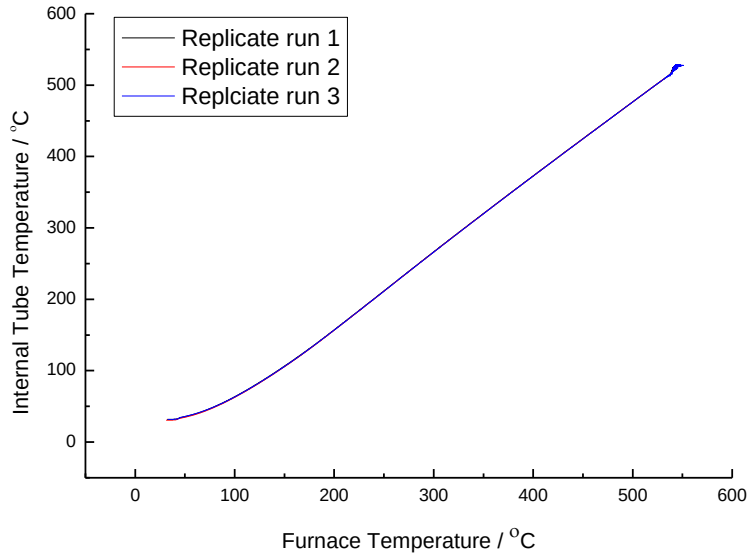

Figure 178 Calibration plot of TVA tube Z

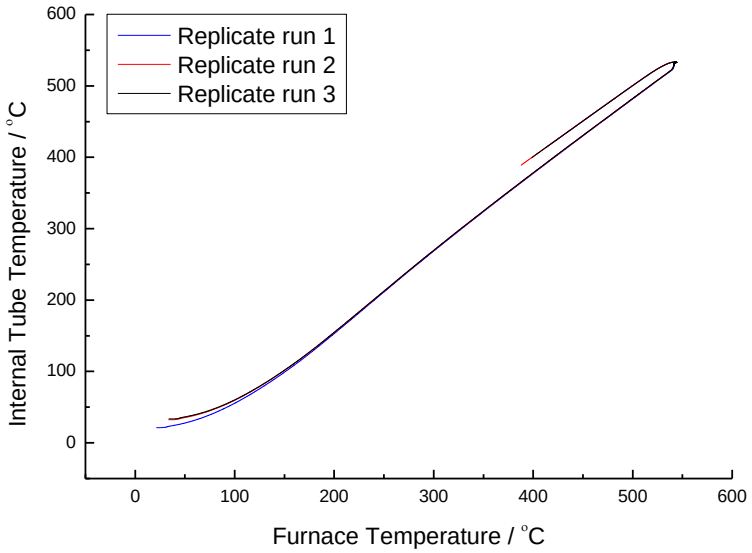

Figure 179 Calibration plot of TVA tube 4

APPENDIX 7: THERMAL DEGRADATION KINETICS

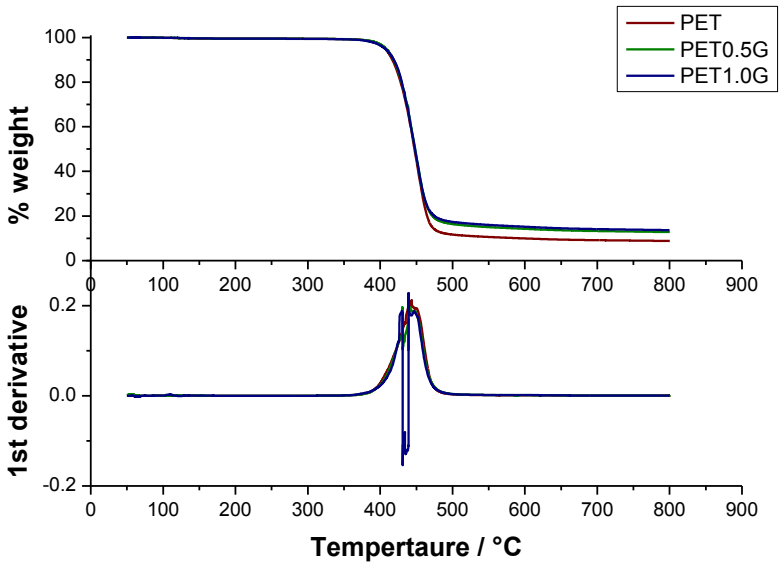

Figure 180 Duplicate dynamic, non-oxidative degradation TGA runs for PET, PET0.5G and PET1.0G. Runs were performed under helium.

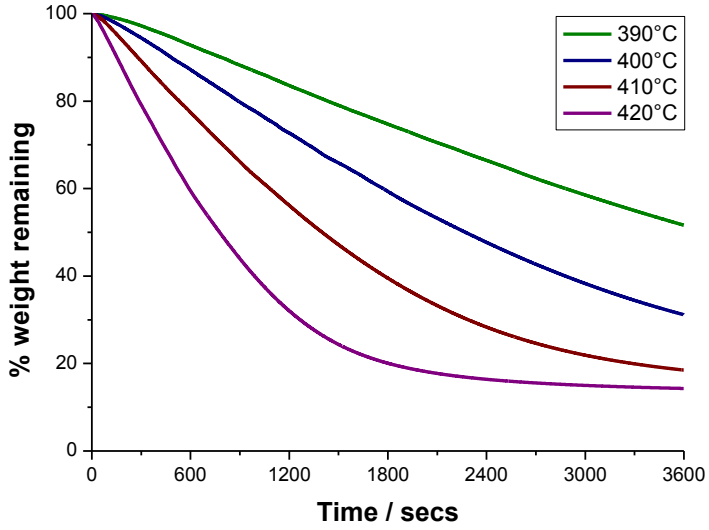

Figure 181 Duplicate isothermal degradative plots for PET uniaxial film between 390ºC and 420ºC. The isothermal was held for 1 hour. Analysis was performed under helium.

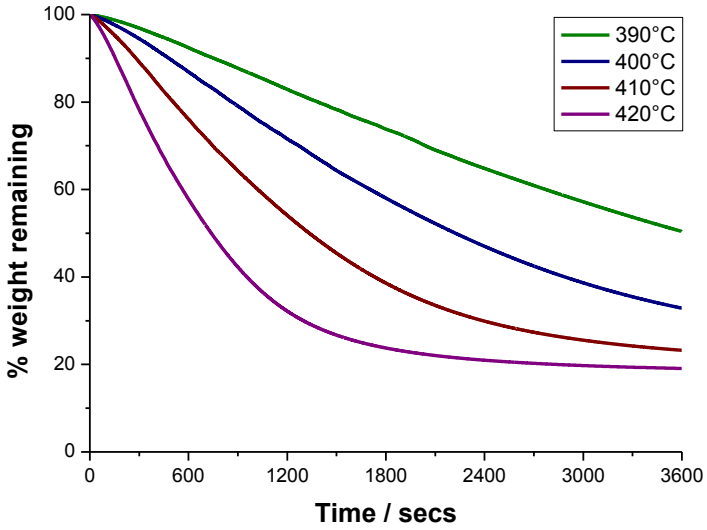

Figure 182 Isothermal degradative plots for PET0.5G uniaxial film between 390ºC and 420ºC. The isothermal was held for 1 hour. Analysis was performed under helium.

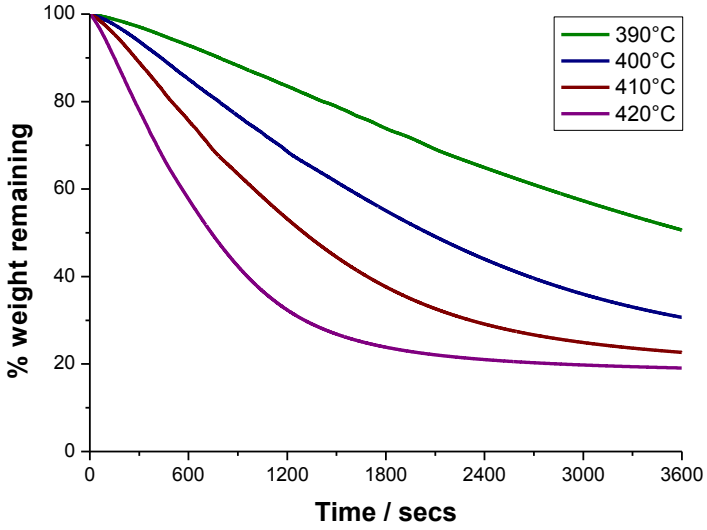

Figure 183 Duplicate isothermal degradative plots for PET0.5G uniaxial film between 390ºC and 420ºC. The isothermal was held for 1 hour. Analysis was performed under helium.

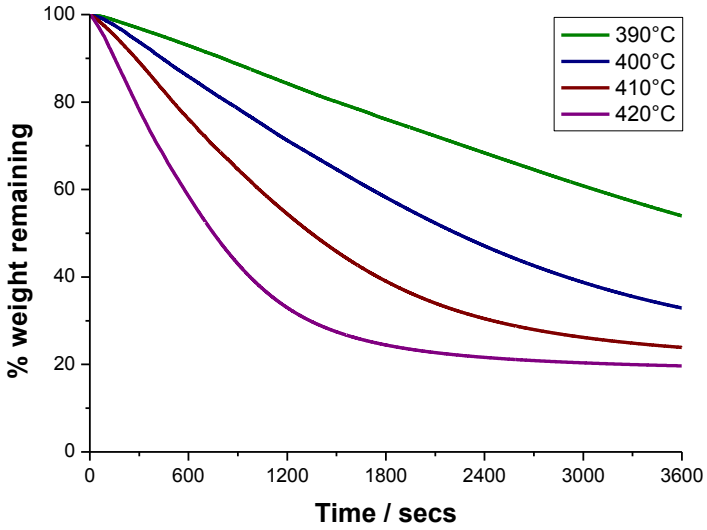

Figure 184 Isothermal degradative plots for PET1.0G uniaxial film between 390ºC and 420ºC. The isothermal was held for 1 hour. Analysis was performed under helium.

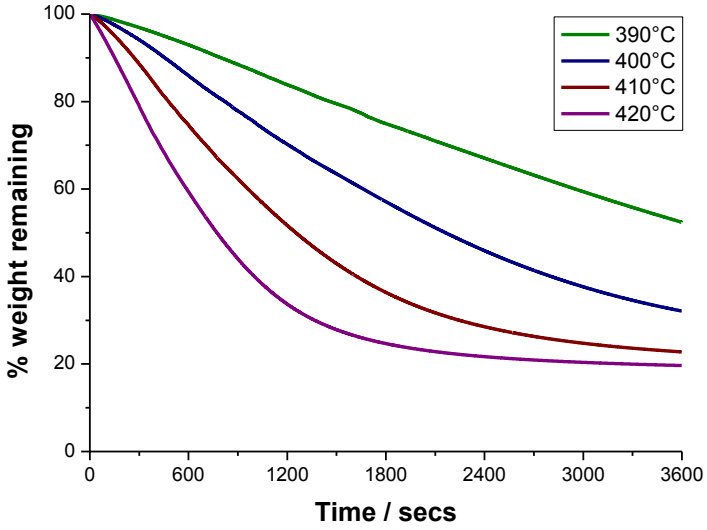

Figure 185 Duplicate isothermal degradative plots for PET1.0G uniaxial film between 390ºC and 420ºC. The isothermal was held for 1 hour. Analysis was performed under helium.

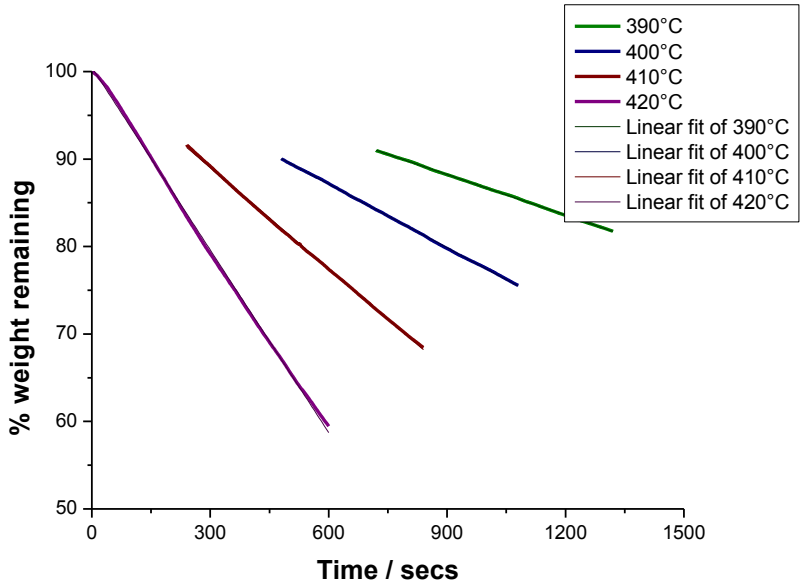

Figure 186 Duplicate plot of regions of maximum weight loss during the isothermal degradation plots for PET uniaxial film between 390ºC and 420ºC. Analysis was performed under helium. Linear fittings were also performed.

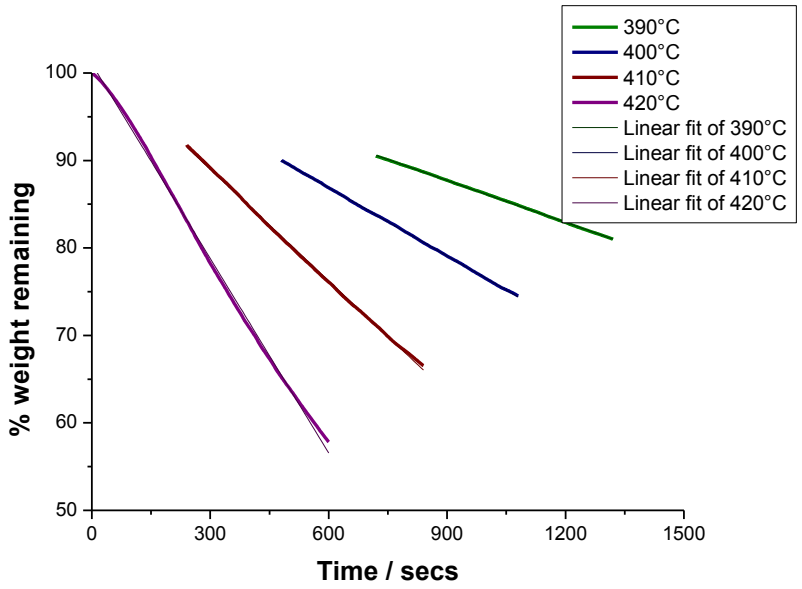

Figure 187 Regions of maximum weight loss during the isothermal degradation plots for PET0.5G uniaxial film between 390ºC and 420ºC. Analysis was performed under helium. Linear fittings were also performed.

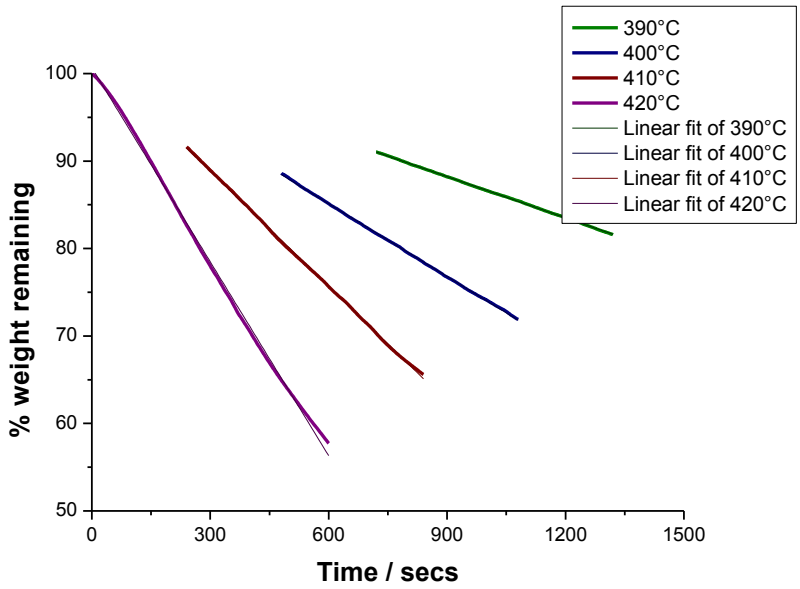

Figure 188 Duplicate plot of regions of maximum weight loss during the isothermal degradation plots for PET0.5G uniaxial film between 390ºC and 420ºC. Analysis was performed under helium. Linear fittings were also performed.

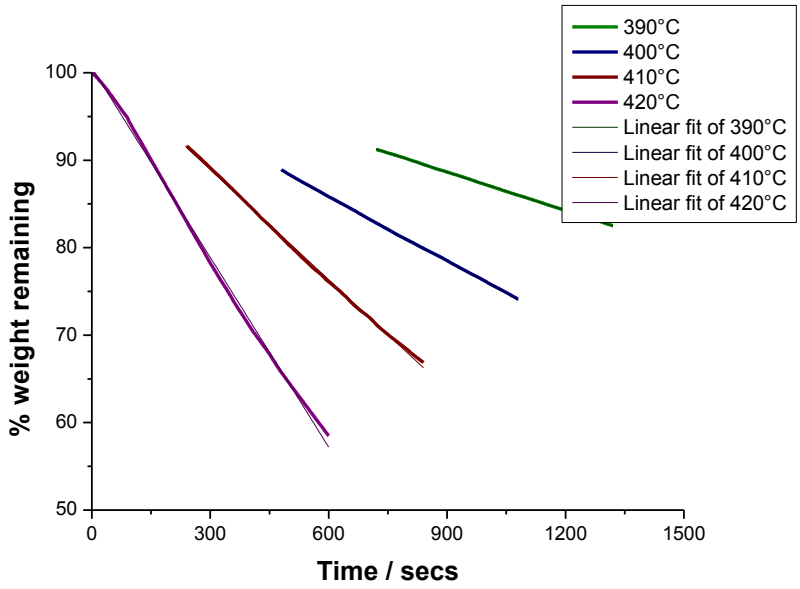

Figure 189 Regions of maximum weight loss during the isothermal degradation plots for PET1.0G uniaxial film between 390ºC and 420ºC. Analysis was performed under helium. Linear fittings were also performed.

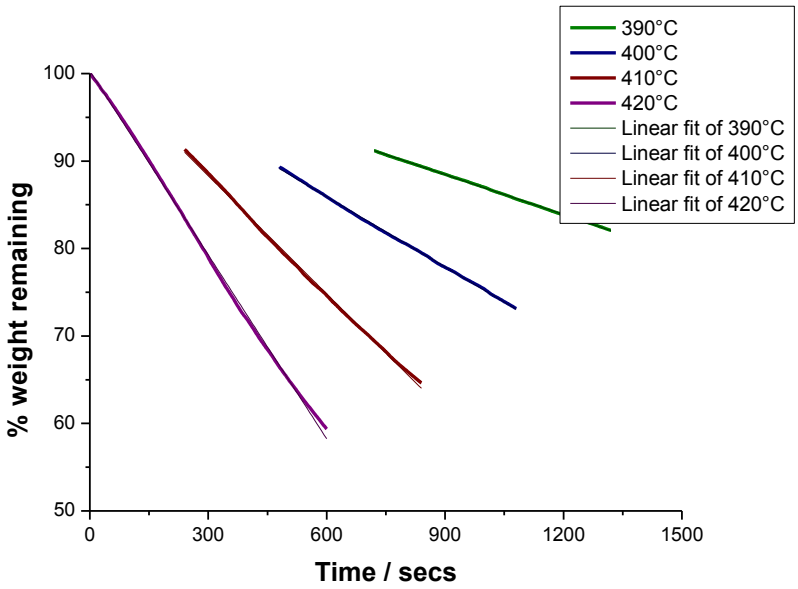

Figure 190 Duplicate plot of regions of maximum weight loss during the isothermal degradation plots for PET1.0G uniaxial film between 390ºC and 420ºC. Analysis was performed under helium. Linear fittings were also performed.

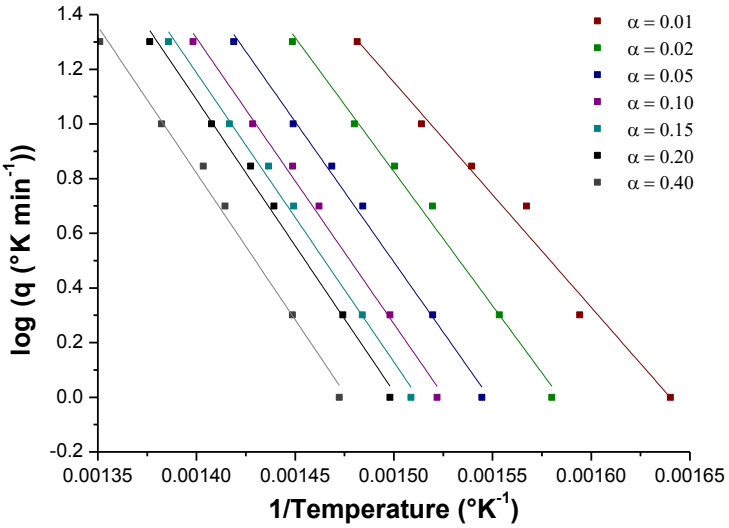

Figure 191 ASTM E1641. Conversion plot for the thermal degradation of PET uniaxial film.

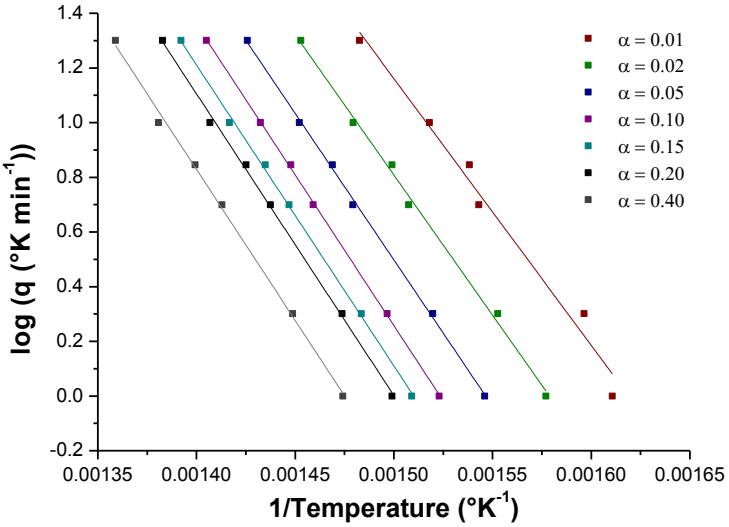

Figure 192 Duplicate. ASTM E1641. Conversion plot for the thermal degradation of PET uniaxial film.

Table 9 Gradients for the linear data fittings in the appendix figures 191 and 192.

Conversion	Δ(log β)/Δ(1/T)	
	PET uniaxial 1	PET uniaxial 2
0.01	-8239	-9758
0.02	-9808	-10256
0.05	-10264	-10711
0.10	-10448	-11013
0.15	-10579	-11001
0.20	-10691	-11034
0.40	-10730	-11048

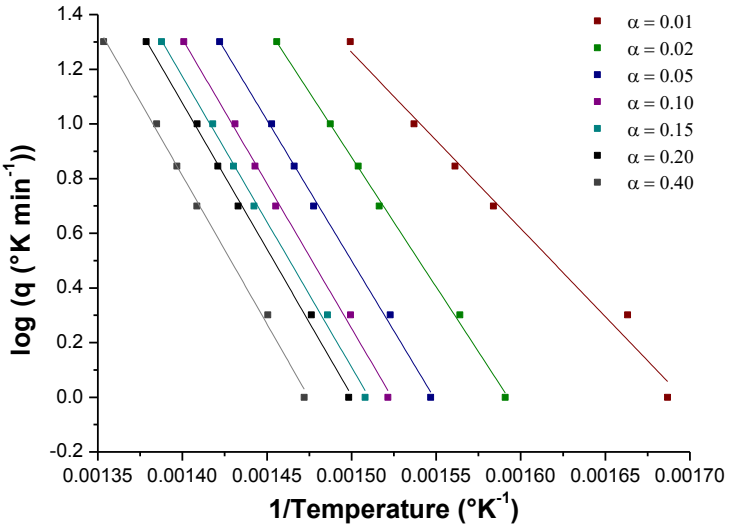

Figure 193 ASTM E1641. Conversion plot for the thermal degradation of PET0.5G uniaxial film.

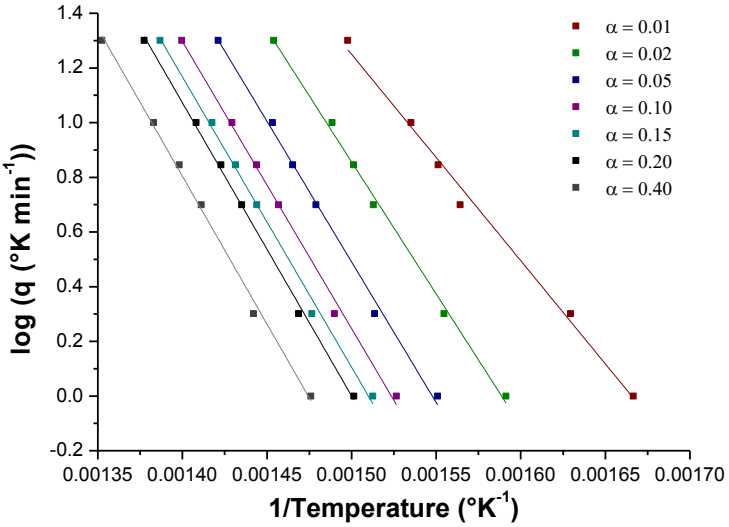

Figure 194 Duplicate. ASTM E1641. Conversion plot for the thermal degradation of PET0.5G uniaxial film.

Table 10 Gradients for the linear data fittings in the appendix figures 193 and 194.

Conversion	Δ(log β)/Δ(1/T)	
	PET0.5G uniaxial 1	PET0.5G uniaxial 2
0.01	-8238	-9758
0.02	-9808	-10256
0.05	-10264	-10711
0.10	-10448	-11013
0.15	-10579	-11001
0.20	-10691	-11034
0.40	-10730	-11048

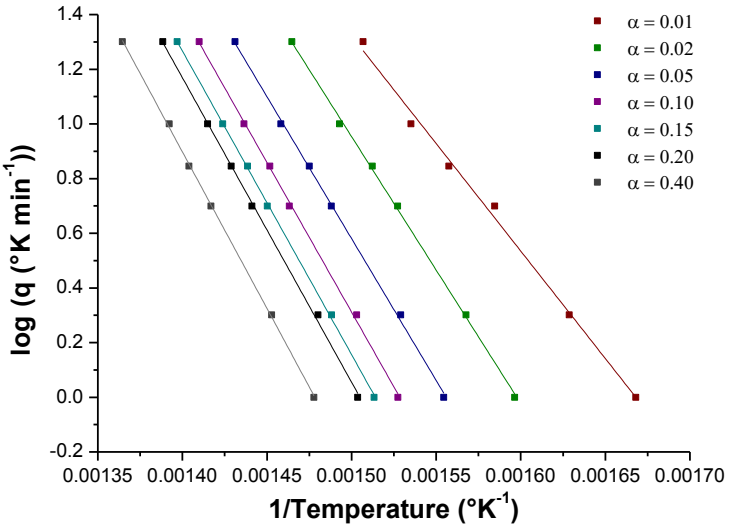

Figure 195 ASTM E1641. Conversion plot for the thermal degradation of PET1.0G uniaxial film.

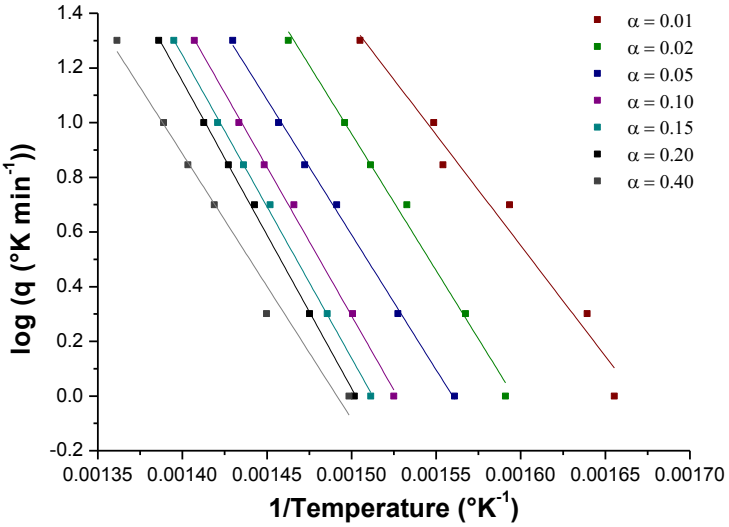

Figure 196 Duplicate. ASTM E1641. Conversion plot for the thermal degradation of PET1.0G uniaxial film.

Table 11 Gradients for the linear data fittings in the appendix figures 195 and 196.

Conversion	**Δ(log β)/Δ(1/T)**	
	PET1.0G uniaxial 1	**PET1.0G uniaxial 2**
0.01	-7864	-8098
0.02	-9765	-10007
0.05	-10378	-9882
0.10	-10936	-10867
0.15	-11109	-11082
0.20	-11138	-11233
0.40	-11465	-9700

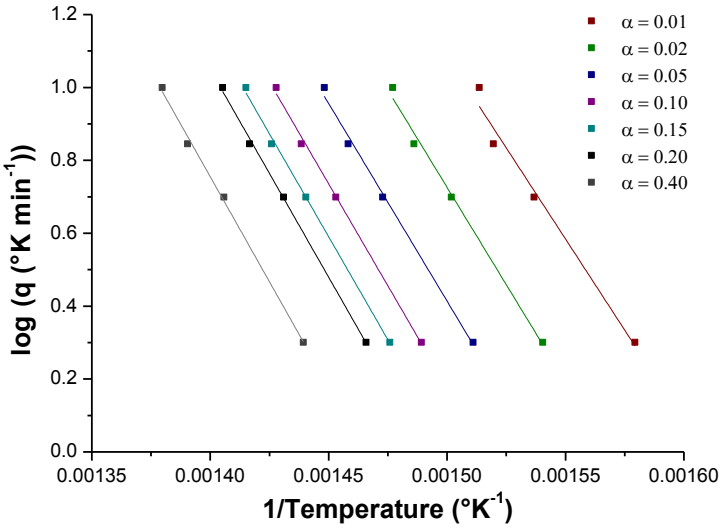

Figure 197 ASTM E1641. Conversion plot for the thermal degradation of PET chip

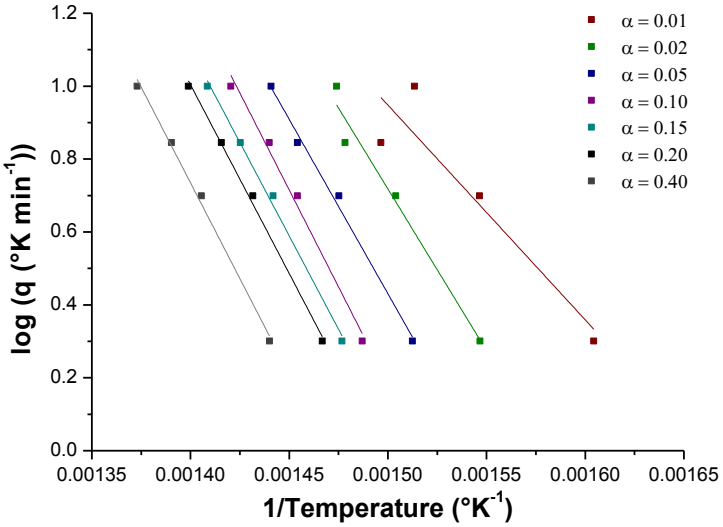

Figure 198 Duplicate. ASTM E1641. Conversion plot for the thermal degradation of PET chip

Table 12 Gradients for the linear data fittings in the appendix figures 197 and 198.

Conversion	Δ(log β)/Δ(1/T)	
	PET chip 1	PET chip 2
0.01	-9996	-5892
0.02	-10678	-8871
0.05	-10845	-9564
0.10	-11188	-10641
0.15	-11300	-10255
0.20	-11395	-10352
0.40	-11532	-10502

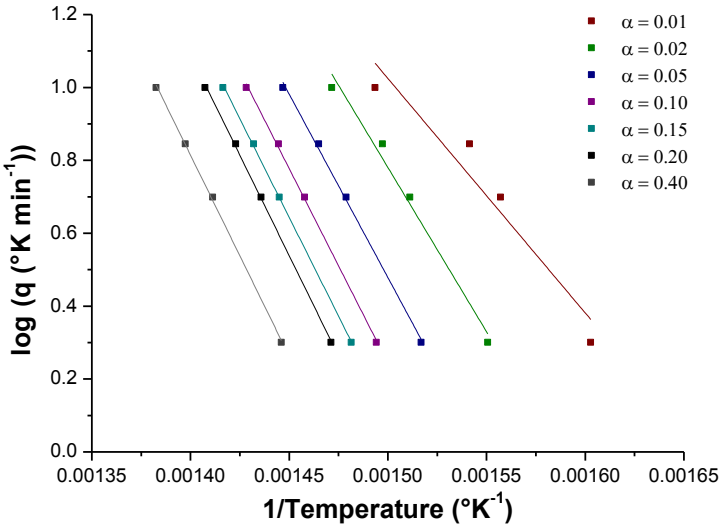

Figure 199 ASTM E1641. Conversion plot for the thermal degradation of PET0.5G chip

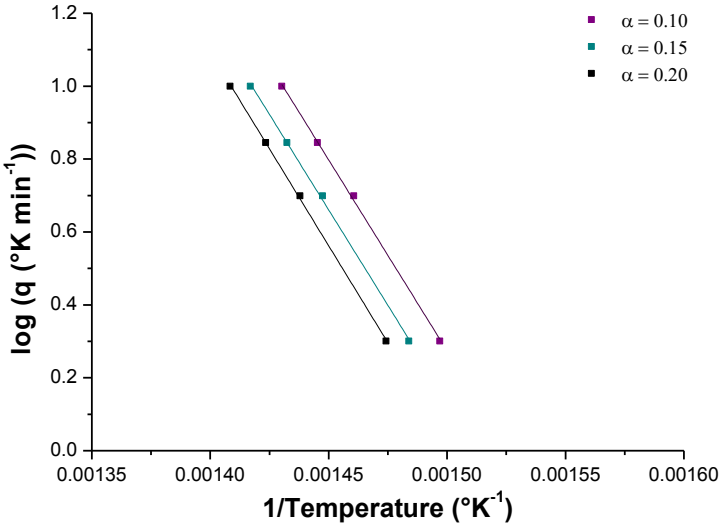

Figure 200 Duplicate. ASTM E1641. Conversion plot for the thermal degradation of PET0.5G chip

Table 13 Gradients for the linear data fittings in the appendix figures 199 and 200.

Conversion	Δ(log β)/Δ(1/T)	
	PET0.5G chip 1	PET0.5G chip 2
0.01	-6432	
0.02	-9015	
0.05	-10061	
0.10	-10677	-10476
0.15	-10828	-10471
0.20	-11027	-10635
0.40	-11043	

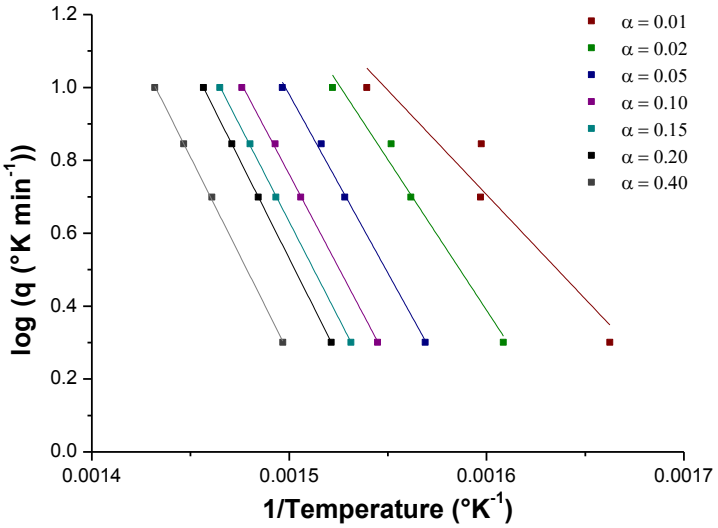

Figure 201 ASTM E1641. Conversion plot for the thermal degradation of PET1.0G chip

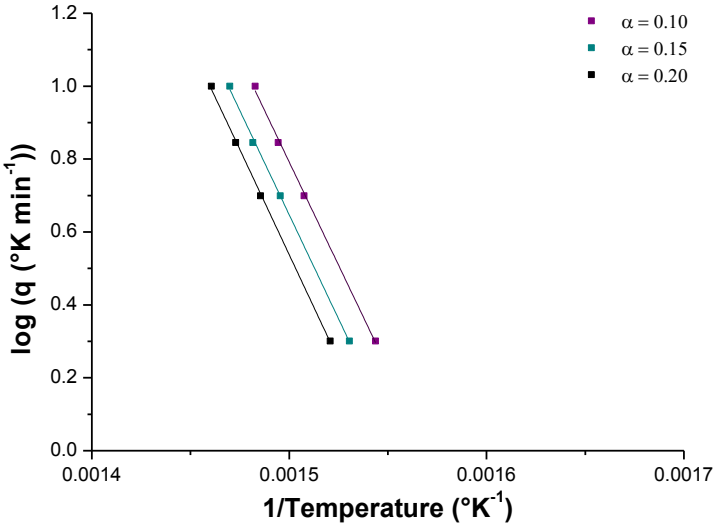

Figure 202 Duplicate. ASTM E1641. Conversion plot for the thermal degradation of PET1.0G chip

Table 14 Gradients for the linear data fittings in the appendix figures 201 and 202.

Conversion	Δ(log β)/Δ(1/T)	
	PET1.0G chip 1	PET1.0G chip 2
0.01	-5726	
0.02	-8267	
0.05	-9801	
0.10	-10245	-11324
0.15	-10556	-11.423
0.20	-10783	-11525
0.40	-10798	

Table 15 Approximation constants for kinetic model ASTM 1641

E/RT	a	b (1/K)	E/RT	a	b (1/K)
8	5.370	0.540	35	18.312	0.459
9	5.898	0.528	36	18.770	0.458
10	6.417	0.519	37	19.228	0.458
11	6.928	0.511	38	19.684	0.456
12	7.433	0.505	39	20.141	0.456
13	7.933	0.500	40	20.598	0.456
14	8.427	0.494	41	21.052	0.455
15	8.918	0.491	42	21.507	0.455
16	9.406	0.488	43	21.961	0.454
17	9.890	0.484	44	22.415	0.454
18	10.372	0.482	45	22.868	0.453
19	10.851	0.479	46	23.321	0.453
20	11.328	0.477	47	23.774	0.453
21	11.803	0.475	48	24.226	0.452
22	12.276	0.473	49	24.678	0.452
23	12.747	0.471	50	25.130	0.452
24	13.217	0.470	51	25.581	0.451
25	13.686	0.469	52	26.031	0.451
26	14.153	0.467	53	26.482	0.451
27	14.619	0.466	54	26.932	0.450
28	15.084	0.465	55	27.382	0.450
29	15.547	0.463	56	27.832	0.450
30	16.010	0.463	57	28.281	0.450
31	16.472	0.462	58	28.731	0.449
32	16.933	0.461	59	29.179	0.449
33	17.394	0.461	60	29.628	0.449
34	17.853	0.459			

Table 16 Approximation constants for kinetic model ASTM E698

E/RT	D	E/RT	D	E/RT	D
5	1.4	29	1.069	53	1.0377
6	1.3333	30	1.0667	54	1.037
7	1.2857	31	1.0645	55	1.0364
8	1.25	32	1.0625	56	1.0357
9	1.2222	33	1.0606	57	1.0351
10	1.2	34	1.0588	58	1.0345
11	1.1818	35	1.0571	59	1.0339
12	1.1667	36	1.0556	60	1.0333
13	1.1538	37	1.0541	61	1.0328
14	1.1429	38	1.0526	62	1.0323
15	1.1333	39	1.0513	63	1.0317
16	1.125	40	1.05	64	1.0312
17	1.1176	41	1.0488	65	1.0308
18	1.1111	42	1.0476	66	1.0303
19	1.1053	43	1.0465	67	1.0299
20	1.1	44	1.0455	68	1.0294
21	1.0952	45	1.0444	69	1.029
22	1.0909	46	1.0435	70	1.0286
23	1.087	47	1.0426	71	1.0282
24	1.0833	48	1.0417	72	1.0278
25	1.08	49	1.0408	73	1.0274
26	1.0769	50	1.04	74	1.027
27	1.0741	51	1.0392		
28	1.0714	52	1.0385		

APPENDIX 8: THERMO-OXIDATIVE DEGRADATION

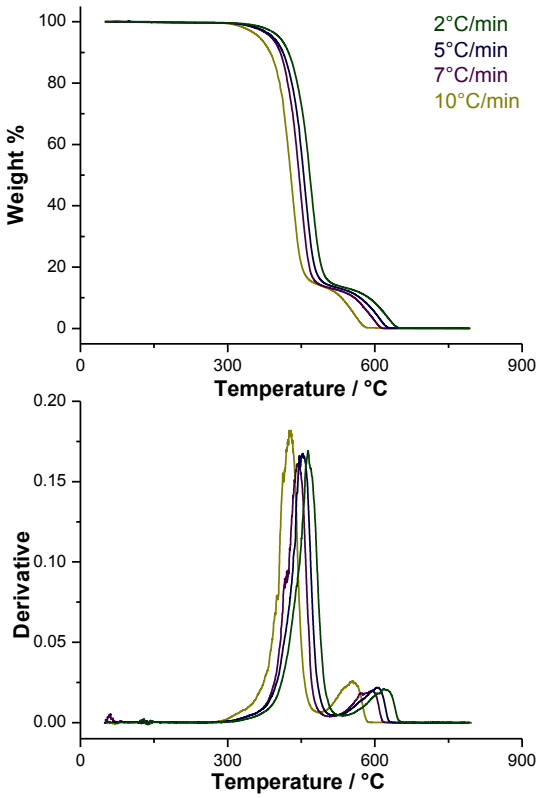

Figure 203 TGA thermograms for PET chip during thermo-oxidative degradation under air.

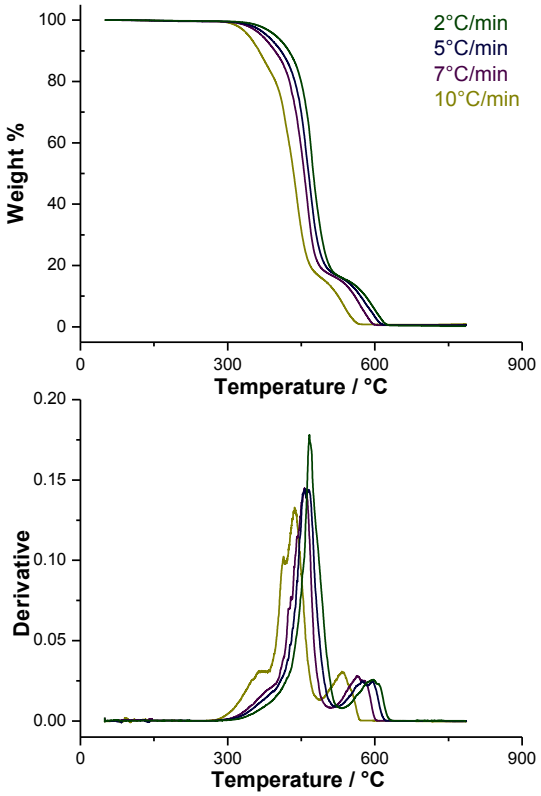

Figure 204 TGA thermograms for PET0.5G chip during thermo-oxidative degradation under air.

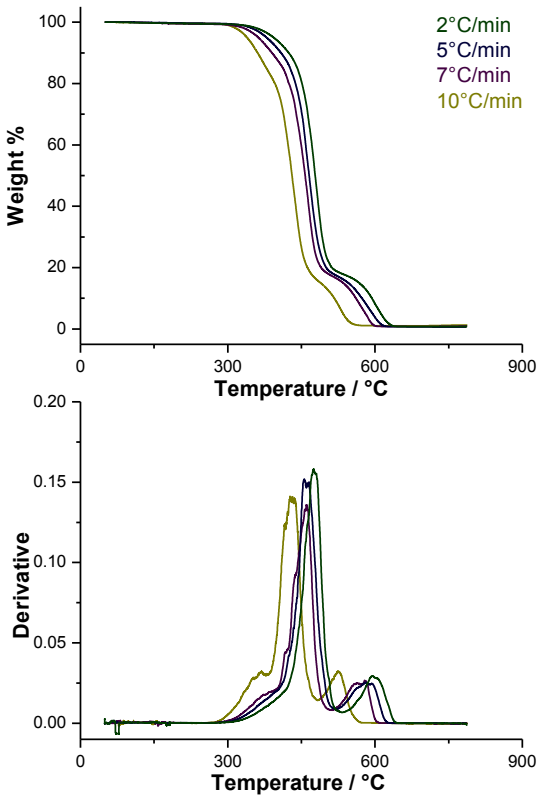

Figure 205 TGA thermograms for PET1.0G chip during thermo-oxidative degradation under air.

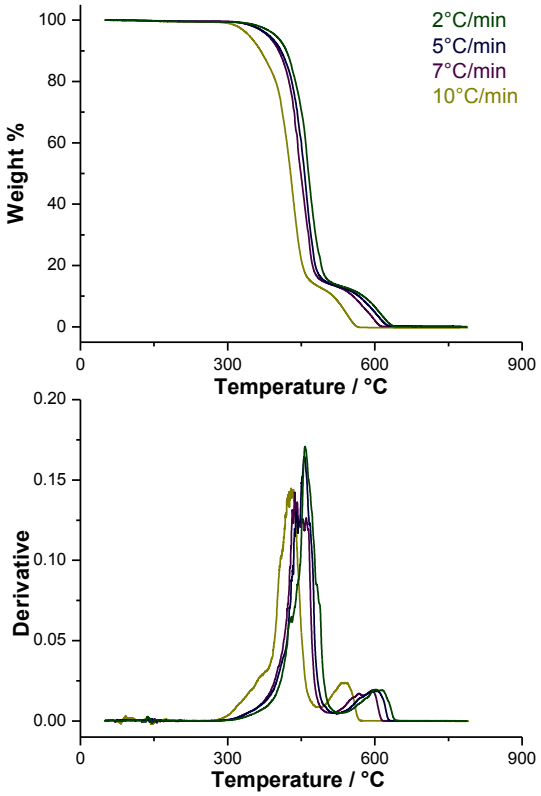

Figure 206 Replicate. TGA thermograms for PET chip during thermo-oxidative degradation under air.

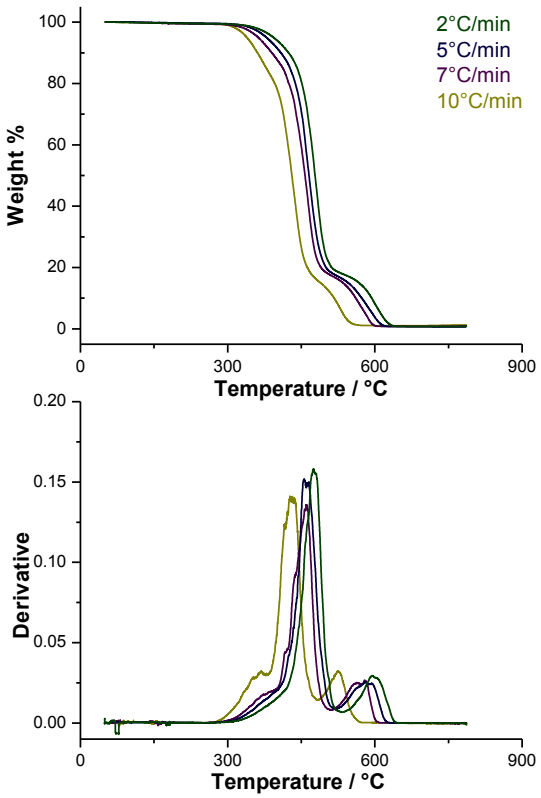

Figure 207 Replicate.TGA thermograms for PET0.5G chip during thermo-oxidative degradation (air).

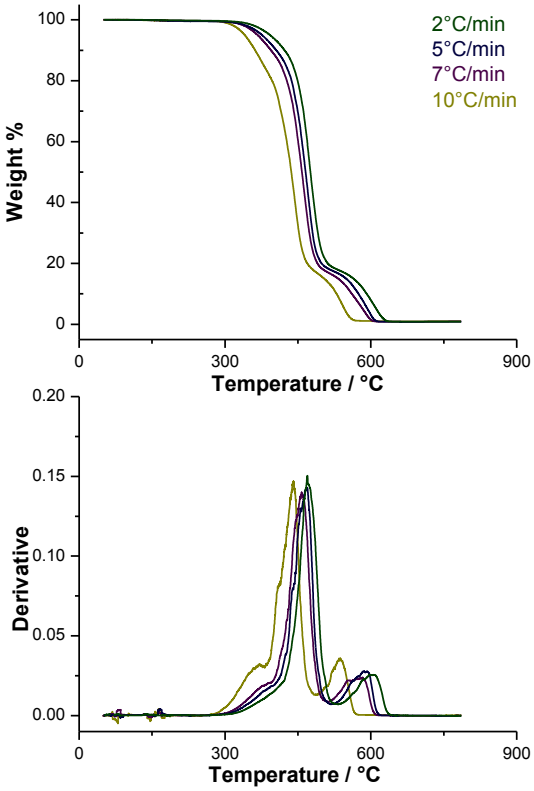

Figure 208 Replicate.TGA thermograms for PET1.0G chip during thermo-oxidative degradation (air).

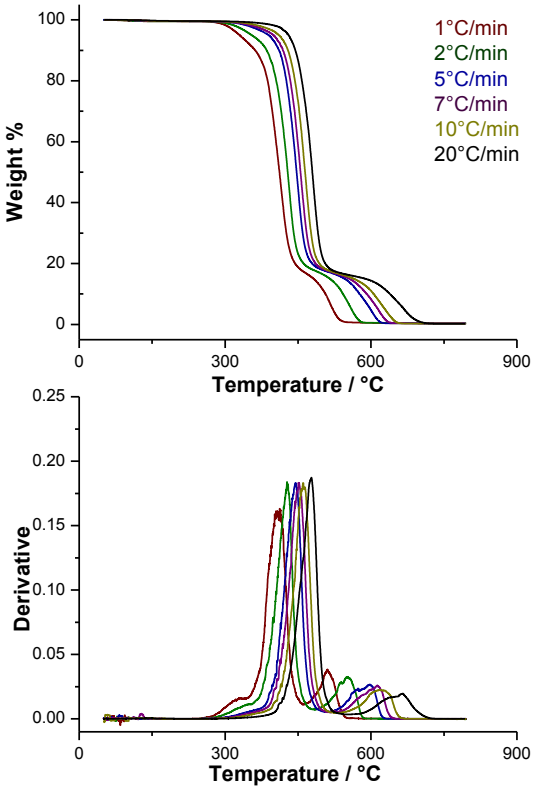

Figure 209 TGA thermograms for PET0.5G uniaxial film during thermo-oxidative degradation (air).

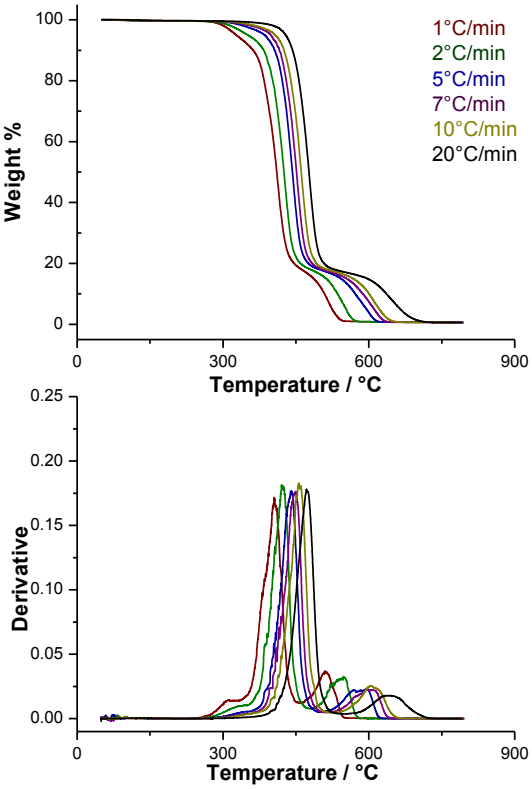

Figure 210 TGA thermograms for PET1.0G uniaxial film during thermo-oxidative degradation (air).

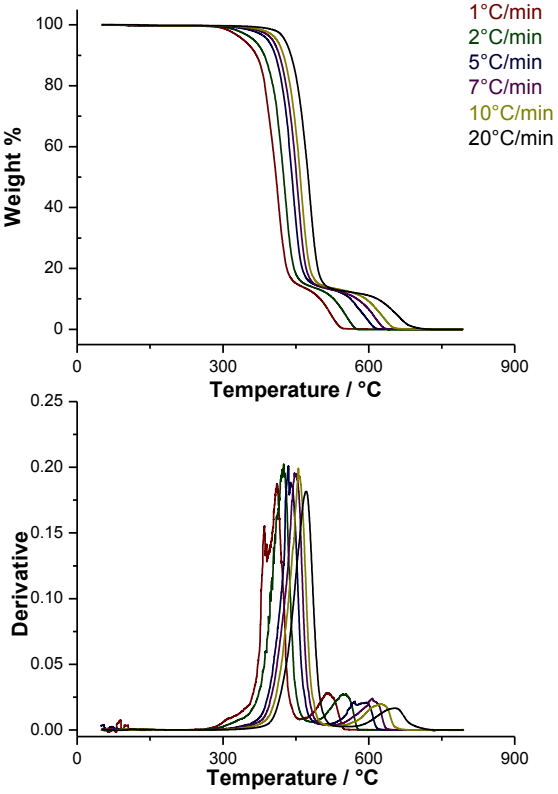

Figure 211 Duplicate. Thermograms for PET uniaxial film during thermo-oxidative degradation (air).

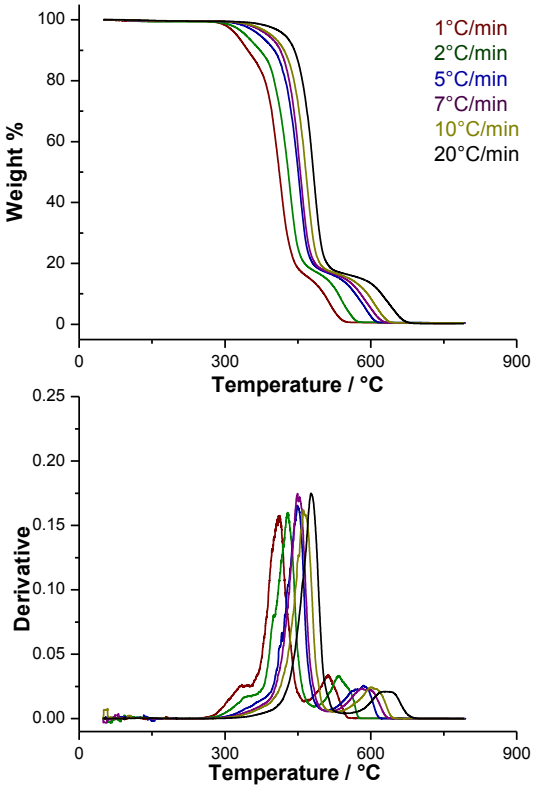

Figure 212 Duplicate. TGA thermograms for PET0.5G uniaxial film during thermo-oxidative degradation (air).

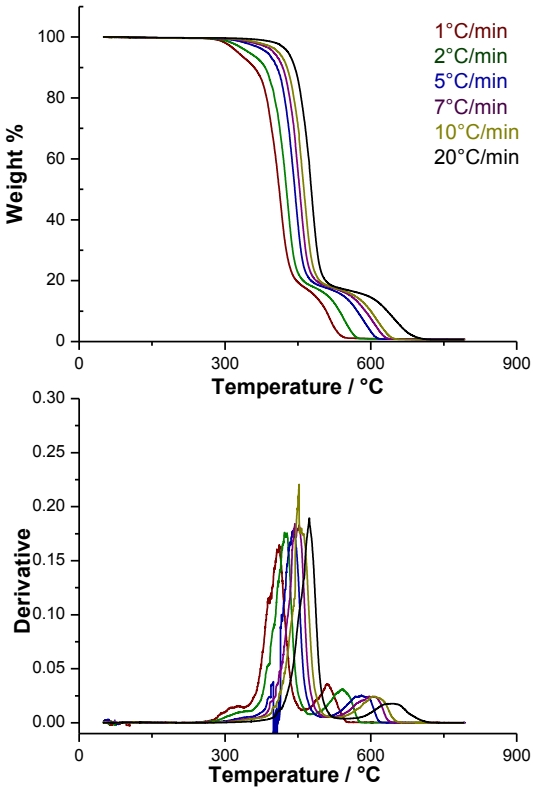

Figure 213 Duplicate. TGA thermograms for PET1.0G uniaxial film during thermo-degradation (air).

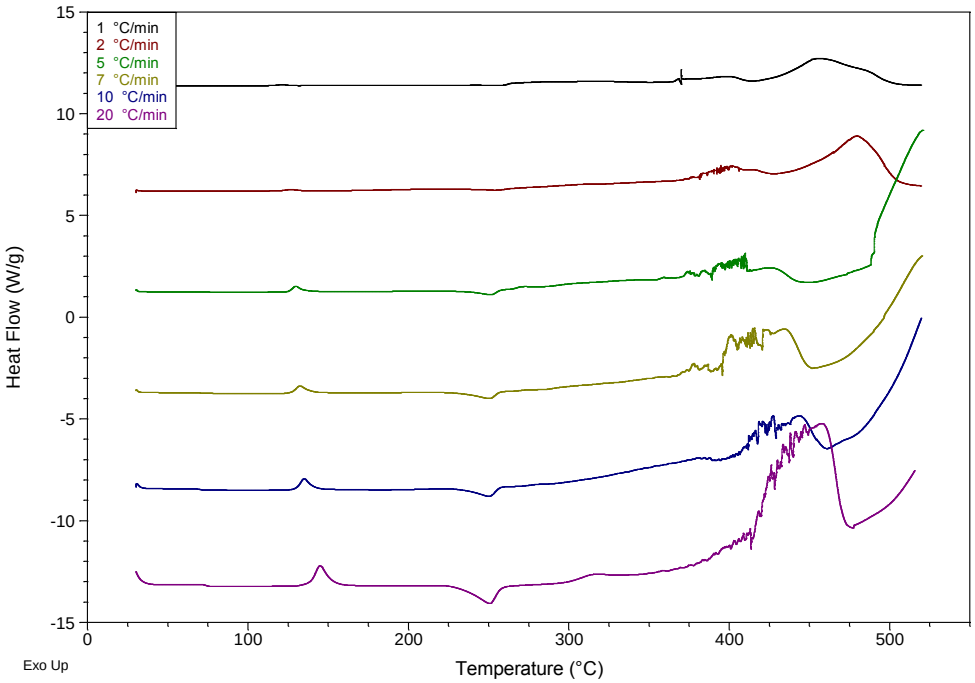

Figure 214 Replicate. Dynamic thermo-oxidative degradation profiles of PET at various heating rates. Analysis was performed under air.

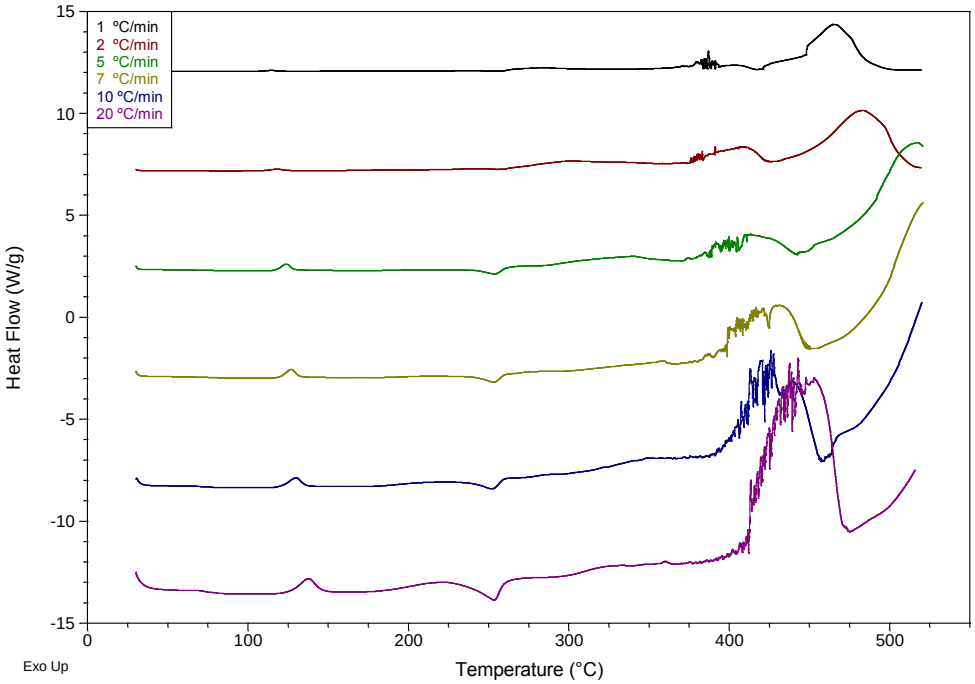

Figure 215 Replicate. Dynamic thermo-oxidative degradation profiles of PET0.5G at various heating rates. Analysis was performed under air.

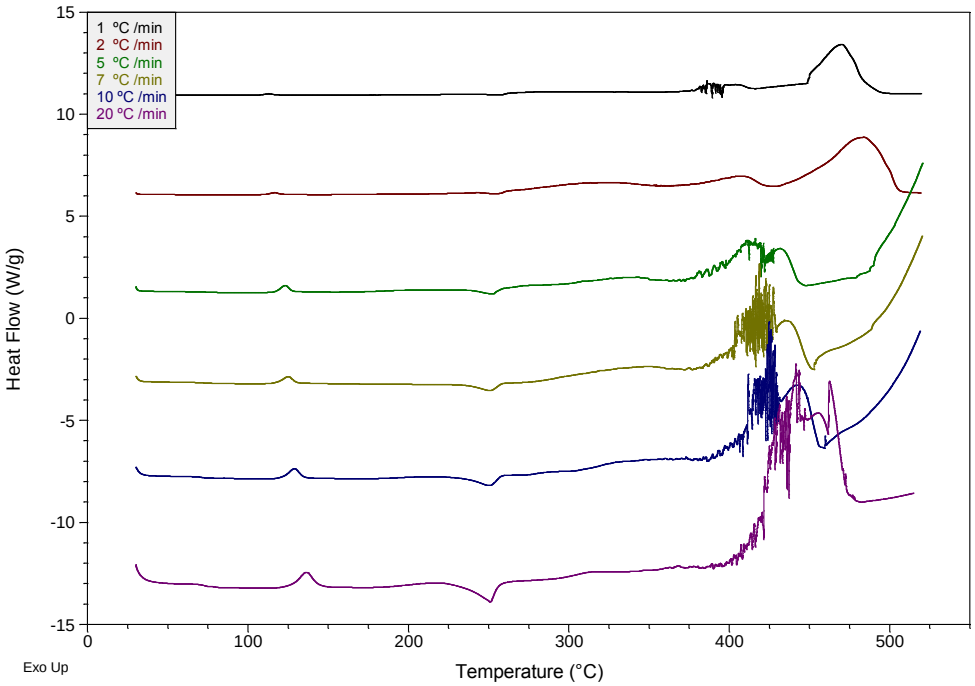

Figure 216 Replicate. Dynamic thermo-oxidative degradation profiles of PET1.0G at various heating rates. Analysis was performed under air.

APPENDIX 9: THERMO-OXIDATIVE DEGRADATION KINETICS

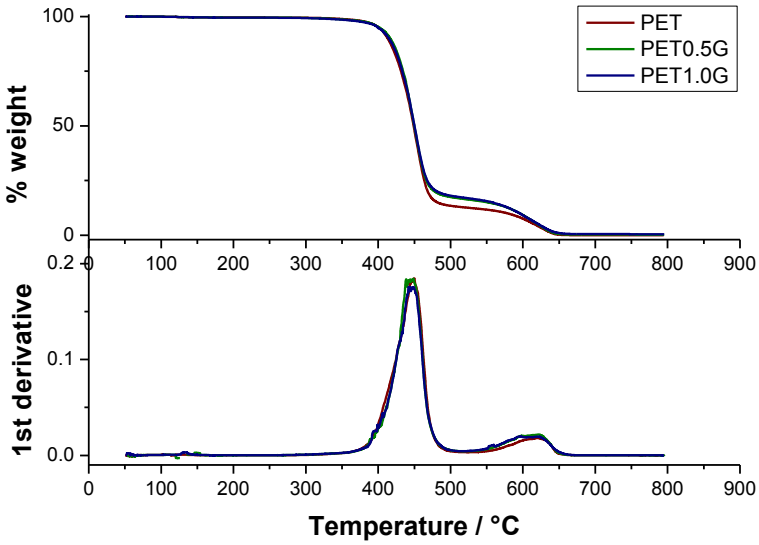

Figure 217 Duplicate. Dynamic thermo-oxidative run of PET, PET0.5G and PET1.0G at 10ºC min^{-1}. Run was performed under air.

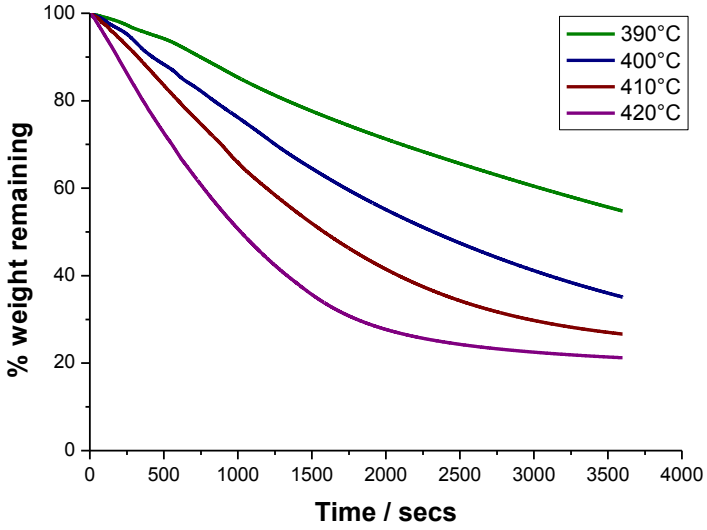

Figure 218 Isothermal thermo-oxidative degradative plots for PET0.5G between 390ºC and 420ºC. The isothermal was held for 1 hour. Analysis was performed under air.

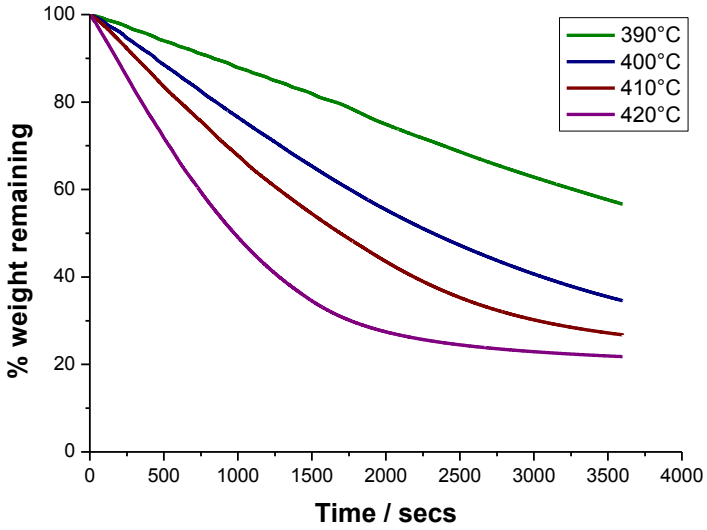

Figure 219 Isothermal thermo-oxidative degradative plots for PET1.0G between 390ºC and 420ºC. The isothermal was held for 1 hour. Analysis was performed under air.

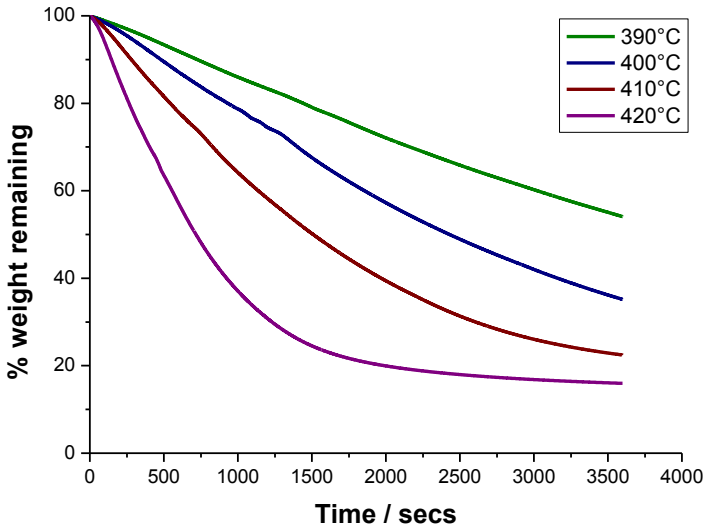

Figure 220 Replicate. Isothermal thermo-oxidative degradative plots for PET between 390ºC and 420ºC. The isothermal was held for 1 hour. Analysis was performed under air.

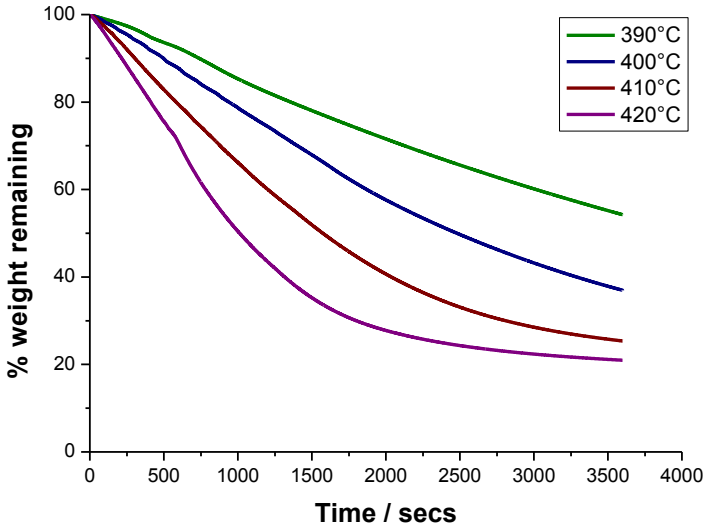

Figure 221 Replicate. Isothermal thermo-oxidative degradative plots for PET0.5G between 390ºC and 420ºC. The isothermal was held for 1 hour. Analysis was performed under air.

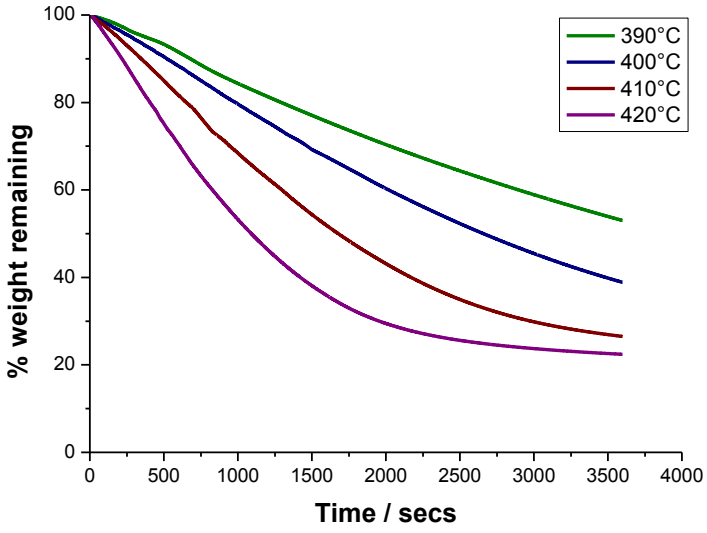

Figure 222 Replicate. Isothermal thermo-oxidative degradative plots for PET1.0G between 390ºC and 420ºC. The isothermal was held for 1 hour. Analysis was performed under air.

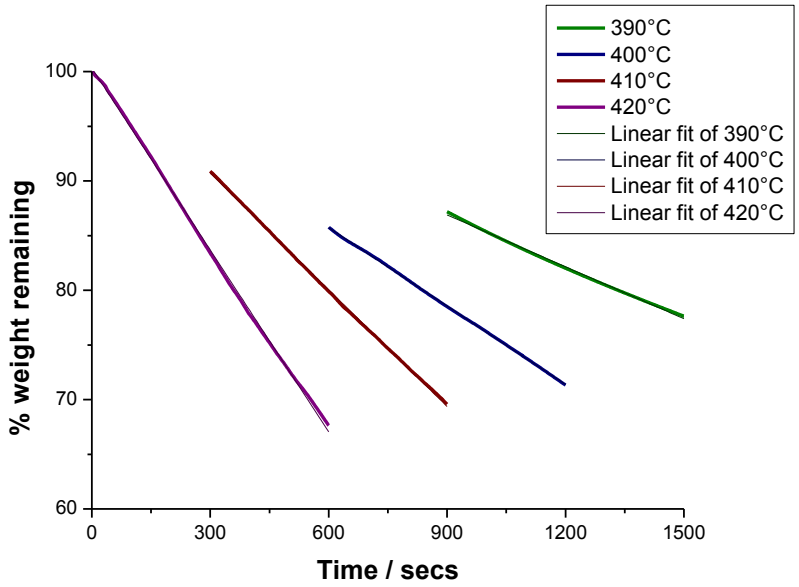

Figure 223 Regions of maximum weight loss during the isothermal thermo-oxidative degradation plots for PET0.5G between 390ºC and 420ºC. Analysis was performed under air. Linear fittings were also performed.

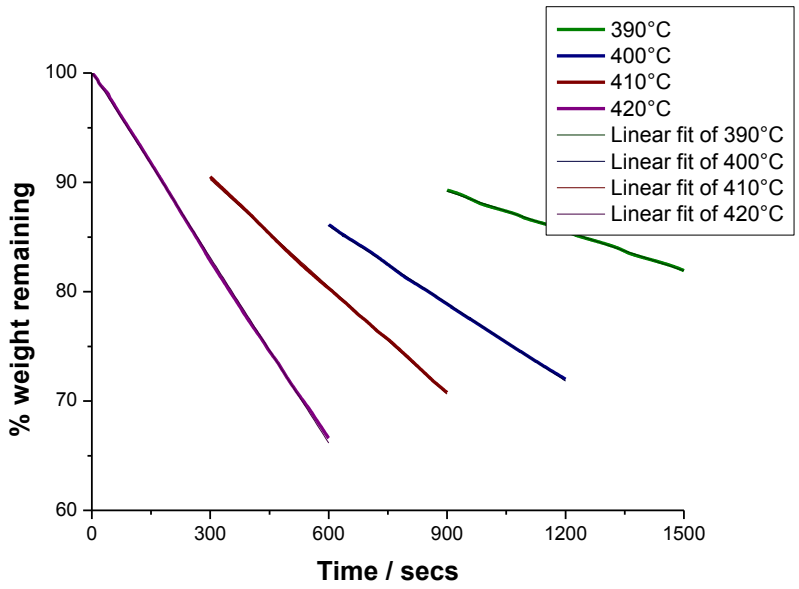

Figure 224 Regions of maximum weight loss during the isothermal degradation plots for PET1.0G between 390ºC and 420ºC. Analysis was performed under air. Linear fittings were also performed.

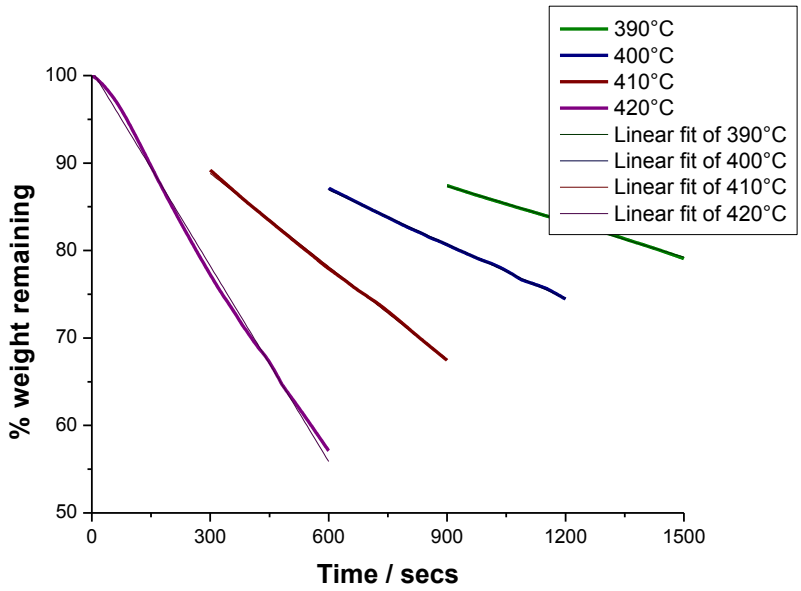

Figure 225 Duplicate. Regions of maximum weight loss during the isothermal degradation plots for PET between 390ºC and 420ºC. Analysis was performed under air. Linear fittings were also performed.

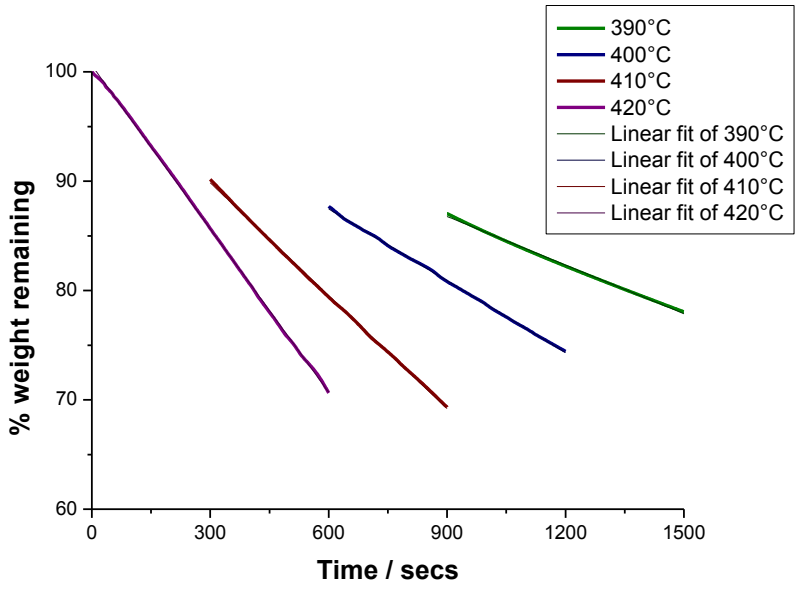

Figure 226 Duplicate. Regions of maximum weight loss during the isothermal thermo-oxidative degradation plots for PET0.5G between 390ºC and 420ºC. Analysis was performed under air. Linear fittings were also performed.

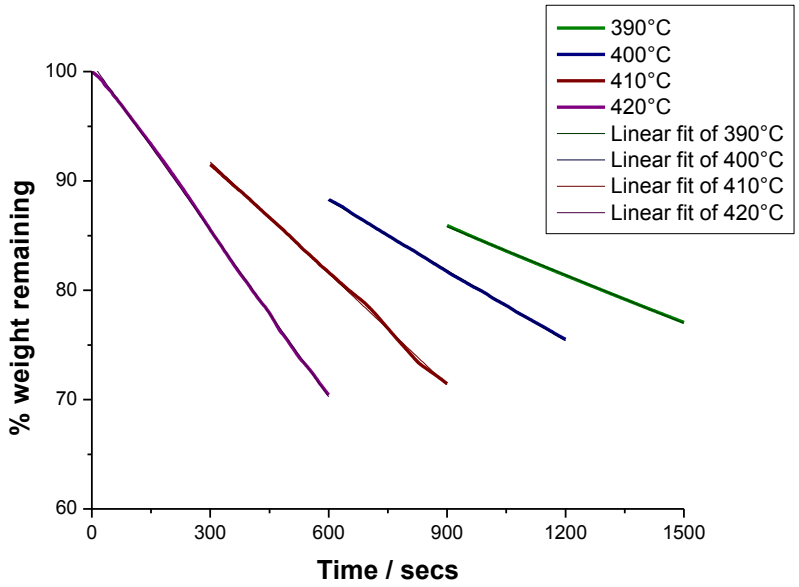

Figure 227 Duplicate. Regions of maximum weight loss during the isothermal degradation plots for PET1.0G between 390ºC and 420ºC. Analysis was performed under air. Linear fittings were also performed.

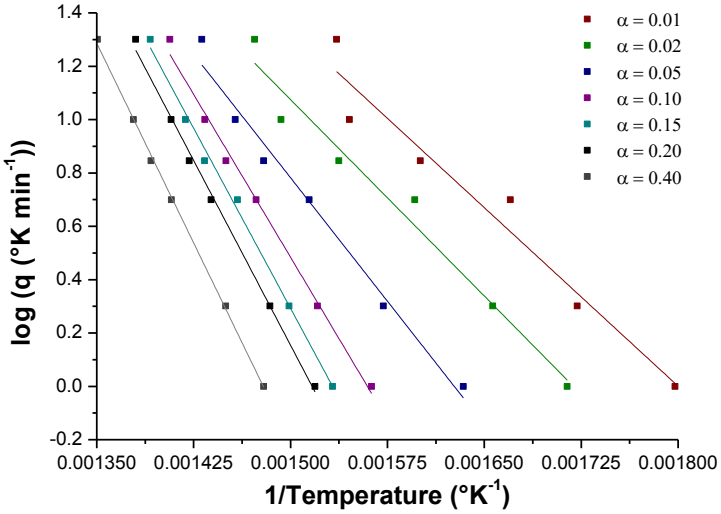

Figure 228 ASTM E1641. Conversion plot for the thermo-oxidative degradation of PET uniaxial film

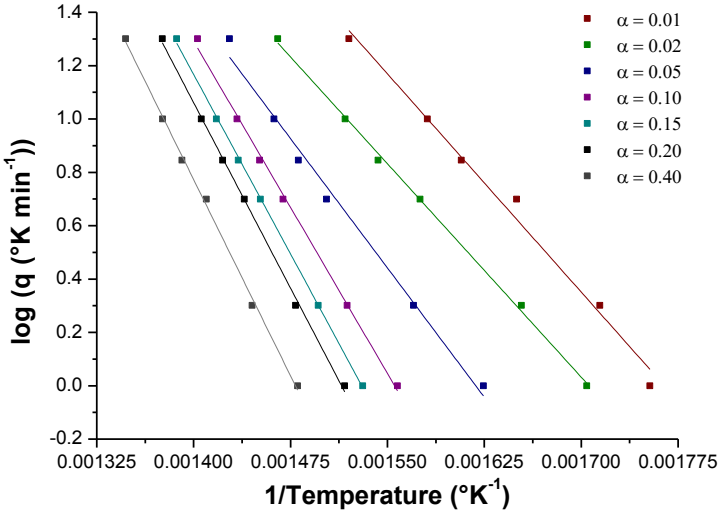

Figure 229 Duplicate. ASTM E1641. Conversion plot for the thermo-oxidative degradation of PET uniaxial film

Table 17 Gradients for the linear data fittings in the appendix figures 228 and 229.

Conversion	Δ(log β)/Δ(1/T)	
	PET uniaxial 1	PET uniaxial 2
0.01	-4463	-5454
0.02	-4909	-5333
0.05	-6169	-6461
0.10	-8137	-8303
0.15	-8999	-8968
0.20	-9232	-9270
0.40	-9979	-9809

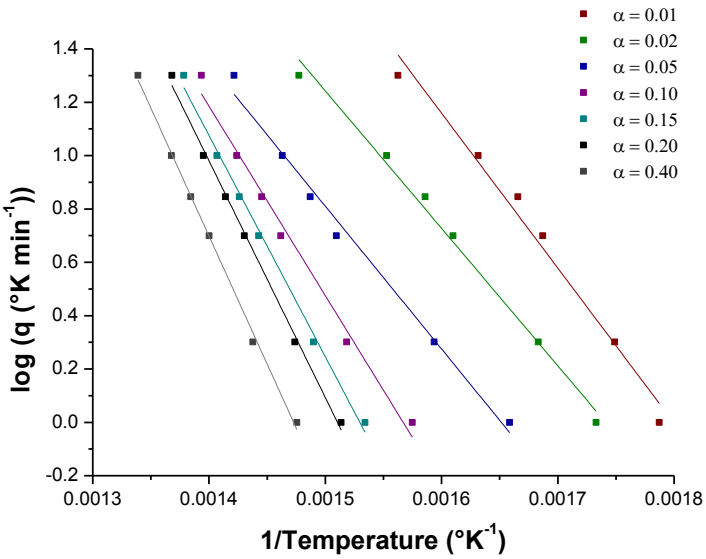

Figure 230 ASTM E1641. Conversion plot for the thermo-oxidative degradation of PET0.5G uniaxial film

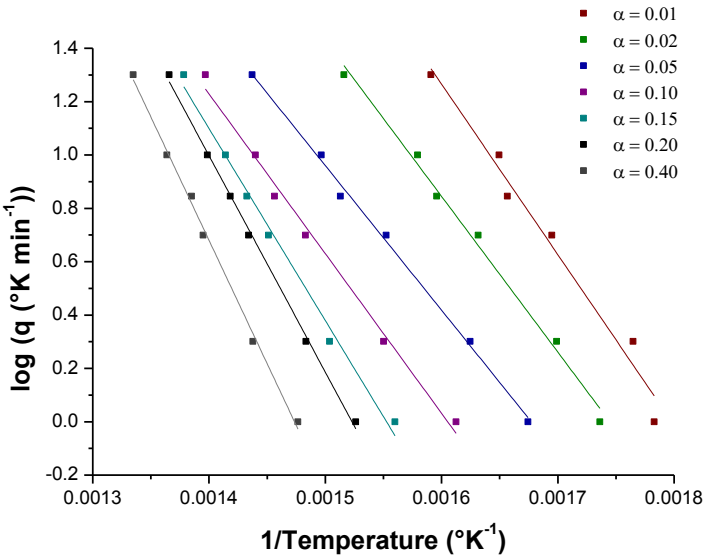

Figure 231 Duplicate. ASTM E1641. Conversion plot for the thermo-oxidative degradation of PET0.5G uniaxial film

Table 18 Gradients for the linear data fittings in the appendix figures 230 and 231.

Conversion	Δ(log β)/Δ(1/T)	
	PET0.5G uniaxial 1	PET0.5G uniaxial 2
0.01	-5810	-6391
0.02	-5154	-5838
0.05	-5351	-5421
0.10	-7097	-5986
0.15	-8292	-7201
0.20	-8871	-8107
0.40	-9595	-9247

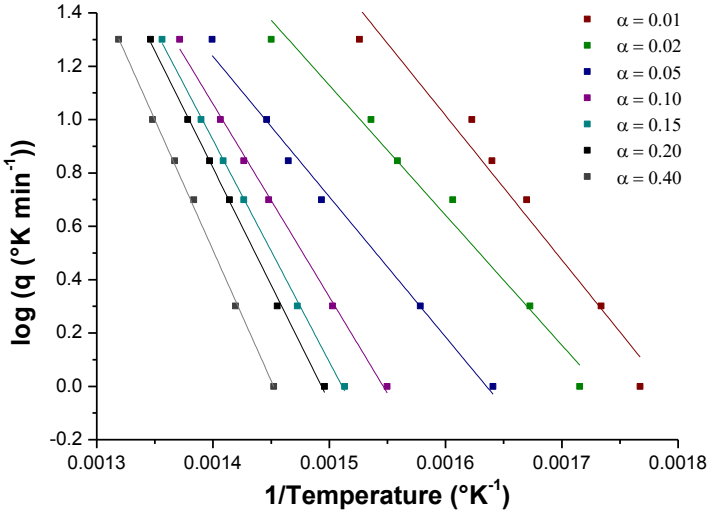

Figure 232 ASTM E1641. Conversion plot for the thermo-oxidative degradation of PET1.0G uniaxial film

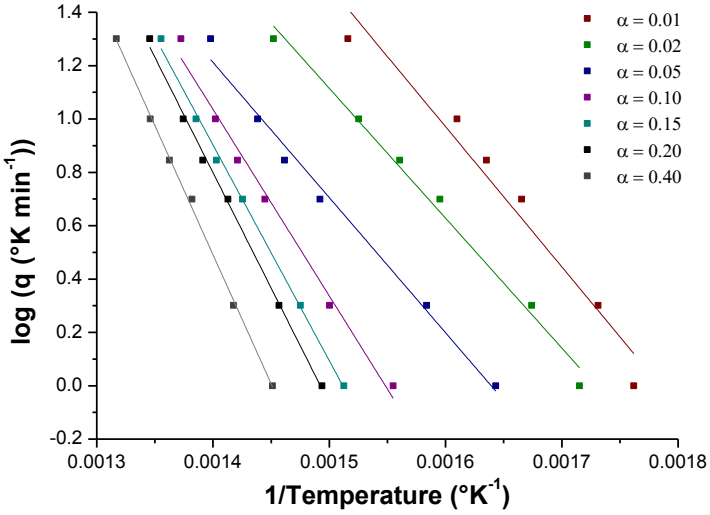

Figure 233 Duplicate. ASTM E1641. Conversion plot for the thermo-oxidative degradation of PET1.0G uniaxial film

Table 19 Gradients for the linear data fittings in the appendix figures 232 and 233.

Conversion	**Δ(log β)/Δ(1/T)**	
	PET1.0G uniaxial 1	**PET1.0G uniaxial 2**
0.01	-5409	-5254
0.02	-4873	-4869
0.05	-5257	-5066
0.10	-7228	-6989
0.15	-8312	-8009
0.20	-8766	-8648
0.40	-9777	-9683

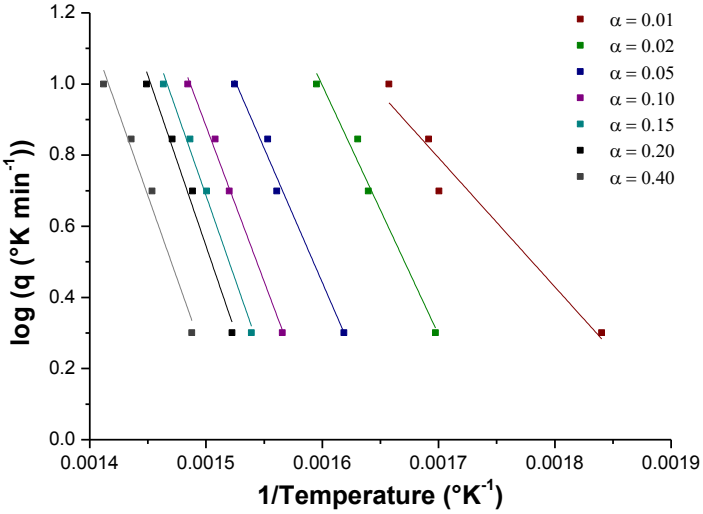

Figure 234 ASTM E1641. Conversion plot for the thermo-oxidative degradation of PET chip

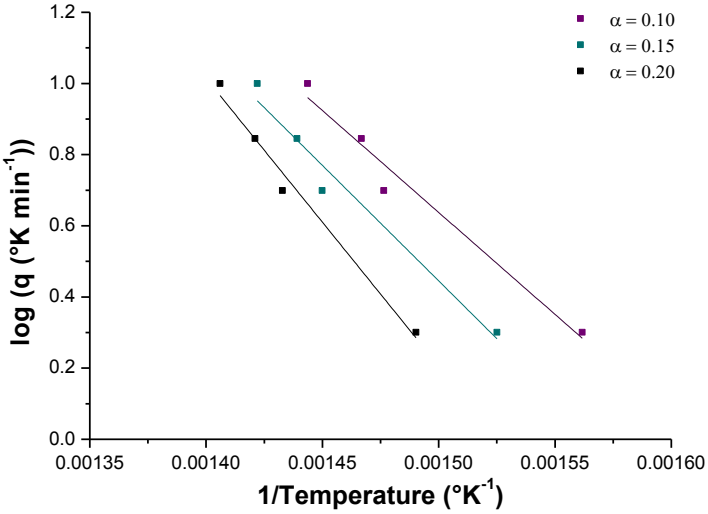

Figure 235 Duplicate. ASTM E1641. Conversion plot for the thermo-oxidative degradation of PET chip

Table 20 Gradients for the linear data fittings in the appendix figures 234 and 235.

Conversion	Δ(log β)/Δ(1/T)	
	PET chip 1	PET chip 2
0.01	-3629	
0.02	-7008	
0.05	-7551	
0.10	-8737	-5730
0.15	-9391	-6492
0.20	-9586	-8086
0.40	-9274	

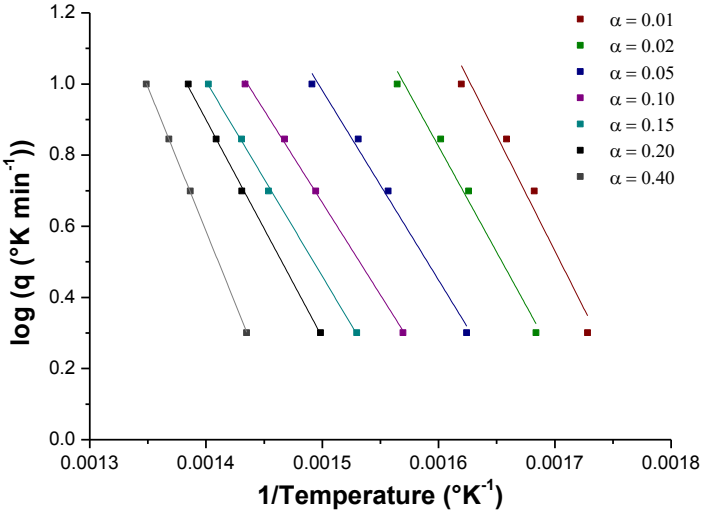

Figure 236 ASTM E1641. Conversion plot for the thermo-oxidative degradation of PET0.5G chip

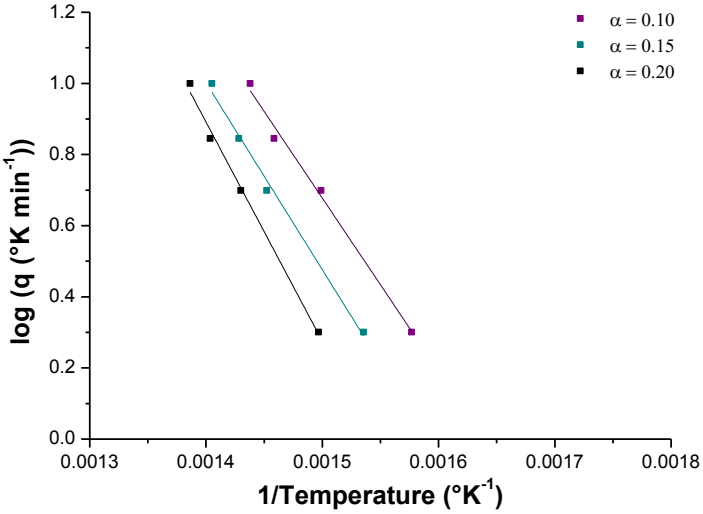

Figure 237 Duplicate. ASTM E1641. Conversion plot for the thermo-oxidative degradation of PET0.5G chip

Table 21 Gradients for the linear data fittings in the appendix figures 236 and 237.

Conversion	Δ(log β)/Δ(1/T)	
	PET0.5G chip 1	PET0.5G chip 2
0.01	-6481	
0.02	-5947	
0.05	-5333	
0.10	-5187	-4872
0.15	-5480	-5254
0.20	-6119	-6161
0.40	-8100	

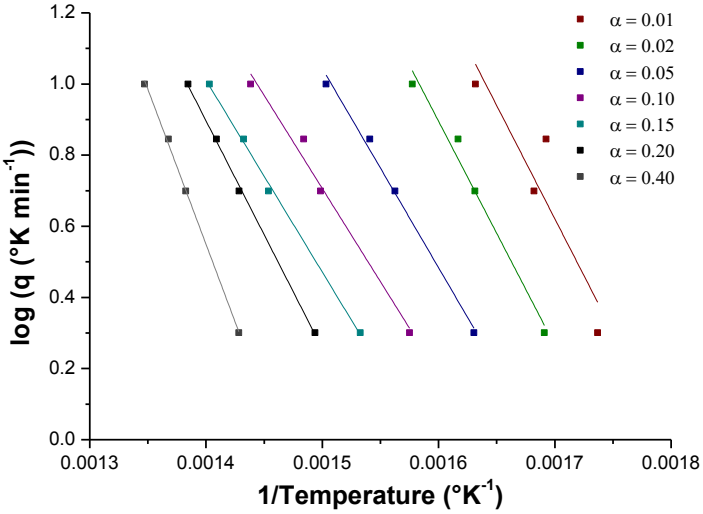

Figure 238 ASTM E1641. Conversion plot for the thermo-oxidative degradation of PET1.0G chip

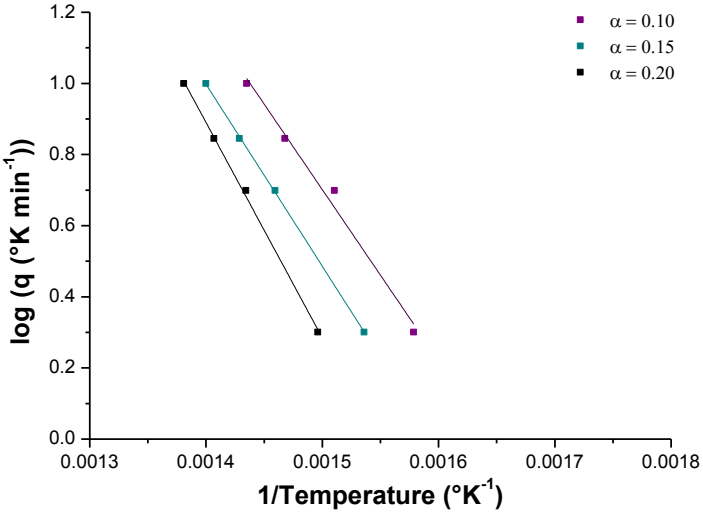

Figure 239 Duplicate. ASTM E1641. Conversion plot for the thermo-oxidative degradation of PET1.0G chip

Table 22 Gradients for the linear data fittings in the appendix figures 238 and 239.

Conversion	Δ(log β)/Δ(1/T)	
	PET1.0G chip 1	PET1.0G chip 2
0.01	-6369	
0.02	-6301	
0.05	-5601	
0.10	-5227	-4808
0.15	-5391	-5117
0.20	-6406	-6506
0.40	-8716	

Table 23 Approximation constants for kinetic model ASTM 1641

E/RT	a	b (1/K)	E/RT	a	b (1/K)
8	5.370	0.540	35	18.312	0.459
9	5.898	0.528	36	18.770	0.458
10	6.417	0.519	37	19.228	0.458
11	6.928	0.511	38	19.684	0.456
12	7.433	0.505	39	20.141	0.456
13	7.933	0.500	40	20.598	0.456
14	8.427	0.494	41	21.052	0.455
15	8.918	0.491	42	21.507	0.455
16	9.406	0.488	43	21.961	0.454
17	9.890	0.484	44	22.415	0.454
18	10.372	0.482	45	22.868	0.453
19	10.851	0.479	46	23.321	0.453
20	11.328	0.477	47	23.774	0.453
21	11.803	0.475	48	24.226	0.452
22	12.276	0.473	49	24.678	0.452
23	12.747	0.471	50	25.130	0.452
24	13.217	0.470	51	25.581	0.451
25	13.686	0.469	52	26.031	0.451
26	14.153	0.467	53	26.482	0.451
27	14.619	0.466	54	26.932	0.450
28	15.084	0.465	55	27.382	0.450
29	15.547	0.463	56	27.832	0.450
30	16.010	0.463	57	28.281	0.450
31	16.472	0.462	58	28.731	0.449
32	16.933	0.461	59	29.179	0.449
33	17.394	0.461	60	29.628	0.449
34	17.853	0.459			

Table 24 Approximation constants for kinetic model ASTM E698

E/RT	D	E/RT	D	E/RT	D
5	1.4	29	1.069	53	1.0377
6	1.3333	30	1.0667	54	1.037
7	1.2857	31	1.0645	55	1.0364
8	1.25	32	1.0625	56	1.0357
9	1.2222	33	1.0606	57	1.0351
10	1.2	34	1.0588	58	1.0345
11	1.1818	35	1.0571	59	1.0339
12	1.1667	36	1.0556	60	1.0333
13	1.1538	37	1.0541	61	1.0328
14	1.1429	38	1.0526	62	1.0323
15	1.1333	39	1.0513	63	1.0317
16	1.125	40	1.05	64	1.0312
17	1.1176	41	1.0488	65	1.0308
18	1.1111	42	1.0476	66	1.0303
19	1.1053	43	1.0465	67	1.0299
20	1.1	44	1.0455	68	1.0294
21	1.0952	45	1.0444	69	1.029
22	1.0909	46	1.0435	70	1.0286
23	1.087	47	1.0426	71	1.0282
24	1.0833	48	1.0417	72	1.0278
25	1.08	49	1.0408	73	1.0274
26	1.0769	50	1.04	74	1.027
27	1.0741	51	1.0392		
28	1.0714	52	1.0385		